

NOTES ON CHANNELING

J.U. Andersen

LIST OF CONTENTS AND FIGURES

Chapters	Page	Figures
1. Introduction	2	
2. Directional effects	3	1-3
3. Deflection by atom	6	4
4. Continuum potential	8	5
5. Atomic potential	10	6
6. Critical angles	13	7, 8
7. Thermal vibrations	18	9
8. Merging of axial and planar effects	21	10-12
9. Reversibility and blocking	24	
10. Experimental observation	26	19-21a
11. Statistical treatment	33	22
12. Trend towards equilibrium	37	23, 24
13. Three stages in particle motion	40	25-29
14. Standard model	45	30-34
15. Corrections to χ_{\min} and $\psi_{1/2}$	53	35-41
16. Compensation rules	60	42, 43
17. Scattering of random and aligned beam	66	44-46
18. Dechanneling	82	47-56
19. Stopping and atomic processes in channelled ions	102	57-66
20. Applications of channeling and blocking	112	67-72
21. Electrons and positrons, channeling radiation	118	73-87
22. References	130	

1. INTRODUCTION

Ion channeling in crystals was discovered in the early 1960s [Davies 1983]. Systematic studies of the range of low-energy heavy ions revealed significant discrepancies from theoretical expectations. The average range was found to be in good agreement with theory, but there was in polycrystalline materials a nearly exponential tail of ions with much longer range. Experiments with amorphous and single-crystalline materials soon proved that the effect was caused by enhanced penetration along major axes in the crystals [Piercy *et al.* 1963], [Lutz and Sizmann 1963]. Also computer simulations of ion penetration showed this effect [Robinson and Oen 1963].

As the name 'channeling' indicates, the longer penetration was associated with the existence of open 'channels' between the rows of crystals atoms. At first, the effect was believed to be limited to low-energy ions, but experiments with MeV protons soon indicated strong deviations from normal energy loss for penetration through a thin crystal parallel to an axis [Dearnaley 1964].

A decisive step in the development was Jens Lindhard's theoretical analysis in 1964-65 of channeling phenomena [Lindhard 1964, 65]. The conditions for stable channeling trajectories were shown to lead to a critical upper value of the angle of incidence ψ relative to an axis. For ψ -values below this limit, the ions are reflected from the atomic strings due to correlated deflections by the atoms, without penetrating to the core of the strings. This string effect was predicted to lead to a dramatic reduction in yield of, e.g., nuclear reactions between the projectile and the atomic nuclei, a prediction which was soon confirmed by experiments [Bøgh 1964, 65], [Andersen 1965]. Also the closely related effect of blocking by an atomic string of particles emitted from or scattered from a string atom was soon established independently by several groups [Domeij and Björkqvist 1965], [Tulinov *et al.* 1965], [Gemmell and Holland 1965]. Weaker and less stable channeling effects occur for particles moving at a small angle to close-packed crystal planes.

In these notes, we follow many aspects of Lindhard's original discussion which is still the basis for our description of channeling phenomena. The string effect has turned out to be by far the most useful phenomenon, with a number of important applications, for example to the study of crystal damage during ion implantation and lattice location of the implanted impurity and to the measurement of very short nuclear lifetimes.

Several comprehensive reviews have been published over the years. Gemmell's review [Gemmell 1974] and the book [Feldman *et al.* 1982] are particularly useful with extensive bibliography.

A special chapter in the development is channeling of electrons and positrons [Uggerhøj 1966], [Uggerhøj and Andersen 68]. Owing to their low mass, there are

quantum corrections to the classical channeling theory for these particles [Lervig *et al.* 1967], and channeling phenomena have provided a number of illustrations of the correspondence between quantal and classical descriptions [Andersen *et al.* 1977]. In recent years, this field has experienced a renaissance due to the discovery of channeling radiation connected to the oscillations of channeling trajectories [Andersen *et al.* 1983].

The first 18 chapters of the notes and the introduction above were written in about 1990 but I have recently revisited and amended the notes. Still, some of the text refers to the situation 25 years ago. A couple of figures in Ch. 18 I could not locate but I left the informative references to them in the text. I have not for many years taught the course on channeling and am now since 2011 retired. However, prompted by my long-time collaborator and good friend Ejvind Bonderup, I decided to make the notes available in electronic form. Although there is not any longer much new research on basic channeling and blocking phenomena, the applications are still very important and the notes can perhaps be a useful introduction to the field.

Aarhus, December 2014
Jens Ulrik Andersen

2. DIRECTIONAL EFFECTS

The penetration of charged particles through solids is often treated as penetration through a dense gas, i.e., the atoms are assumed to be randomly distributed, and Poisson statistics can then be applied to calculate the probabilities for processes such as small-angle scattering and energy loss.

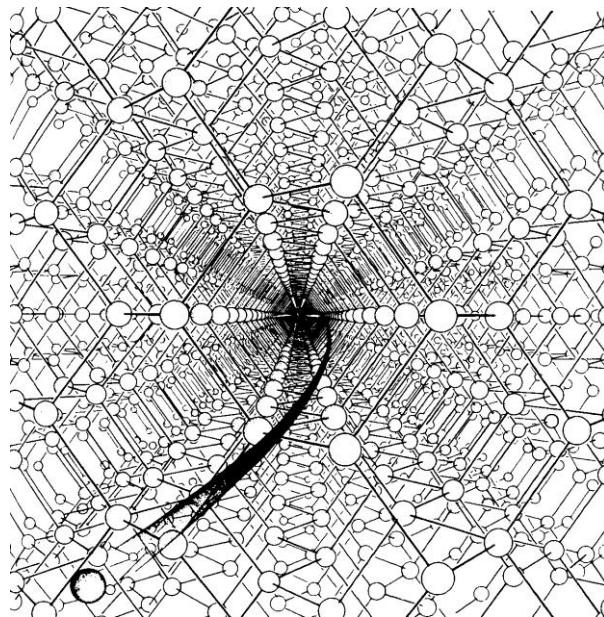


Fig. 1. Artist's concept of the channeling process on a microscopic scale. From [Brandt 1968].

A well known exception is coherent *Bragg scattering* of electrons by crystals. At the Bragg angle,

$$\theta_B = \frac{g}{2K}, \quad (1)$$

where g is a reciprocal-lattice vector, related to a planar spacing d through $g = 2\pi/d$, and $\hbar K$ is the electron momentum, the scattered amplitudes from different planes interfere constructively, and a very strong and sharp peak in scattering-yield results. But for the typical ions we shall be considering, MeV protons or alpha particles, such interference effects are very weak. Owing to their large mass M_1 , the Bragg angles are exceedingly small,

$$\theta_B = \frac{\pi \hbar}{d M v} = \pi \left(\frac{m_0}{M} \right) \left(\frac{v_0}{v} \right) \left(\frac{a_0}{d} \right), \quad (2)$$

where m_0 is the electron mass, $v_0 = e^2/\hbar$ is the Bohr velocity, and a_0 the Bohr radius, $a_0 = 0.53 \text{ \AA}$. For 1 MeV protons, $\theta_B \leq 10^{-4}$. As we shall see, the characteristic angles for channeling are larger by two orders of magnitude. In addition, the mean-free path for inelastic scattering is very short, of the order of a few lattice spacings, and interference effects are therefore restricted to very short path lengths for MeV ions.

This makes it more natural to think of the projectile as a classical, localised particle, and one could imagine enhanced penetration through crystals to result from *geometrical transparency*, as illustrated in Fig.1. Between the rows of atoms there is an open channel, allowing unhindered passage of the projectile. In fact, the name channeling originates in such a (mis-) conception.

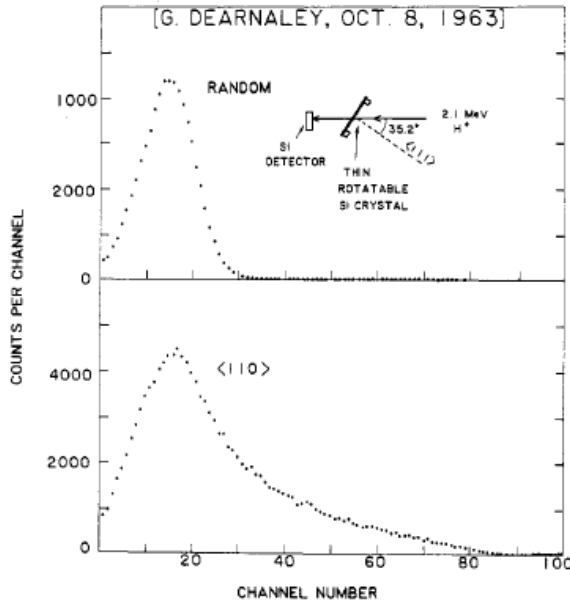


Fig. 2. Energy spectra of 2.1-MeV H^+ transmitted through a 30- μm Si crystal for random (upper) and $\langle 110 \rangle$ incidence (lower). From [Davies 1983].

However, Fig. 2 shows a measurement of the energy loss of 2.1-MeV protons in a 30- μm thick Si crystal, measured for incidence in a 'random' direction (i.e., not parallel to any strong crystal axis or plane) and for incidence parallel to a $\langle 110 \rangle$ axis. The random spectrum is, as expected, nearly symmetric and broadened by straggling in energy loss. But the aligned spectrum exhibits a long tail towards higher energies (small energy loss), and the average energy loss is clearly smaller. A simple argument shows that this effect cannot be explained by transparency. The energy loss is due to excitation of atoms in the crystal by passing ions, and if the ions are moving on straight lines, perhaps with random, small deflections, every crystal atom is subjected to the same ion flux for 'random' and aligned incidence. The total energy deposited in the crystal, and hence the average energy loss per ion, is therefore the same in the two cases. Consequently, the experiment tells us that the ion flux is modified by the lattice. The ion motion is *governed* by the lattice.

The governing of the ion motion must be due to correlation of deflection by crystal atoms. A simple cubic crystal is illustrated in Fig. 3. For ion incidence along an axis, the projectiles are moving nearly parallel to atomic strings, characterised by an atomic spacing d . We shall choose the axis as z -direction and denote the transverse coordinates $\mathbf{r} = (x, y)$. Also for motion nearly parallel to a crystallographic plane, there is correlation between collisions with atoms in an atomic plane (note the two meanings of 'plane'). For a number of collisions, the distance x from the plane will be nearly the same. A plane is characterised by a spacing d_p between the atomic planes and a corresponding density of atoms Nd_p , where N is the density of atoms in the crystals. The x - and y -coordinates in the plane may be chosen as in Fig. 3, i.e., parallel to two perpendicular axes in the plane. Sometimes it is convenient to choose the z -axis parallel to ion motion, or rather to its projection on the plane, and the x -axis perpendicular to the plane.

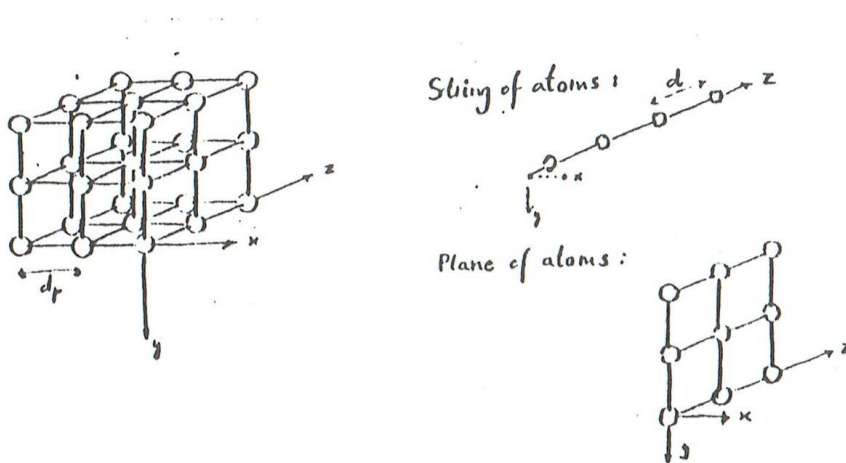


Fig. 3. Geometry of simple cubic crystal.

To characterise axes and planes, we use Miller indices. For example, the $[1\bar{1}0]$ axis is parallel to the vector $(1, -1, 0)$ in the xyz coordinate system in Fig. 3, and the $(1\bar{1}0)$ plane is perpendicular to this vector. There are many (here six) equivalent axes and planes, and to indicate a family of axes or planes, we use different parentheses, a

$\langle 110 \rangle$ axis and a $\{110\}$ plane. Note that it is not customary in channeling literature to require the vector to be a reciprocal-lattice vector. For example, the lowest-order reciprocal-lattice vector parallel to the vector $(1, -1, 0)$ is $(2\bar{2}0)$ in a face centred cubic lattice, where the distance between neighbouring atomic planes perpendicular to this vector is $d/2\sqrt{2}$. (These conventions are far from always followed!)

3. DEFLECTION BY ATOM

The steering of the ions is due to small-angle scattering by atoms, as illustrated in Fig. 4 for the axial case. The scattering can be described through an ion-atom potential $V_a(\mathbf{R})$ which is a screened Coulomb potential. The strength of the Coulomb interaction can be characterised by the dimensionless parameter κ ,

$$\kappa = \frac{2Z_1Z_2e^2}{\hbar v} = 2Z_1Z_2 \left(\frac{v_0}{v} \right), \quad (3)$$

where Z_1e and Z_2e are the nuclear charges. Bohr concluded from a wave packet analysis of the scattering that a classical description is valid for $\kappa > 1$, while for $\kappa <$

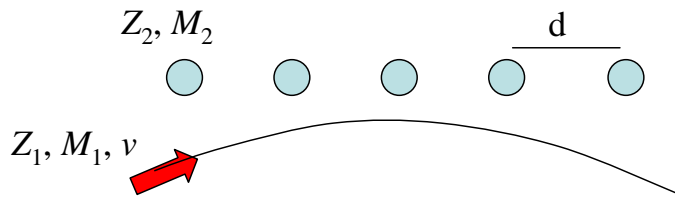


Fig. 4. Governing of ion path by correlated collisions with atoms on the string.

1, the scattering is so weak that a quantal perturbation treatment may be applied (Born approximation) [Bohr 1948]. For a typical case, 1-MeV protons in Si, we have $\kappa = 4.5$ and a classical picture of the deflection should be reasonable.

Clearly, for very high energies, κ becomes small in this case, $\kappa = 0.2$ for $v = c$. Furthermore, as pointed out by Lindhard, the requirement $\kappa > 1$ for a classical description is replaced by a stronger condition for scattering in a screened Coulomb field,

$$\kappa > 1 + \left(\frac{q}{a} \right)^2, \quad (3a)$$

where q is the impact parameter and a the Thomas-Fermi screening distance $a = 0.8853Z_2^{-1/3}a_0$. For governing of channeled particles, q is typically larger than a .

It was therefore a very important step in Lindhard's analysis of channeling to show that the application of classical mechanics is not limited by the inequality (3a). The reason is that for a collision with a string of atoms, as illustrated in Fig. 4, the scattering object is not a single atom but several atoms. Qualitatively, the charge Z_2e in Eq. (3) should therefore be replaced by the combined charge of the atoms that are active in the deflection. As it turns out, a classical description of the deflection by a string of atoms then remains valid at all projectile velocities provided the projectile mass is

large compared with the electron mass (see also [Andersen 1985]) . We shall later discuss separately the special cases of electron and positron channeling.

An instructive argument illuminating the result indicated above is provided by the following transformation [Lindhard 1965]: Consider a particle with velocity v approaching a string at angle ψ . In the frame of reference following the longitudinal motion of the particle, the transverse motion is governed by collisions with velocity $v_z \sim v$ at time intervals $\tau = d/v$. If we increase the velocity to $2v$, while reducing the angle to $\psi/2$ to keep the transverse energy fixed, the transverse motion is nearly unchanged. The momentum transfers in individual collisions are smaller by a factor of two, but this is compensated for by the reduction of the time interval between collisions to $\tau/2$. The same transformation of the transverse motion could be obtained without changing the velocity or angle by cutting the atoms in two and displacing one half a distance $d/2$ along the string. Hence it is clear that in the limit $v \rightarrow \infty$, the description approaches the continuum picture introduced in the following section.

The continuum-string potential may for cursory estimates be represented by a two-dimensional Coulomb potential, Eq. (23a), $U(r) \sim (Z_1 Z_2 e^2/r)(a/d)$. We may then for the transverse motion introduce Bohr's κ parameter³ which becomes

$$\kappa_{\perp} = \frac{2Z_1 Z_2 e^2}{\hbar v \psi} \left(\frac{a}{d} \right) .$$

For channeled particles, $\psi < \psi_1 = (2Z_1 Z_2 e^2/Ed)^{1/2}$ (Eq. (29)), and hence

$$\kappa_{\perp} \geq \left[Z_1 Z_2^{1/3} \frac{M_1}{m_0} \right]^{1/2} ,$$

which is large compared to unity for particles with mass M_1 much larger than the electron mass m_0 . Thus the transverse motion can be described classically according to Bohr's analysis. In conclusion, in the limit $v \rightarrow \infty$, the deflection by a string can be treated classically, although Bohr's κ becomes small for individual collisions with string atoms.

For correlated scattering by atoms in a string or strings in a plane, we are concerned only with very small deflections in the single scattering events, and the classical description of an ion-atom collision is then very simple. The relative motion may be described as the motion of a particle with the reduced mass M_0 in the potential $V_a(\mathbf{R})$. Since the path is nearly a straight line, we may apply the impulse approximation to obtain the momentum transfer,

$$\begin{aligned} \Delta p &\cong - \int_{-\infty}^{\infty} dt \frac{\partial}{\partial q} V_a(\sqrt{q^2 + (vt)^2}) = - \frac{1}{v} \frac{\partial}{\partial q} \Gamma(q) , \\ \Gamma(q) &= \int_{-\infty}^{\infty} dz V_a(\sqrt{q^2 + z^2}) . \end{aligned} \quad (4)$$

The scattering angle θ in the centre-of-mass frame is given by $\theta \sim \Delta p/M_0 v$, and the laboratory scattering angle φ is obtained from $\tan \varphi = M_2 \sin \theta / (M_1 + M_2 \cos \theta)$,

$$\varphi \cong \frac{M_2}{M_1 + M_2} \theta \cong \frac{\Delta p}{M_1 v} . \quad (5)$$

The momentum transfer $M_1 v \varphi$ in the laboratory is thus the same as in the CM system Eq. (4), which is not surprising since it is nearly perpendicular to the velocity. The conclusion is that for small-angle scattering, we may calculate deflection angles as if the atoms were fixed in space, i.e., as scattering in a fixed, external potential. Note that the formulas in Eqs. (4) and (5) also apply for a relativistic particle if M_1 is replaced by the relativistic mass $M_1 \gamma$.

4. CONTINUUM POTENTIAL

We shall now show that a particle which, as illustrated in Fig. 4, is deflected by a number of correlated collisions with atoms on a string, to a good approximation moves as it were under the influence of a continuum string potential obtained by averaging the potential in the axial (z) direction,

$$U(\mathbf{r}) = \frac{1}{d} \int_{-d/2}^{d/2} dz \sum_{j=-\infty}^{\infty} V_a(\sqrt{r^2 + (z - jd)^2}) = \frac{1}{d} \int_{-\infty}^{\infty} dz V_a(\sqrt{r^2 + z^2}) . \quad (6)$$

The average potential U is proportional to the function Γ introduced in Eq. (4), and hence the momentum transfer $\Delta \mathbf{p}_i$ in the i 'th collision may be expressed as

$$\Delta \mathbf{p}_i = -\tau \nabla U(\mathbf{r}), \quad \mathbf{r} = \mathbf{q}_i, \quad (7)$$

where $\tau = d/v$ is the time interval between collisions. We have here used the fact that the motion is nearly parallel to the string and $\Delta \mathbf{p}_i$ therefore is nearly perpendicular to the string.

In the continuum picture, where the motion is governed by the potential $U(\mathbf{r})$, the momentum transfer during the time interval τ , corresponding to passage from a distance $d/2$ in front of the atom to a distance $d/2$ behind it, is given by

$$\Delta \mathbf{p}_i = - \int_{-\tau/2}^{\tau/2} dt \nabla U(\mathbf{r}(t)) . \quad (8)$$

If the variation of $\mathbf{r}(t)$ is small, $|\mathbf{r}(\frac{\tau}{2}) - \mathbf{r}(-\frac{\tau}{2})|/r(0) \ll 1$, this is a good approximation to Eq. (7).

In the continuum approximation, Eq. (8), the momentum transfer is exactly perpendicular to the axis. Introducing the notation $\mathbf{p}_\perp = (p_x, p_y)$, the equations of the motion may be expressed as

$$\begin{aligned} \frac{d}{dt} \mathbf{p}_\perp &= -\nabla U(\mathbf{r}) \\ \frac{d}{dt} p_z &= 0 \end{aligned} , \quad (9)$$

with the understanding that they should be applied only for time intervals longer than τ . The transverse energy and the longitudinal momentum are then conserved,

$$\begin{aligned} E_{\perp} &= \frac{p_{\perp}^2}{2M_1} + U(\mathbf{r}) = \text{const.} \\ p_z &= \text{const.} \end{aligned} \quad (10)$$

For relativistic particles, the equations also apply with high accuracy with the replacement $M_1 \rightarrow \gamma M_1$.

The two-dimensional potential surface is illustrated in Fig. 5. Only close to the string is U given by Eq. (6). In general, we have

$$U(\mathbf{r}) = \frac{1}{d} \int_{-d/2}^{d/2} V_c(\mathbf{r}, z) dz. \quad (11)$$

If the crystal potential V_c may be expressed as a sum of atomic potentials, U becomes a superposition of string potentials (6), illustrated in Fig. 5.

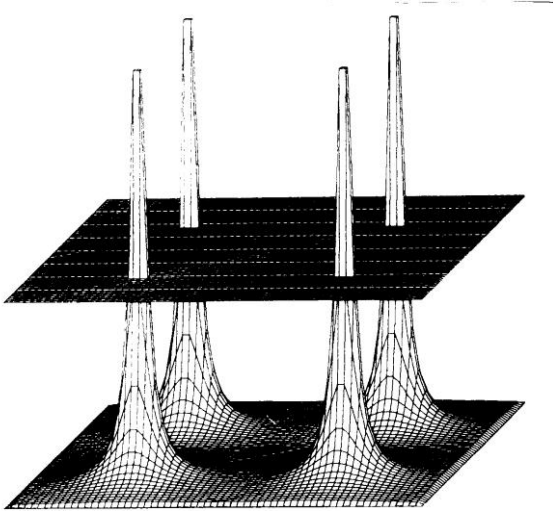


Fig. 5. Axial continuum potential. The transverse unit cell is the area within the centre of the four strings. An additional plane has been included to show the forbidden regions for a particle with fairly high transverse energy.

The particle motion is confined to the region where $E_{\perp} > U(r)$ and we denote the allowed area per unit cell by $A(E_{\perp})$ (total area of unit cell A_0). If E_{\perp} is below the maximum of the potential, there is a minimum distance of approach r_m , and a corresponding forbidden area πr_m^2 around strings. Such a channeled particle therefore cannot come very close to the centre of atoms, and 'close-encounter processes' such as nuclear reactions or Rutherford backscattering are forbidden.

Also for planes we may introduce a continuum potential which in effect governs the motion when many atoms contribute to the deflection from an atomic plane. It is obtained as an average of the crystal potential over the two dimensions parallel to the plane,

$$V(x) = \frac{1}{A} \int_A dy dz V_c(x, y, z). \quad (12)$$

Close to an atomic plane, V may in analogy to Eq. (6) be approximated by the potential from a single plane,

$$V(x) = \frac{1}{A} \int_A dydz V_a(\sqrt{x^2 + y^2 + z^2}), \quad (13)$$

and the potential in Eq. (12) may to a good approximation be expressed as a sum of contributions (Eq. (13)) from different atomic planes.

The motion may be decomposed in free propagation parallel to the plane and x -motion with conserved energy,

$$E_{\perp} = \frac{p_x^2}{2M_1} + V(x), \quad (14)$$

which for $E_{\perp} < V_{\max}$ is a periodic oscillation between a pair of neighbouring atomic planes.

5. ATOMIC POTENTIAL

For high velocity v and low-charge Z_1 , the strength parameter κ defined in Eq. (3) is small for collisions with electrons ($|Z_2| = 1$), and the passage of a projectile is a weak perturbation. The atomic potential is then simply the expectation value of the Coulomb interaction in the electronic ground state Ψ_0 , and with the electrons at positions \mathbf{R}_i we obtain

$$V_a(R) = \langle \Psi_0 | \sum_i \frac{-Z_1 e^2}{|\mathbf{R} - \mathbf{R}_i|} + \frac{Z_1 Z_2 e^2}{R} | \Psi_0 \rangle . \quad (15)$$

Relativistic Hartree-Fock calculations give very accurate atomic wave functions, and the results have been tabulated. Useful are Doyle and Turner's analytical fits to the scattering factor,

$$f(s) = \frac{2m_0}{\hbar^2} \int_0^{\infty} R^2 V_a(R) \frac{\sin(4\pi s R)}{4\pi s R} dR = \sum_{i=1}^4 a_i \exp(-b_i s^2) \quad (\text{fit}). \quad (16)$$

The parameters a_i and b_i are tabulated [Doyle and Turner1968].

This approximation leads to simple analytical forms of the axial and planar potentials. The approximation by four Gaussians in Eq. (16) is accurate only for not too large s ($s < 2 \text{ \AA}^{-1}$), and therefore the potentials will be inaccurate at small distances. However, here the continuum potentials are modified by thermal vibrations. The vibrations of an atom usually lead to a nearly isotropic Gaussian distribution,

$$dP(r_a) = \varrho^{-2} \exp\left(-\frac{r_a^2}{\rho^2}\right) d(r_a^2) , \quad (17a)$$

$$dP(x_a) = (\pi\rho^2)^{-1/2} \exp\left(-\frac{x_a^2}{\rho^2}\right) dx_a \quad (17b)$$

of the displacements \mathbf{r}_a from a string and x_a from an atomic plane. The continuum potentials should be convoluted with these distributions, leading to the thermally averaged potentials U_T and V_T ,

$$U_T(\mathbf{r}) = \int \frac{d^2\mathbf{r}_a}{\pi\rho^2} \exp\left(-\frac{r_a^2}{\rho^2}\right) U(|\mathbf{r} - \mathbf{r}_a|) \quad (18a)$$

and

$$V_T(x) = \int_{-\infty}^{\infty} \frac{dx_a}{\sqrt{\pi\rho^2}} \exp\left(-\frac{x_a^2}{\rho^2}\right) V(x - x_a). \quad (18b)$$

These convolutions correspond to multiplication of the scattering factor $f(s)$ by a Debye-Waller factor $\exp(-(2\pi)^2\rho^2s^2)$, and this is very simple to include in the expansion (16). For $s > 2 \text{ \AA}^{-1}$, the Debye-Waller factor is very small (ρ is usually of order 0.1 \AA) and the inaccuracy in this region is therefore not important for the thermally averaged potentials (with new notation, $B_i = b_i/(2\pi)^2$):

$$U_T(r) = \frac{2e^2a_0}{d} \sum_{i=1}^4 \frac{a_i}{B_i + \rho^2} \exp\left(-\frac{r^2}{B_i + \rho^2}\right), \quad (19a)$$

$$V_T(x) = 2\sqrt{\pi}e^2Nd_p a_0 \sum_{i=1}^4 \frac{a_i}{\sqrt{B_i + \rho^2}} \exp\left(-\frac{x^2}{B_i + \rho^2}\right). \quad (19b)$$

Being based on atomic Hartree-Fock calculations, these expressions represent the potentials from charge distributions for free atoms, but the corrections in solids for bonding, etc., are very small, and their influence has been identified only in the most accurate channeling measurements [Andersen *et al.* 1982].

Much more important are perturbations of the charge distribution by the projectile when the κ parameter is not very small. Such effects can be taken into account by a Z_1 dependence of the screening of the nuclei by atomic electrons, as is usually done in the Thomas-Fermi-type estimates of the interaction potential $V_a(\mathbf{R})$.

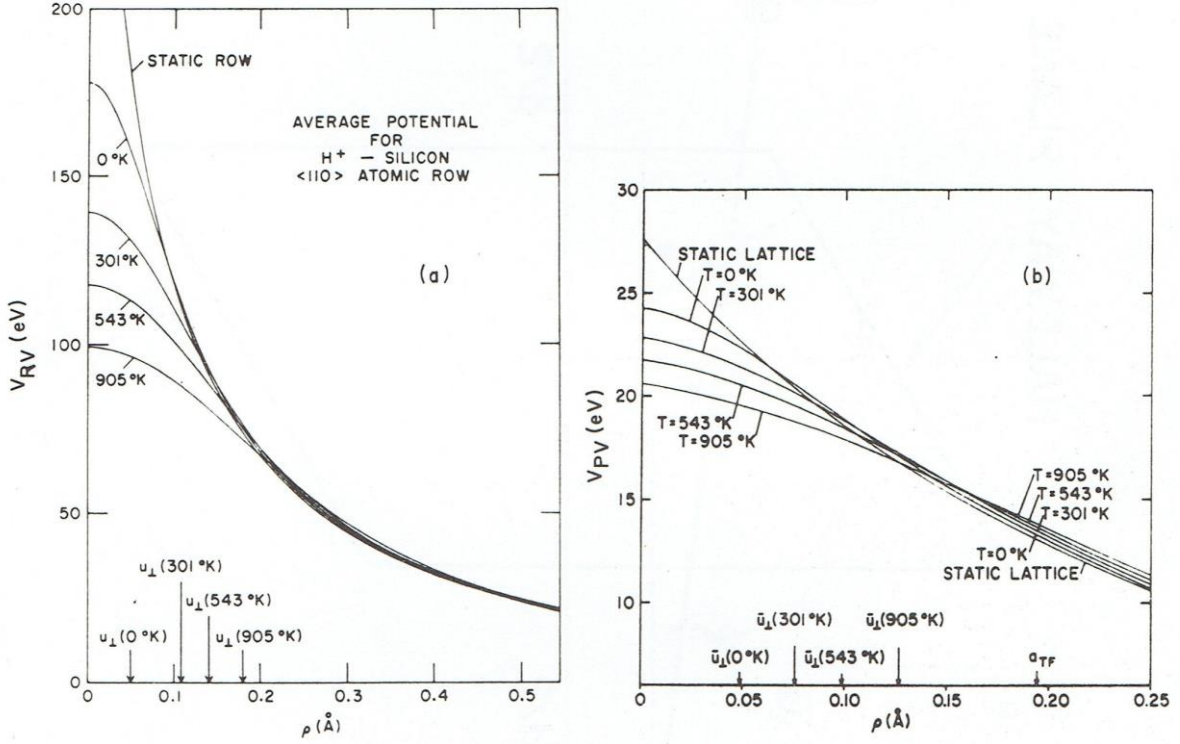


Fig. 6. Thermally averaged continuum potentials derived from the Molière approximation to the T-F potential for (a) a $\langle 110 \rangle$ string and (b) a $\{110\}$ plane. The symbol ρ here denotes the distance from the string or plane, and u_{\perp} and \bar{u}_{\perp} denote the vibrational amplitude in two and one dimensions, respectively (from [Appleton *et al.* 1967]).

For simple general estimates, the Thomas-Fermi picture is very useful, leading to a simple scaling with atomic number,

$$V_a(R) = \frac{Z_1 Z_2 e^2}{R} \varphi\left(\frac{R}{a}\right), \quad (20)$$

where a is the Thomas-Fermi screening radius, $a = 0.8853 a_0 Z_2^{-1/3}$ for an undisturbed atom. Reasonable limits for the function φ are $\varphi \rightarrow 1$ for $R \rightarrow 0$ and $\varphi \rightarrow 0$ for $R \rightarrow \infty$. For a collision between two atoms both carrying many electrons the screening may be represented by a modified value of a ,

$$a = 0.8853 a_0 (Z_1^{2/3} + Z_2^{2/3})^{1/2}. \quad (21)$$

For highly stripped ions at high velocity the correction to a is smaller [Andersen *et al.* 2008]. A very accurate representation of the Thomas-Fermi potential is the Molière approximation, but we shall use the much simpler ‘standard potential’ [Lindhard 1965],

$$V_a(r) = \frac{Z_1 Z_2 e^2}{R} \left[1 - \left(1 + \left(\frac{C a}{R} \right)^2 \right)^{-1/2} \right], C \cong \sqrt{3}. \quad (22)$$

It leads to a simple analytical expression for the continuum string potential,

$$U(r) = \frac{Z_1 Z_2 e^2}{d} \log \left(\frac{(Ca)^2}{r^2} + 1 \right). \quad (23)$$

At distance $r \sim a$, U is nearly proportional to r^{-1} and we may in simple estimates use the approximation

$$U(r) \cong \frac{Z_1 Z_2 e^2 a}{r d}. \quad (23a)$$

For a single plane, one obtains with the standard potential

$$V(x) = 2\pi Z_1 Z_2 e^2 N d_p [(Ca^2 + x^2)^{1/2} - x]. \quad (24)$$

The expressions are not so convenient when the thermal average in Eq. (18) is included but for distances larger than ρ we can often ignore this modification. Note that as a consequence of the R^{-1} dependence of V_a at small distances, the static string potential diverges logarithmically for small r . The smearing in Eq. (18) leads to a finite maximum, $U_T(0) \cong U(\rho/\sqrt{2})$. For planes, already the static potential is finite but the sharp cusp at $x = 0$ is rounded by the smearing. These effects are illustrated in Fig. 6 for the Molière approximation to the potential for protons in Si.

6. CRITICAL ANGLES

When the continuum string potential was introduced, we noted that the condition for applying this potential to calculate the projectile path is that the relative change of the distance to the string be small over a penetration distance d , i.e., during the corresponding time $\tau = d/v$. For the continuum picture to be self-consistent, the trajectory calculated from the equation of motion in Eq. (9) must fulfil this condition.

For a particle approaching a string at an angle ψ the minimum distance in the collision depends on the impact parameter l in the transverse plane, $r_m = r_m(\psi, l)$. The condition formulated above may be written approximately as

$$d\psi < r_m(\psi, l). \quad (25)$$

Since the right-hand side decreases with increasing ψ , the inequality sets an upper limit to ψ . The condition is most restrictive for $l = 0$, which case is therefore considered in the following.

At $r_m(\psi, 0)$, the transverse kinetic energy, $E_{\perp} = (p \sin \psi)^2 / 2M_1 \cong E\psi^2$, where p is the momentum and E the energy of the projectile (for relativistic particles, $E \equiv \frac{1}{2}pv$ instead), is transformed into the potential energy,

$$U(r_m) = E\psi^2. \quad (26)$$

Since $U(r)$ is a decreasing function, the inequality in Eq. (25) may be expressed as

$$E\psi^2 < U(d\psi). \quad (27)$$

Introducing the standard potential in Eq. (23), we obtain

$$E\psi^2 < E\psi_1^2 \cdot \frac{1}{2} \log \left(\left(\frac{ca}{d\psi} \right)^2 + 1 \right), \quad (28)$$

where the angle ψ_1 is given by

$$\psi_1 = \left(\frac{2Z_1Z_2e^2}{Ed} \right)^{1/2}. \quad (29)$$

(The factor of two included for historical reasons)

We may now distinguish between two energy regimes corresponding to

$$\begin{aligned} \psi_1 < \frac{a}{d} &\leftrightarrow \text{high energies} \\ \psi_1 > \frac{a}{d} &\leftrightarrow \text{low energies} \end{aligned} \quad (30)$$

At high energies, the logarithm in Eq. (28) is large and slowly varying at $\psi \sim \psi_1$. For increasing ψ , the inequality is broken at an angle of this order, and we may insert $\psi = \psi_1$ in the logarithm to obtain

$$\psi < \psi_1 \left[\frac{1}{2} \log \left(\left(\frac{ca}{d\psi_1} \right)^2 + 1 \right) \right]^{1/2} \quad (31)$$

The factor on ψ_1 is never very large compared to unity, and ψ_1 is often called Lindhard's critical angle for channeling. We note that the minimum distance of approach corresponding to the limiting angle in Eq. (31) is $r_m \sim d\psi_1$.

At low energies, the logarithm is small for $\psi \sim \psi_1$, and the inequality in Eq. (28) is broken already at somewhat smaller angles. Expanding the logarithm, we obtain

$$\psi^2 < \frac{1}{2} \psi_1^2 \left(\frac{ca}{d\psi} \right)^2 \quad \text{or} \quad \psi < \left(\psi_1 \frac{ca}{\sqrt{2}d} \right)^{1/2}. \quad (32)$$

At low energies, the critical angle varies more slowly with energy, $\propto E^{-1/4}$, compared with $\psi_1 \propto E^{-1/2}$.

The inclusion of thermal vibration in the description modifies this picture. The main consequence of channeling, the extinction of close-encounter processes, disappears when a particle can penetrate to a distance $\sim \rho$ from a string (root-mean-square displacement in 2D). In the continuum approximation, this is possible unless the transverse energy is lower than $\sim U(\rho)$, and we obtain as a condition for ‘channeling’

$$E\psi^2 < U(\rho)$$

or, with the standard potential,

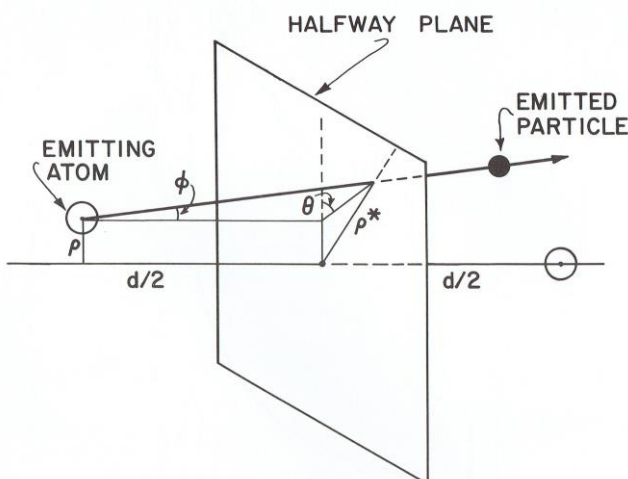
$$\psi < \psi_1 \left[\frac{1}{2} \log \left(\left(\frac{Ca}{\rho} \right)^2 + 1 \right) \right]^{1/2}. \quad (33)$$

At high energies, defined now by the condition

$$\rho > d\psi_1, \quad (34)$$

the inequality in Eq. (33) is more restrictive than Eq. (31). The picture then becomes particularly simple since we may apply the continuum description for all angles ψ in calculations of the yield of close-encounter processes. The accuracy of this description is illustrated in the following section by a comparison with Monte-Carlo simulations.

The transition between high and low energies can be studied in the half-way-plane model, illustrated in Fig. 7 for emission of a particle from an atom displaced by a distance r from a string (r denoted ρ in the figure). Here we consider the reverse process of a particle moving from right to left and hitting a string atom. The particle is approaching the string at angle ψ , i.e. with transverse energy $E\psi^2$, and for the motion along the string it is assumed that the transverse energy is conserved at the xy -planes halfway between two string atoms. Although the potential from a static string in Eq. (23) diverges for $r \rightarrow 0$, it is in this model possible to hit a string atom for a finite value of ψ .



Let us consider a trajectory at an angle ψ to the string for large r and terminating in a string atom at $r = 0$. The angle to the string of the motion just before hitting the atom is denoted ϕ , and the distance from the string at the halfway plane in front of this atom is $\phi d/2$. Conservation of E_{\perp} leads to the relation

Fig. 7. Emission of particle from string atom. The transverse energy is determined at the plane halfway between string atoms. From [Gemmell 1974].

$$E\psi^2 = E\varphi^2 + U\left(\frac{\varphi d}{2}\right).$$

For large φ , the first term on the right-hand side becomes large, and for small φ , the potential diverges. To find the intermediate minimum value of $E\psi^2$, we differentiate with respect to $E\varphi^2$ and use the expression in Eq. (23) for U ,

$$0 = 1 - \frac{\psi_1^2}{2} \frac{1}{\left(\frac{2Ca}{\varphi d}\right)^2 + 1} \left(\frac{2Ca}{d}\right)^2 \varphi^{-4},$$

with the solution

$$\varphi^2 = 2 \left(\frac{Ca}{d}\right)^2 \left[-1 + \left(1 + \frac{1}{2} \left(\frac{d\psi_1}{Ca}\right)^2\right)^{1/2} \right].$$

Again we may consider the two limits, ψ_1 small or large compared to (Ca/d) . At high energies, we obtain by expanding the square root to first order, $\varphi^2 \sim \psi_1^2/2$, and this leads to

$$\psi \geq \psi_1 \frac{1}{\sqrt{2}} \left[1 + \log \left(\left(\frac{2\sqrt{2}Ca}{d\psi_1} \right)^2 + 1 \right) \right]^{1/2},$$

which is consistent with the upper limit in Eq. (31) for correlated deflection from a string in the high-energy region (since it is slightly larger).

For low energies, $\varphi^2 \sim \sqrt{2}\psi_1(Ca/d)$, and the lower limit becomes

$$\psi \geq \left(2\sqrt{2}\psi_1 \frac{Ca}{d} \right)^{1/2}$$

which is larger than the upper limit in Eq. (32) by a factor of two.

When thermal vibrations are included in the halfway-plane model, a numerical calculation is needed to find the critical angle for hitting atoms. The result of such a calculation is illustrated in Fig. 8. At high energies, $d\psi_1 < \rho$, the critical angle is given by Eq. (33) (with a small correction, see Eq. (56)). There is no difference between the continuum model and the halfway-plane model. At low energies, $d\psi_1 > \rho$, the discreteness of the string becomes important. The ions can ‘sneak in’ between neighbouring string atoms. The thermal vibrations are here less important, the critical angle being close to the result obtained for the static string.

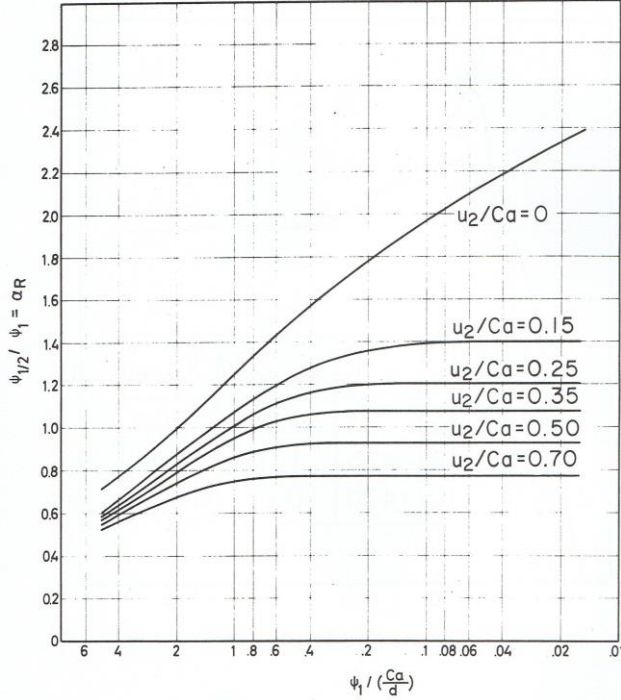


Fig. 8. Numerical calculation of the halfwidth $\psi_{1/2}$ of the axial dip in yield, using the halfway-plane model with the standard potential. The root mean square two-dimensional vibrational displacement is here denoted u_2 . The lower curves should be lifted by 0.05 to correct for a rounding-off error in [Andersen 1967].

It is also worth noting that scattering by continuum strings may be observed for angles larger than the critical angle given by Eq. (31) or (33), for example in measurements of transmission through thin crystals. Scattering with conservation of the angle to an axis leads to the formation of a so-called doughnut pattern. One should therefore be careful in applications of the distinction between *random beam* and *aligned beam*, introduced by Lindhard as corresponding to angles ψ larger or smaller, respectively, than the limit given by Eq. (31) or (33). Particles in random beam give a yield of close-encounter processes as in a random target, but the multiple scattering is strongly modified by the doughnut scattering.

For planar channeling, the correlation between deflections is much less well defined, and an analysis of the self-consistency of the continuum picture is not so straightforward. From the potential in Eq. (24) we may, however, define a characteristic angle corresponding to $E\psi^2 = V(0)/\pi$,

$$\psi_p = \psi_1 \left(\frac{ca}{d_s} \right)^{1/2}. \quad (35)$$

Here ψ_1 is the Lindhard angle in Eq. (29) for an axis with atomic spacing d in the strings separated in the plane by d_s , i.e. $Nd_p d d_s = 1$. The critical angle is clearly somewhat smaller for planar than for axial channeling, by a factor of order 2-3.

7. THERMAL VIBRATIONS

As we have seen, the thermal vibrations play a crucial role in channeling phenomena. The vibrations lead to irregular displacements of atoms from their equilibrium positions, seen as static displacements by the swift projectiles. We may distinguish between three consequences:

1. Displacements from strings or planes of the atomic nuclei that the projectiles must hit to produce a nuclear reaction, for example.
2. Thermal smearing of continuum potentials.
3. Fluctuations of the repulsive force from the atoms on a string or plane, leading to non-conservation of transverse energy and 'dechanneling'.

The first effect is very important at high energies for the critical angle, as shown in Fig. 8. The thermal smearing is in comparison a small correction. A comparison with Monte-Carlo simulations of dips is shown in Fig. 9. These calculations demonstrate a remarkable accuracy of the approximation of transverse-energy conservation, in the continuum model at high energies, and with the restriction at low energies to conservation at halfway planes only. There is complete agreement with dips in yield obtained by Monte-Carlo simulation.

The third effect indicated above will be discussed in some detail later (Ch. 17). A combination of inelastic scattering by electrons and the thermal fluctuations in atomic deflection leads to a gradual change in transverse energy of the channeled particle and transitions from aligned to random beam ('dechanneling', Ch.18).

The static distribution of thermal displacements is Gaussian in the harmonic approximation for interatomic forces. This is easy to see in a classical picture of a harmonic oscillator in equilibrium with a heat bath at temperature T . The density in phase space is proportional to a Boltzmann factor $\exp(-E/kT)$, or

$$dP(\mathbf{R}_a, \mathbf{P}_a) \propto \exp\left(-\left(\frac{P_a^2}{2M_2} + \frac{1}{2}M_2\omega^2 R_a^2\right)/kT\right) d^3\mathbf{R}_a d^3\mathbf{P}_a. \quad (36)$$

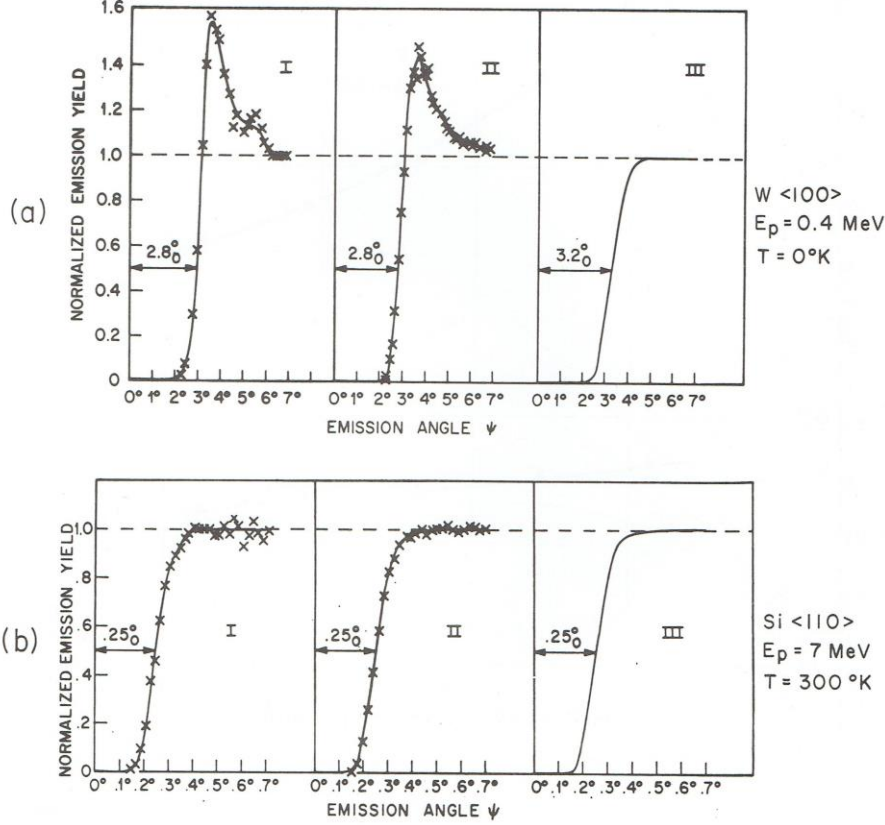


Fig. 9. Comparison of axial dip in yield for static string with dip for a vibrating atom in a static string. The calculations were made by Monte-Carlo collisions (I), in the halfway-plane model (II), and in the continuum model (III). The value of the parameter $\rho/d\psi_1$ is 0.55 (a) and 8.1 (b), respectively. With all atoms vibrating (I) and with a thermally averaged potential in (II) and (III), a similar agreement was found, the width being reduced by 5% in case (b). From [Andersen and Feldman 1970].

Integration over the momentum \mathbf{P}_a of the atom and over one or two of the coordinates leads to the Gaussian distributions in Eqs. (17a) and (17b), with mean-square vibrations in two dimensions,

$$\rho^2 = \frac{2kT}{M_2\omega^2}. \quad (37)$$

(Often ρ is called the vibrational amplitude). By a straightforward (but somewhat lengthy) calculation [Feldman 1967], one can show that a Boltzmann distribution over energy results in a Gaussian spatial distribution also for a quantum oscillator, with a mean-square displacement in two dimensions, given by

$$\rho^2 = \frac{\hbar}{M_2\omega} / \tanh\left(\frac{\hbar\omega}{2kT}\right). \quad (38)$$

For low temperatures, $kT \ll \hbar\omega$, this expression reduces to the mean-square displacement $\hbar/M_2\omega$ of zero-point motion in the ground state, and at high temperatures, $kT \gg \hbar\omega$, we regain the classical result in Eq. (37). A picture of the solid as a

collection of independent harmonic oscillators with the same frequency is usually referred to as the Einstein model.

In a real solid, the atomic oscillators are of course coupled, but if the interatomic forces are harmonic, the displacement distribution for an atom will still be Gaussian. This is easy to show through a linear transformation to normal coordinates which behave as uncoupled harmonic oscillators with Gaussian statistical distributions. Integration over all but one of the atomic coordinates of the combined probability function leaves a Gaussian. (Try the example of two coupled oscillators!)

In the Einstein model, correlations of the vibrations of neighbouring atoms are completely neglected. A more realistic picture is obtained in the Debye model where the vibrations are assumed to be elastic waves. For the parameter ρ^2 , one obtains

$$\rho^2 = \frac{3\hbar^2}{2M_2kT_D} \left(1 + 4 \left(\frac{T}{T_D} \right)^2 \int_0^{T_D/T} \frac{x dx}{e^x - 1} \right). \quad (39)$$

The integral in this formula is tabulated in Abramovitz and Stegun: *Handbook of Mathematical Functions*, p. 998. At high temperatures, $T \gg T_D/6$, ρ^2 is proportional to temperature,

$$\rho^2 \cong \frac{6\hbar^2 T}{M_2 k T_D^2}, \quad T \gg T_D/6, \quad (40)$$

and at low temperature, the zero-point motion dominates,

$$\rho^2 \cong \frac{3}{2} \frac{\hbar^2}{M_2 k T_D}, \quad T \ll T_D/6. \quad (41)$$

This behaviour is nearly the same as for the Einstein model, with $\hbar\omega \sim 0.6kT_D$.

The frequency spectrum of the vibrations one obtains for the Debye model is often very unrealistic, but the formula in Eq. (39) is still useful, with T_D as an empirical parameter which has been tabulated for a number of materials. However, the effective value of T_D may depend weakly on temperature.

Also for correlations of vibrations, the Debye model gives a fairly simple prediction. The correlation is weakest at low temperatures. This is at first surprising but is explained by the fact that the correlation is strongest for the low-frequency modes with long wavelength. At a finite temperature, these modes are more excited than the high-frequency modes with short wavelength (Boltzmann distribution) but at zero K only the zero-point motion is left in all modes of vibration.

The magnitude of the correlation between displacements of two atoms a and b can be characterized by a coefficient β , defined by

$$\beta = \frac{\langle x_a x_b \rangle_T}{\langle x_a^2 \rangle_T} , \quad (42)$$

where the brackets indicate a statistical (thermal) average. For a discussion of the predictions of the Debye model and a comparison to more sophisticated calculations for the diamond structure (e.g. Si), we refer to [Nielsen and Weber 1980]. For nearest neighbours in Si, the coefficient β may be as large as $\beta \sim 0.25$.

The importance of correlation is quite different for the three effects mentioned in the beginning of this section. For the displacement from a string of the atom to be hit, correlation is not very important. The correlation decreases strongly with separation between atoms a and b in Eq. (42), and only for very low energies is the scattering by the nearest neighbour on a string decisive for the distance r from the string when the projectile passes an atomic site. We may also note that for $\beta < 0.5$, the mean-square relative vibration is still larger than the individual vibrations of atoms a and b .

The second effect, the thermal smearing of continuum potentials, is not affected by correlation, but the third effect may be influenced significantly. If neighbouring pairs of atoms vibrate together, the mean-square fluctuation in deflection angle will be twice as large as for uncorrelated vibrations.

We may finally note that for planes, the correlation will normally not be important. Only when the projectile moves nearly parallel to a strong axis in the plane will it scatter off atoms with small separation. This feature has been used to study the influence of correlations on electron channeling [Andersen *et al.* 1983a].

8. MERGING OF AXIAL AND PLANAR EFFECTS

The separation between axial and planar channeling is not always as clear-cut as we have pretended until now. The merging of the two effects is illustrated in Fig. 10. The axis is at the intersection of a number of planes in the stereogram. Using the Miller indices, we can easily decide which planes. The axis is contained in a plane if it is perpendicular to the normal to the plane. As an illustration, the [111] axis is contained in the $(1, \bar{1}, 0)$, $(0, 1, \bar{1})$, $(1, 0, \bar{1})$, $(1, 1, \bar{2})$, $(1, \bar{2}, 1)$, $(\bar{2}, 1, 1)$ planes since the scalar product of the vector $(1, 1, 1)$ with, e.g., $(1, -1, 0)$ is zero. The angles between the planes may also be expressed in terms of the scalar product, e.g.,

$$\cos\theta = \frac{(1, \bar{1}, 0) \cdot (1, 0, \bar{1})}{\|(1, \bar{1}, 0)\| \|(1, 0, \bar{1})\|} = \frac{1}{\sqrt{2}\sqrt{2}} = \frac{1}{2} . \quad (43)$$

Thus the angle between the two $\{110\}$ planes is 60° .

The planes are in Fig. 10 represented by an angular interval $|\varphi| \leq \psi_p$, where φ is the angle to the plane. Axial channeling is confined to polar angles $\psi \leq \psi_1$. However, at angles $\psi \sim \psi_1$, the planar and axial channeling merge. The qualitative picture of

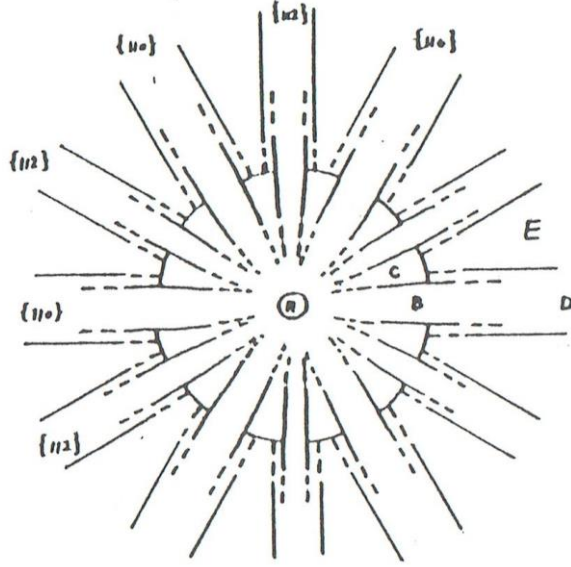


Fig. 10. Illustration of the interplay of axial and planar effects. Denoting by ψ the angle to the axis and by φ the angle to the nearest plane, we may characterise the different regions as follows:

- A: Proper channeling $\psi < \psi_1/10$.
- B: Axial channeling $\psi < \psi_1$.
- C: Governing by strings of strings $\psi \sim \psi_1$,
 $\varphi < \psi_1 [(\psi/\psi_1)(Ca/d_s)^2]^{1/3}$.
- D: Planar channeling, $\psi > \psi_1$, $\varphi \leq \psi_p = \psi_1 (Ca/d_s)^{1/2}$.
- E: Random.

planar channeling then has to be changed. The projectiles move nearly parallel to strings of atoms in the planes, and the planar potential is replaced by a superposition of string potentials. If a particle approaches a plane in between two strings, it may 'sneak in' between them and the smaller the angle ψ to the axis, the easier it will be to sneak in. The limit $\varphi < \psi_p$ is therefore in this region replaced by a lower limit which depends on the angle ψ (weakly).

The estimate given in the figure may be derived from an argument similar to the halfway-plane analysis discussed in Ch. 6. Denote by θ the azimuthal angle to a plane of the motion perpendicular to the axis (Fig. 10) for a particle hitting a string. With an approximation to the potential in Eq. (24) for $x > Ca$,

$$V(x) = \pi E \psi_1^2 N d_p dx \left[\left(\left(\frac{Ca}{x} \right)^2 + 1 \right)^{1/2} - 1 \right] \cong \frac{\pi}{2} E \psi_1^2 N d_p (Ca)^2 x^{-1},$$

the transverse energy relative to the plane, evaluated at half the distance d_s to the neighbouring string, where the particle's distance to the plane is $x = \theta d_s/2$, can be expressed as

$$E \varphi^2 \cong E \psi^2 \theta^2 + \pi E \psi_1^2 \left(\frac{Ca}{d_s} \right)^2 \theta^{-1}.$$

The minimum value for penetration of the plane is obtained by setting the derivative of this expression equal to zero. For this value the potential and kinetic energies are of similar magnitude when the potential energy in the middle of the planar channel is subtracted. Neglecting a numerical factor of about 1.7 (as in the definition of ψ_p in Eq. (35)), we obtain as a condition for planar channeling,

$$\varphi < \psi_1 \left[\left(\frac{\psi}{\psi_1} \right) \left(\frac{Ca}{d_s} \right)^2 \right]^{1/3}. \quad (44)$$

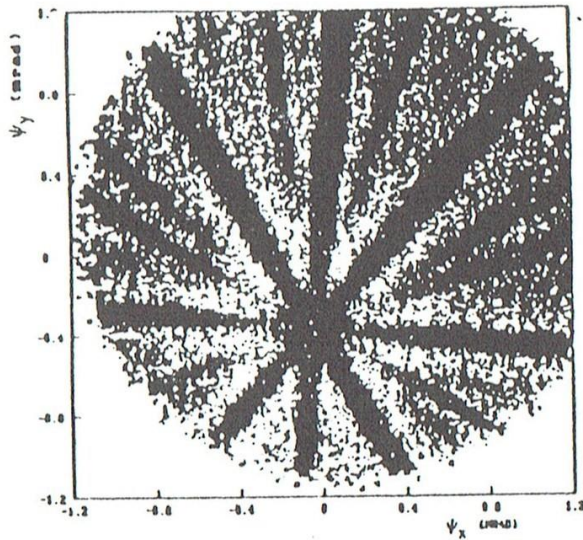


Fig. 11. Angular distribution of ~ 10 -GeV protons passed through a $\langle 110 \rangle$ oriented Ge crystal. The beam was nearly uniform over the region of angles of incidence within the large circle with ~ 2.5 -mrad diameter, and incidence directions of particles scattered by less than 0.1 mrad in the crystal have been marked with a black dot. The regions with little scattering appear black in the stereogram. The value of ψ_1 for the $\langle 110 \rangle$ axis is about 0.2 mrad. From [Bak *et al.* 1982].

As indicated in Fig. 10 and seen in Fig. 11, the stronger planes become narrower (weaker) close to the axis and the weaker planes disappear. However, at the same time, the stronger planes also play a role for $\psi < \psi_1$ where governing by strings of strings may lead to planar-type motion. For very small angles ψ , the concept of collisions with individual strings breaks down. The particle is confined to move in the centre of axial channels, and if the transverse energy $E\psi^2$ is lower than the barrier between neighbouring channels (see contour plot of U in Fig. 12), the motion is confined to one axial channel. This type of motion was denoted *proper channeling* by Lindhard (also called *hyper channeling*). The characteristic energy corresponding to the barrier between channels is seen in Fig. 12 to be lower than $E\psi_1^2$ by almost two orders of magnitude.

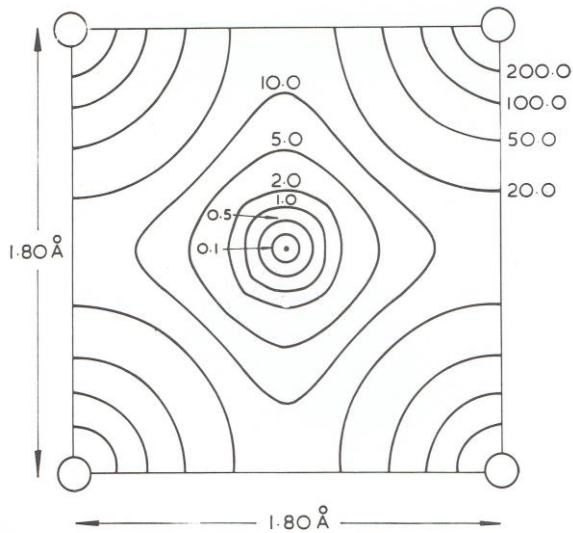


Fig. 12. Contour plot of the continuum axial potential for He on $\langle 100 \rangle$ Cu (fcc structure). The energies are in eV. The critical angle ψ_1 corresponds to a transverse energy of $E\psi_1^2 = 462$ eV. From [Gemmel 1974].

9. REVERSIBILITY AND BLOCKING

In the approximation, where ion trajectories are calculated as motion in an external, fixed potential, the motion is reversible. The exclusion of close encounters with atoms for incident, channeled particles corresponds to an exclusion of the time-reversed channeling trajectories for particles emitted from an atomic site. In the direction of an axis or plane, the emission is 'blocked' owing to correlated scattering by atoms on the string or plane, in which the emitted atom is sitting. The resulting dips in yield are identical to the channeling dips and, in fact, in some of the calculations shown earlier, blocking dips were evaluated (e.g., Fig. 9).

Through a simple argument, the equivalence may be related to Liouville's theorem for Hamiltonian motion. Consider a group of particles moving from a point A outside a crystal to a point B inside. According to Liouville's theorem, the volume in phase space filled by the particles is conserved through the trajectory, or

$$dp_x^A dp_y^A dp_z^A dx^A dy^A dz^A = dp_x^B dp_y^B dp_z^B dx^B dy^B dz^B. \quad (45)$$

At both A and B we choose the z -axis parallel to the trajectory. The potential at B is exceedingly small compared to the ion energy, and conservation of energy leads to the relations

$$\begin{aligned} v_A &= v_B = v \\ dz^A &= v dt = dz^B \\ dp_z^A &= \frac{dE}{v} = dp_z^B \end{aligned} \quad (46)$$

If we introduce the notations $dS = dx dy$ and $d\Omega = dp_x dp_y / p^2$, the relation in Eq. (45) then reduces to

$$d\Omega_A dS_A = d\Omega_B dS_B. \quad (47)$$

This is a relation familiar from optics. A spatial focussing of a beam is accompanied by an increase in the divergence (conservation of emittance). We should note that the formulation here is much simplified. Usually the phase-space volume can not be expressed as a product of volumes in momentum and real space at *both* A and B , as assumed in Eqs. (45) and (47). (Look at the simple example of free motion in one dimension. If position and velocity are uncorrelated at time $t = 0$, they become correlated at later times) However, the argument may be given a more stringent formulation.

From Eq. (47), we can demonstrate directly the equivalence of blocking and channeling:

1. *Channeling.* ν particles incident per unit area at angles ψ, φ . A process with cross section ΔS_B at B is observed. The yield is

$$Y_c(\psi, \varphi) = \nu \Delta S_A = \frac{dS_A}{dS_B} \nu \Delta S_B.$$

It is modified by the factor dS_A/dS_B relative to the ‘random’ yield $\nu \Delta S_B$.

2. *Blocking.* ν particles are emitted per unit solid angle at B . Particles are observed with a detector far away from the crystal, subtending a solid angle $\Delta \Omega_A$ around the direction specified by angles ψ, φ . The yield is

$$Y_b(\psi, \varphi) = \nu \Delta \Omega_B = \frac{d\Omega_B}{d\Omega_A} \nu \Delta \Omega_A .$$

It is modified by the factor $d\Omega_B/d\Omega_A$ relative to the random yield $\nu \Delta \Omega_A$. According to Eq. (47), the two factors are equal, i.e., if the yields are normalised to the random yield, we have

$$\chi_c(\psi, \varphi) \equiv \chi_b(\psi, \varphi). \quad (48)$$

This is a very useful result. Often calculations are much easier or more transparent in one case than in the other, and one may then freely chose the most convenient formulation. An example is the calculations of axial dips in the halfway-plane model which are much simpler to formulate as blocking calculations [Andersen 1967].

The reversibility of trajectories is confined to Hamiltonian motion (without magnetic fields). However, it may be shown that multiple-scattering processes in a sense are reversible too. This implies that the equivalence of channeling and blocking holds also in a description with an irreversible trend towards an equilibrium distribution in phase space. This is important since arguments based on Liouville's theorem have limitations which are well known from Gibb's coffee cup with cream! However, an important violation of reversibility is caused by slowing down. For large depths of penetration, where an appreciable fraction of the ion energy is lost, there will be significant deviations from equivalence of channeling and blocking.

We now give a more stringent proof of the reversibility relation in Eq. (48). In a channeling experiment, the normalised yield χ_c of close encounters is given by the ratio of fluxes at B with and without the presence of the crystal. The fluxes are proportional to the number of particles crossing a small area ΔS_B . At A these particles occupy a phasespace volume (four-dimensional) which is limited by the beam collimation $\Delta \Omega_A$ and by the condition that at B , the spatial coordinates fall within ΔS_B . Since in the random case, this volume is simply $\Delta \Omega_A \Delta S_B$, we obtain

$$\chi_c = (\Delta \Omega_A \Delta S_B)^{-1} \iint d\Omega_A dS_A \Big|_{\substack{\psi_A \in \Delta \Omega_A \\ \mathbf{r}_B \in \Delta S_B}}. \quad (48A)$$

The quantities $\Delta\Omega_A$ and ΔS_B can be chosen arbitrarily provided they are small enough for the flux to be constant over their extension, i.e., as long as the ratio in Eq. (48A) is independent of the value chosen.

For particle emission, we are interested in the ratio of angular fluxes outside the crystal with and without governing of trajectories. At B , the fluxes are proportional to the number of particles within a small solid angle $\delta\Omega_B$ and the particles are restricted to emerge from a small area δS_B . We therefore find for the normalised intensity of emitted particles in the blocking case

$$\chi_b = (\delta\Omega_A \delta S_B)^{-1} \iint d\Omega_B dS_B \left| \begin{array}{l} \boldsymbol{\psi}_A \in \delta\Omega_A \\ \mathbf{r}_B \in \delta S_B \end{array} \right. . \quad (48B)$$

Since we may make the special choice $\Delta\Omega_A = \delta\Omega_A$ and $\Delta S_B = \delta S_B$, we obtain from Eqs. (48A) and (48B), combined with Liouville's theorem, the reversibility relation in Eq. (48).

In this formulation, the problems with correlation of angular and spatial coordinates are avoided. In addition, it includes the possibility of ‘multiple paths’ connecting the phase-space volumes $\Delta\Omega_A \Delta S_A$ and $\Delta\Omega_B \Delta S_B$. This means that the area

$$\Delta S_A = \int dS_A \left| \begin{array}{l} \boldsymbol{\psi}_A \in \Delta\Omega_A \\ \mathbf{r}_B \in \Delta S_B \end{array} \right. \quad (48C)$$

and the solid angle

$$\Delta\Omega_B = \int d\Omega_B \left| \begin{array}{l} \boldsymbol{\psi}_A \in \Delta\Omega_A \\ \mathbf{r}_B \in \Delta S_B \end{array} \right. \quad (48D)$$

may consist of several small disconnected ‘islands’ which may be associated with macroscopically different paths. A simple example of this is discussed in Ch. 16. Outside the edge of the shadow behind an atom bombarded with positively charged particles, a point on a screen is hit by two trajectories, one with large impact parameter and small deflection and another with small impact parameter and large deflection.

10. EXPERIMENTAL OBSERVATIONS

There are a large number of different effects of channeling which can be observed in the experiments. We shall here indicate some of the most important ones. First, it is useful to introduce Lindhard's distinction between *primary and secondary* effects. Since channeling is due to the governing of projectile paths by correlated collisions, such correlated scattering is the primary phenomenon. A consequence of channeling is the restriction of the particle flux to the regions between strings or planes, and the resulting effects, e.g., reduced energy loss and enhanced ion range, are therefore secondary phenomena.

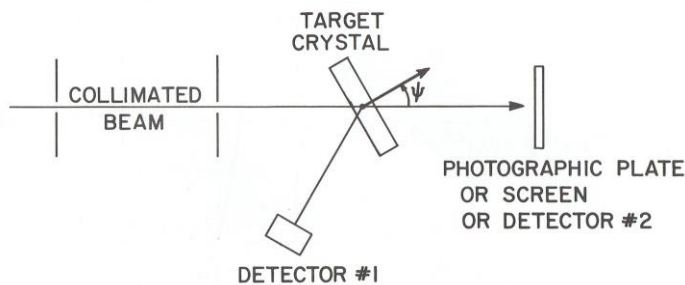
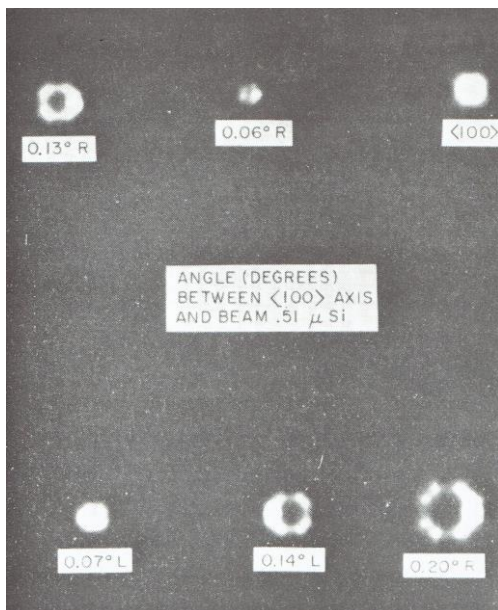


Fig. 13. Geometry for observation of transmission or close-encounter reactions.

When observing the interaction between a beam and a crystal, we have essentially two experimental possibilities, as illustrated in Fig. 13. We can observe the beam after transmission through a thin crystal, or we can observe some signal of a reaction between beam particles and crystal atoms – a nuclear reaction, x-ray excitation, or Rutherford backscattering, for example. The most direct evidence of the scattering by strings, with conservation of transverse energy, is perhaps the observation of the angular distribution of particles after transmission through a thin crystal. Examples of such distributions, measured with a photographic plate, are shown in Fig. 14. At an incidence angle of 0.20° to the $\langle 100 \rangle$ axis, for example, the intensity is seen to be confined to a ring centred on the axis direction, a so-called doughnut.



The ring results from azimuthal scattering around the axis and indicates conservation of transverse energy in collisions with strings. It is not continuously populated but contains dark "holes" which reflect the influence of planes, as illustrated in Fig. 10 (blocking by strings of strings).

Fig. 14. Doughnut patterns observed for 4-MeV protons transmitted through a $\langle 100 \rangle$ Si crystal, $0.5 \mu\text{m}$ thick. The particle intensities were measured on x-ray film 1.4 m downstream from the target. The incidence angles were all smaller than the critical angle which is about 0.35° . In each case, the $\langle 100 \rangle$ axis was tilted to the left (L) or right (R) of the beam direction by the angle indicated. From [Armstrong *et al.* 1971].

The normal 'random' multiple scattering is reduced for channeled particles, as was illustrated in Fig. 11. However, the doughnut scattering is very strong and may lead to a much faster increase in the mean-square deflection angle than normal multiple scattering. There is an interesting analogy to the relative contribution of electrons and nuclei to the normal multiple scattering. There are Z_2 times as many electrons but since the scattering angle in a Coulomb deflection is proportional to the charge of the scattering centre, and the deflection angles add in quadrature, the contribution

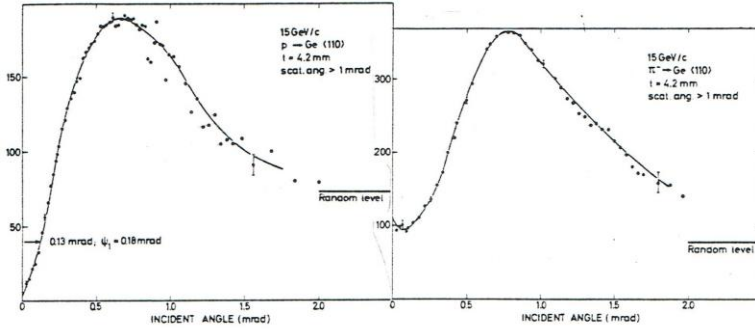


Fig. 15. For a uniform distribution of incidence directions, like in Fig. 11, the number of particles scattered by more than 1 mrad is plotted against the angle to a $\langle 100 \rangle$ axis for 15 GeV/c protons and π^- transmitted through a 4.2-mm thick Ge crystal. From [Uggerhøj 1983].

from 'nuclear' collisions to the mean-square scattering angle will be Z_2 times larger than the electronic contribution. Similarly, the correlated scattering by n atoms on a string will give a contribution to the mean-square scattering angle which is n times larger than obtained from n uncorrelated deflections at the same impact parameter. For incidence angles $\psi \geq \psi_1$, where there is no restriction on impact parameter from channeling, the correlation will therefore lead to enhanced scattering. The enhancement is very dramatic at high energies (e.g. GeV protons) where the angle ψ_1 is very small and the number n therefore very large. Experimental observations of the effect are shown in Fig. 15.

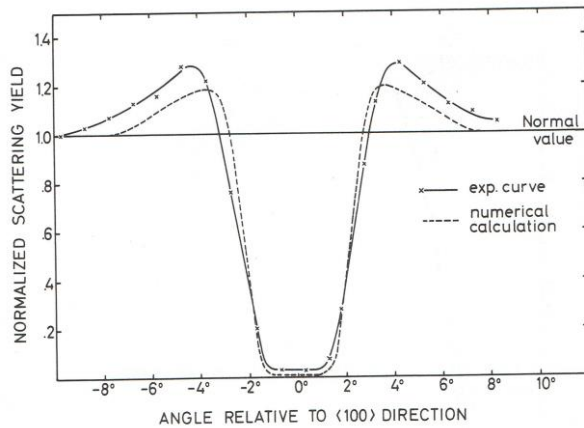


Fig. 16. Dip in backscattering yield for 480-keV protons along a $\langle 100 \rangle$ direction in W. The calculation is based on the half-way plane model with the standard potential. From [Andersen 1967].

However, the most important – and dramatic – manifestation of channeling is the almost complete extinction of nuclear reactions and Rutherford backscattering for incidence parallel to a strong crystal axis [Bøgh and Uggerhøj 1965], as shown in Fig. 16. It is compared with a numerical calculation based on the halfway-plane

model (Fig. 7). The geometry for such a measurement is illustrated in Fig. 17. The crystal is mounted on a goniometer, which allows rotations around two perpendicular axes: a 'tilt' around the vertical axis and an 'azimuthal rotation' around an axis perpendicular to the crystal.

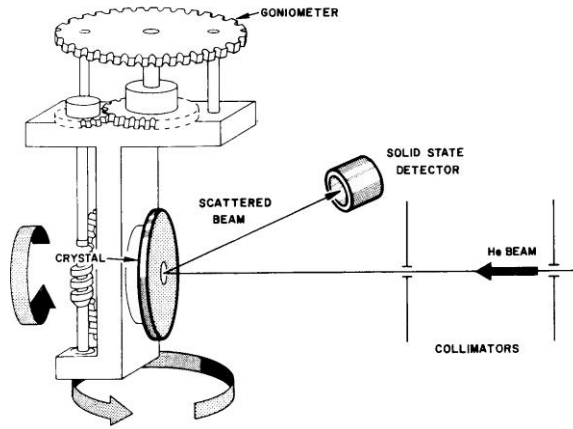


Fig. 17. Schematic view of an experimental setup for channeling experiments. The ion beam impinges on a crystal mounted in an alignment apparatus, a goniometer. The solid-state detector records the energy distribution and intensity of the backscattered ions, typically at 135° to the beam direction. From [Feldman *et al.* 1982].

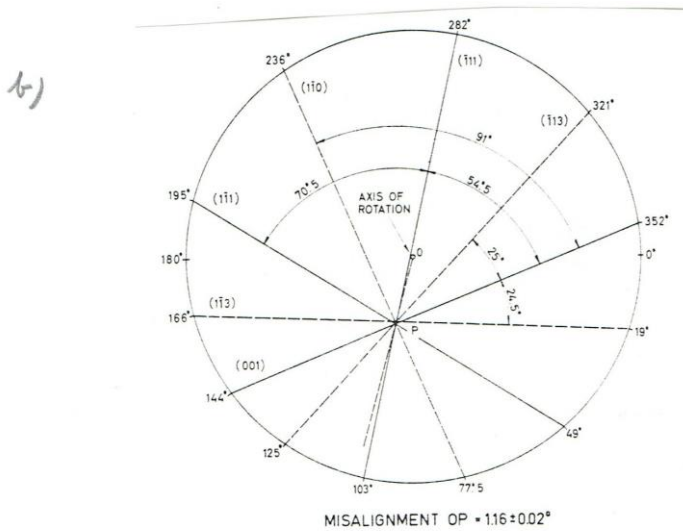
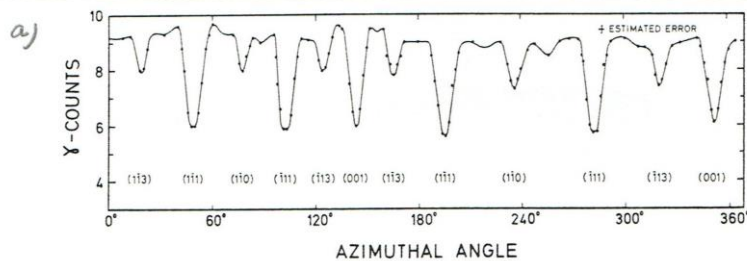


Fig. 18. (a) Azimuthal scan around a $\langle 110 \rangle$ axis at a tilt angle of 3.8° . The γ yield from (p, γ) resonances is recorded for 510 keV protons incident on an Al crystal. (b) Stereogram constructed from (a). The $[110]$ axis is at the intersection of the planes. From [Andersen *et al.* 1965].



A scan like that shown in Fig. 16 used to be made by varying the 'tilt angle' only after a determination of the value for the azimuthal angle for which the tilt 'goes through the axis'. The method applied for this determination is illustrated in Fig. 18. For a fixed tilt angle, the variation in yield is measured for a 360° rotation in the azimuthal angle. The dips in yield shown in the lower part of the figure indicate orientations where the beam is parallel to a strong plane. When the angles are marked around a circle in a stereogram, as shown in the upper part, the planes can be drawn by connecting the marks in pairs in such a way that the lines pass through a common point P which indicates the position of the axis. The dashed line through P and the axis of rotation O gives the azimuthal angle for which a tilt scan will make the beam parallel to the axis at some tilt angle.

Today goniometers are usually under computer control, and more complicated procedures are possible. It turns out to be an important improvement to make an axial scan by averaging the yield over circles in the stereogram centred on the axis (P) with varying radius ψ . Thereby planar effects average out to a large extent, and one is left with a 'pure' string effect which can be compared quantitatively to the calculations we shall discuss in the following chapters.

For most purposes, backscattering is the most useful 'close-encounter process' to observe, although all processes requiring a collision with an atomic nucleus at an impact parameter, which is small compared to the vibrational amplitude, ρ , in principle give equivalent dips in yield.

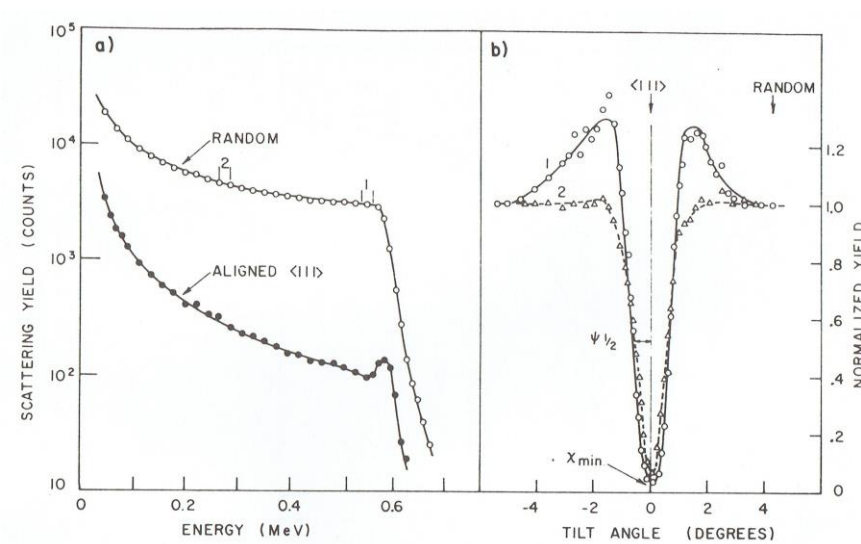


Fig. 19. (a) Energy spectra of 1-MeV He ions backscattered at 160 deg. from a Si crystal, for incidence parallel to a <111> direction (aligned) and off-axis (random). (b) Counts, normalised to random, in the energy intervals 1 and 2 in (a), as a function of the angle of incidence relative to a <111> axis. From [Picraux *et al.* 1969].

There are several reasons for this. First, Rutherford scattering is a universal process with a well-defined (and large) cross section. Second, the energy distribution of the backscattered particles gives information on the dependence on penetration depth into the crystal. This is illustrated in Fig. 19. To the left are energy spectra of 1-MeV He ions backscattered (160°) from a Si crystal. The maximum energy corresponds to

scattering from the surface and is reduced only by the elastic energy loss in the single collision. Lower energies correspond to scattering deeper into the crystal, and the energy-depth conversion can be calculated from the known stopping power (E loss equal stopping on the way into the crystal + elastic loss + stopping on the way out). By accumulating the yield within a small energy window, one can measure the dip in yield at different depths, as illustrated on the right.

One notices a small hump in the aligned energy spectrum at the surface (note log scale!). This corresponds to scattering from the surface where the flux of incident particles is still uniform, and the yield is the same as in the 'random' case. It appears to be lower because of the finite energy resolution of the detector (typically ~ 30 keV for ~ 1 -MeV He in a solid-state detector). A better resolution can be obtained by momentum analysis in a magnetic spectrometer, as illustrated in Fig. 20. The effective isolation of a signal from backscattering at the surface for incidence in a channeling direction can be used to study surface structures with ion beams [Feldman *et al.* 1982].

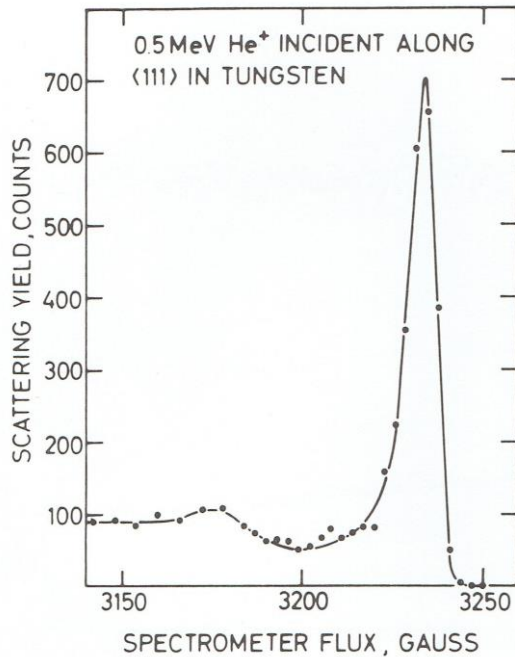


Fig. 20. 'Surface peak' measured with magnetic spectrometer. The x -axis is essentially an energy axis for backscattered He ions, and the peak stems from scattering off the surface layer(s). From [Bøgh 1972].

Blocking dips in backscattering yield can be observed in a setup similar to the one shown in Fig. 17. It requires a narrow collimator in front of the detector, which must be movable. The equivalence of blocking with channeling is demonstrated in Fig. 21. One curve gives the scattering yield as a function of the angle of the beam to the axis, with the detector looking in a random direction; the other curve corresponds to a variation of the angle of the detection direction to the axis, for fixed 'random' incidence direction of the beam. The window in the energy spectrum was placed close to the maximum energy, like window 1 in Fig. 19, in order to minimize effects of energy loss with depth (not reversible).

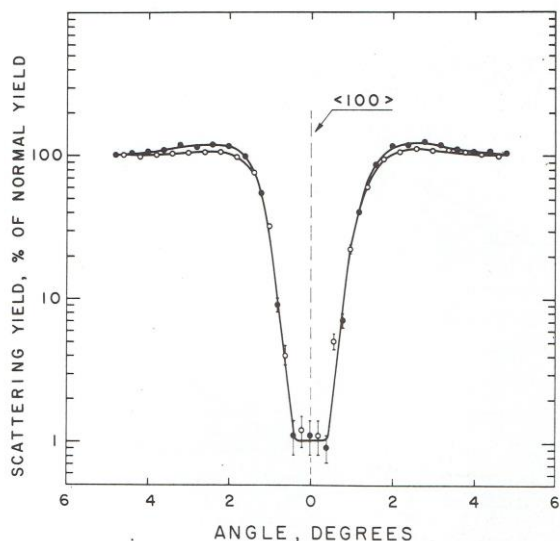


Fig. 21. Comparison of channeling and blocking dips for 1-MeV protons backscattered through 135° in a W crystal at a depth of $3000 \pm 500 \text{ \AA}$. From [Bøgh and Whitton 1967].

In a blocking measurement, the yield can be recorded simultaneously over a large angular region with a position-sensitive detector. The simplest detector is a plastic film which, after etching, will show positions of ion impact as small craters in the surface. A resulting 'blocking pattern' is shown in Fig. 21a. This type of measurement can, for example be used to determine quickly the orientation of a crystal.

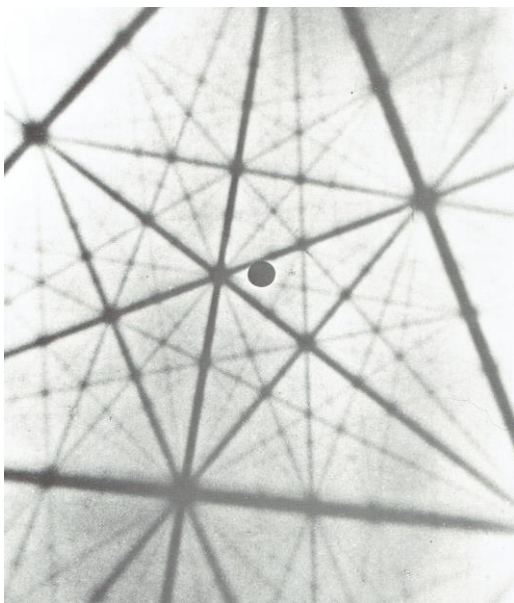


Fig. 21a. Backscattering blocking pattern for 150-keV protons on a Bi crystal near a $\langle 111 \rangle$ direction. The black circle near the centre is the hole allowing the beam to pass through the film. From [Engelmohr *et al.* 1970].

11. STATISTICAL TREATMENT

For planar channeling, the trajectories are very simple, oscillating back and forth between a pair of neighbouring planes. For axial channeling, the motion is much more complicated. However, the very complexity may be turned into an advantage. The trajectories may become ergodic and fill out the available phase space.

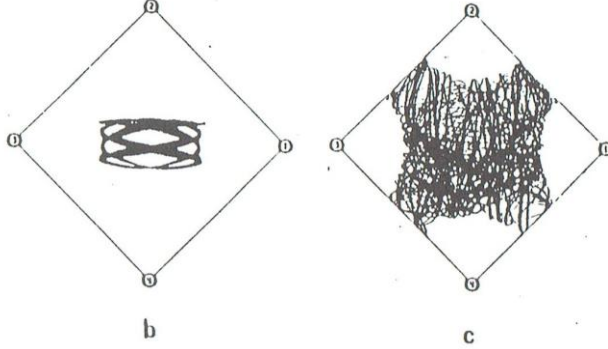


Fig. 22. Projection on the transverse plane of computer-simulated trajectories of channelled ions, with a very low transverse energy (b), where the ions are confined to one transverse unit cell (proper channeling), and with a somewhat higher E_{\perp} (c), where they can move freely about between strings. In the latter case, the trajectory segments in different unit cells have been translated back by symmetry.

The spatial distribution is illustrated in Fig. 22, for two transverse energies. One is lower than the barrier between channels (see Fig. 12), and the motion is confined to one channel (proper channeling). The motion is then too simple to be ergodic. It is quasi periodic.

For the higher transverse energy, the particle can move freely about between strings. The trajectory segments in different unit cells have been translated into one cell in the display, and they are seen to fill out the available area, with $E_{\perp} > U(\mathbf{r})$, nearly uniformly. To obtain the probability density, one would have to weight the density of trajectories by the reciprocal transverse velocity, but for the qualitative impression of ergodicity, this is not so important. We shall later study more quantitatively the trend towards a uniform distribution in phase space. According to Liouville's theorem, such a distribution is stable. It corresponds to a *statistical equilibrium*.

We can represent the distribution by a microcanonical ensemble,

$$P_0(\mathbf{r}, \mathbf{p}_{\perp}) = \begin{cases} K & \text{for } E_{\perp}^0 < E_{\perp} < E_{\perp}^0 + \Delta E_{\perp} \\ 0 & \text{elsewhere} \end{cases}, \quad (49)$$

where $E_{\perp} = p_{\perp}^2/2M_1 + U(\mathbf{r})$. A more convenient mathematical representation is a δ -function,

$$P_0(\mathbf{r}, \mathbf{p}_{\perp}) \propto \delta(E_{\perp} - p_{\perp}^2/2M_1 - U(\mathbf{r})). \quad (50)$$

Let us use this expression to calculate the spatial-density in equilibrium,

$$\begin{aligned} P_0(\mathbf{r}) &\propto \int d^2\mathbf{p}_{\perp} \delta(E_{\perp} - p_{\perp}^2/2M_1 - U(\mathbf{r})) \\ &\propto \int d(p_{\perp}^2/2M_1) \delta(E_{\perp} - p_{\perp}^2/2M_1 - U(\mathbf{r})). \end{aligned} \quad (51)$$

The δ -function can only be fulfilled within the integration interval if $E_{\perp} - U(\mathbf{r}) > 0$. Introducing a proper normalisation, we then obtain

$$P_0(\mathbf{r}) = \begin{cases} \frac{1}{A(E_{\perp})} & E_{\perp} > U(\mathbf{r}) \\ 0 & E_{\perp} < U(\mathbf{r}) \end{cases} \quad (52)$$

where $A(E_{\perp})$ is the allowed area in the transverse unit cell with total area A_0 .

This is a remarkably simple distribution. As seen from Eq. (51), the simplicity belongs to two dimensions where, for fixed \bar{r} , the differential volume in momentum space is proportional to dE_{\perp} . In one dimension, the planar case, $dp_x \propto dE_{\perp}/p_x$, and the density $P_0(x)$ is inversely proportional to transverse velocity. This result may of course also be argued directly. The probability density at x is proportional to the time spent at that distance from the plane, i.e., inversely proportional to v_x . For fixed E_{\perp} , the distribution $P_0(x)$ hence has a minimum at the centre of the planar channel and diverges at the turning points near the planes.

Qualitative insight into the statistical equilibrium in one, two, and three dimensions may be gained from an explicit calculation of the distribution in height of the water in a fountain. If the water is ejected vertically only, one gets an accumulation of water at the top. If the water is ejected isotropically in two dimensions, the range of ejection angles contributing to the density increases with decreasing height, and this exactly compensates for the water accumulation near the top for a single ejection angle. Finally, for isotropic ejection in three dimensions, the increase in the number of water beams contributing at decreasing height dominates, and one obtains a density distribution proportional to water velocity.

Averages in statistical equilibrium. Usually, the probability for occurrence of the process under consideration, e.g., backscattering, depends only on the position of the trajectory in the transverse plane, i.e., it is proportional to a function $W(\mathbf{r})$, normalized over the transverse area A_0 . In statistical equilibrium, the yield is then determined by the integral,

$$\langle W(\mathbf{r}) \rangle = \frac{A_0}{A(E_{\perp})} \int_{A(E_{\perp})} W(\mathbf{r}) d^2\mathbf{r} . \quad (53)$$

'Random' yield is unity per definition. It corresponds to uniform flux over A_0 and is obtained from Eq. (53) for $E_{\perp} \rightarrow \infty$,

$$\langle W(\mathbf{r}) \rangle_{\text{rand}} = \int_{A_0} W(\mathbf{r}) d^2\mathbf{r} = 1 . \quad (54)$$

The most important example is the yield of processes which require a close collision with a nucleus, i.e., an impact parameter $q \ll \rho$. The probability density $W(\mathbf{r})$ is then given by the Gaussian distribution (17a) of atomic displacements. Examples of

such processes are Rutherford backscattering, nuclear reactions, and inner-shell ionisation. For outer shells, the ionisation can take place in collisions with impact parameter $q \geq \rho$, and the displacement distribution must be convoluted with the impact-parameter dependence of the ionisation probability [Andersen and Davies 1976].

The yield of close-encounter processes, normalised to random yield, is given by

$$\Pi_{\text{in}}(E_{\perp}) = \frac{A_0}{A(E_{\perp})} \int_{r>r_m} \exp\left(\frac{-r^2}{\rho^2}\right) d\left(\frac{r^2}{\rho^2}\right) \cong \exp\left(\frac{-r_m^2}{\rho^2}\right), \quad (55)$$

where r_m is the minimum distance of approach, $E_{\perp} = U(r_m)$. The yield drops to zero very quickly when E_{\perp} becomes less than $\sim U(\rho)$. The half width of the dip in yield is determined by the condition $\exp\left(-\frac{r_m^2}{\rho^2}\right) = 1/2$, or $r_m^2 = \rho^2 \log 2$. If we introduce the standard potential, we obtain the formula

$$\psi_{1/2} = \psi_1 \left[\frac{1}{2} \log \left(\frac{(Ca)^2}{\rho^2 \log 2} + 1 \right) \right]^{1/2}. \quad (56)$$

This is the more precise result, replacing the limit in Eq. (33), argued qualitatively. With typical values of the parameters, e.g., $C = \sqrt{3}$, $a = 0.17 \text{ \AA}$, $\rho = 0.11 \text{ \AA}$ for He in Si at room temperature, the factor on ψ_1 is close to unity, *in casu* $\psi_{1/2} = 1.1 \psi_1$.

As our second example, we consider the yield of processes requiring a hard collision with an electron. Examples are positron annihilation in flight, δ -electron ejection, and the contribution to stopping from close collisions.

If we take the crystal potential to be the electrostatic potential seen by a test charge, it is connected to the electron density by Poisson's equation. If we average in the z -direction on both sides of this equation, we obtain a connection between the continuum potential $U(\mathbf{r})$ and the z -averaged electron density $\rho_s(\mathbf{r})$,

$$\Delta U(\mathbf{r}) = 4\pi(Z_1 e^2)\rho_s(\mathbf{r}). \quad (57)$$

In two dimensions, the Laplace operator in cylinder coordinates is given by

$$\Delta = \frac{1}{r} \frac{\partial}{\partial r} r \frac{\partial}{\partial r} + \text{angular part}. \quad (58)$$

In the important region of the average (53) of $\rho_s(\mathbf{r})$ there is cylindrical symmetry around a string. We therefore approximate the unit cell by a circle with area $\pi r_0^2 = A_0$ and obtain for the average of ΔU ,

$$\begin{aligned}\langle \Delta U(r) \rangle &= \frac{1}{A(E)} \int_{r_m}^{r_0} \pi d(r^2) \frac{1}{r} \frac{d}{dr} r \frac{d}{dr} U(r) \cong \frac{2\pi}{\pi r_0^2} \int_{r_m}^{r_0} dr \frac{d}{dr} \left(r \frac{d}{dr} U(r) \right) \cong \\ &\cong \frac{2\pi}{\pi r_0^2} (-r_m U'(r_m))\end{aligned}\quad (59)$$

We apply the standard potential again,

$$U'(r) = -\frac{Z_1 Z_2 e^2}{d} \frac{2(Ca)^2}{r} \frac{1}{(Ca)^2 + r^2}, \quad (60)$$

with the limit

$$rU'(r) \rightarrow -\frac{2Z_1 Z_2 e^2}{d} \quad \text{for } r \rightarrow 0. \quad (61)$$

The random case corresponds to $E_\perp \rightarrow \infty$ and $r_m \rightarrow 0$ and we then obtain from Eqs. (57) and (59),

$$\langle \rho_s(r) \rangle_{\text{rand}} = NZ_2, \quad (62)$$

since $\pi r_0^2 = (Nd)^{-1}$ where N is the atomic density in the crystal. This we knew beforehand, of course, but it is nice to see it come out!

It is natural to express the average of ρ_s for finite E_\perp in terms of a reduced number of electrons per atom, $Z_2^*(E_\perp)$, and Eqs. (57), (59) lead to

$$\frac{Z_2^*(E_\perp)}{Z_2} = \frac{-dr_m U'(r_m)}{2Z_1 Z_2 e^2} = \frac{1}{1 + \frac{r_m^2}{(Ca)^2}} = 1 - \exp\left(-\frac{2E_\perp}{E\psi_1^2}\right). \quad (63)$$

Again a very simple result is obtained with the standard potential. The width of the dip in yield of scattering by electrons is considerably narrower than the dip in yield of close encounters with nuclei. If again we express the transverse energy at half dip, $Z_2^* = Z_2/2$, as $E_\perp = E\psi_{1/2}^2$ we obtain

$$\psi_{1/2} = \psi_1 (1/2 \log 2)^{1/2} \cong 0.6\psi_1. \quad (64)$$

The reason for the narrower dip is that the atomic electrons have a much wider distribution around the string than do the atomic nuclei and Eq. (64) corresponds to the relation $E\psi_{1/2}^2 = U(Ca)$ which would have been our first guess from qualitative considerations.

12. TREND TOWARDS EQUILIBRIUM

Consider a beam of particles with initially well-defined and not too low transverse momentum \mathbf{p}_0 . Although the length of \mathbf{p}_\perp is the same before and after a collision with a string, the direction of it is changed. Gradually, any memory of the initial direction is lost, and equilibrium is attained. In a transmission experiment, as illustrated in Fig. 14, the doughnut becomes uniformly populated.

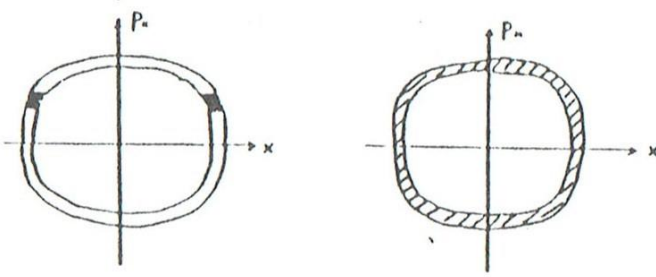


Fig. 23. Two-dimensional planar phase space. Initial distribution and average over one period of the motion.

In the doughnut pattern, one could clearly see the influence of planes or strings of strings but at first we disregard this complication and consider a model with randomly distributed strings. For symmetry reasons, the average transverse momentum $\langle \mathbf{p}_\perp \rangle$ of the particles in the beam will then be parallel to \mathbf{p}_0 , $\langle \mathbf{p}_\perp \rangle = \langle \cos \alpha \rangle \mathbf{p}_0$, where α is the angle between \mathbf{p}_\perp and \mathbf{p}_0 . Since all impact parameters l with strings are equally probable, it is easily seen that in collisions with impact parameters $\pm l$, the projection on the initial direction is changed on the average by the amount $-(1 - \cos \varphi) \langle \mathbf{p}_\perp \rangle$, where $\varphi(l)$ is the scattering angle in the transverse plane. The average momentum therefore decreases exponentially with depth,

$$\langle \mathbf{p}_\perp \rangle = \mathbf{p}_0 \exp\left(-\frac{z}{\lambda_\perp}\right), \quad (65)$$

where the mean-free path λ_\perp is given by

$$\frac{1}{\lambda_\perp} = N d \psi \int_{-\infty}^{\infty} dl (1 - \cos \varphi(l)) . \quad (66)$$

Here it is assumed that the particles move with nearly constant transverse velocity v_\perp , which is well fulfilled if the transverse energy is not too low, $E_\perp \sim E \psi_1^2$. A reasonably high E_\perp is required anyway for the picture of independent collisions with strings to be applicable.

The integral receives its main contributions from small impact parameters, and we may therefore in a cursory estimate use the simple potential $U(r) \sim E \psi_1^2 (a/2r)$ (cf. Eq. (23a)). The scattering law is then Rutherford's, $\tan(\varphi/2) = r_m/2l$, where $E_\perp = U(r_m)$, and using the relation

$$1 - \cos \varphi = 2 \left(1 + \left(\cot \frac{\varphi}{2}\right)^2\right)^{-1/2},$$

the integration is straightforward,

$$\lambda_{\perp} = (\pi N d a)^{-1} \frac{\psi}{\psi_1^2} . \quad (67)$$

For $\psi \sim \psi_1 \sim 1^\circ$, λ_{\perp} is of order 1000 Å. This simple estimate indicates that if we look apart from the arrangement of strings into planes any memory of the initial transverse direction is lost very quickly.

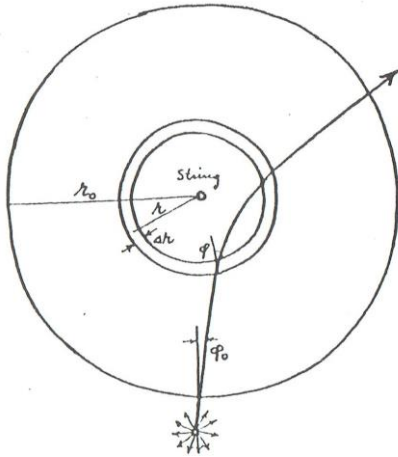


Fig. 24. Scattering on strings of particles with an isotropic distribution in transverse momentum far from strings.

However, the presence of planar structure may be a serious complication. If the beam is initially parallel to a plane, governing by strings of strings will lead to a planar-type oscillatory motion between two planes, and the transverse momentum remains more or less in the initial direction. On the other hand, when the beam is initially not parallel to a plane, the blocking by strings of strings hinders scattering into planar directions (cf. Fig. 14). Often the direction of \mathbf{p}_{\perp} is not of much importance but, as we shall see, there is a coupling between the direction of \mathbf{p}_{\perp} and the distribution in space which is decisive for the yield of reactions.

Equilibrium in space

Consider first the planar case. A group of particles initially within an interval $dx dp_x$ in transverse phase space sweeps through all the available phase space during one period of the motion. The equilibrium distribution therefore corresponds to an average over one period of the motion.

For the two-dimensional axial case, an energy surface in phase space is three-dimensional, and the situation is more complicated. Trajectories can be quasiperiodic or quasi-ergodic, as illustrated in Fig. 22 in spatial projection. Usually, restriction of the motion to part of phase space is a consequence of a conservation law. If, for example, the potential has axial symmetry near the minimum, angular momentum is conserved for proper channeling.

Another example is the approximate conservation of transverse energy in planar-type motion for particles with higher transverse energy, when the transverse

velocity is nearly parallel to a plane. We shall later (Ch. 15) consider the influence on the spatial distribution of this division of phase space into channeling- and blocking-type transverse trajectories. Here we show how an isotropic distribution of transverse momenta far from strings ensures a spatial equilibrium distribution in the transverse plane.

Consider a stream of particles incident on a string with not too low transverse energy, $E_{\perp} = p_0^2/2M_1$, and with an isotropic distribution of transverse momenta (see Fig. 24). An area $\pi r_0^2 = (Nd)^{-1}$ is ascribed to the string, and a trajectory may be specified through its initial angle φ_0 with the direction toward the string.

We now want to calculate the number $\Delta N(r)$ within a circular ring of radius r and thickness Δr and compare with the result (52) obtained from statistical equilibrium. Since the potential is axially symmetric near the string, there is approximate conservation of angular momentum during the collision,

$$p_{\perp} r \sin \varphi = p_{\perp}^0 r_0 \sin \varphi_0. \quad (68)$$

The time Δt spent within the ring is given by

$$\Delta t = \frac{2\Delta r}{\cos \varphi} \frac{M_1}{p_{\perp}}. \quad (69)$$

When the velocity distribution of the particles incident on the string is isotropic, the number of particles crossing the boundary at angles $(\varphi_0, \varphi_0 + d\varphi_0)$ is proportional to $\cos \varphi_0 d\varphi_0$, and we obtain for $\Delta N(r)$

$$\Delta N(r) \propto \int_{|\varphi| < \pi/2} d\varphi_0 \cos \varphi_0 \frac{2\Delta r}{\cos \varphi} \frac{M_1}{p_{\perp}}. \quad (70)$$

After elimination of φ_0 through Eq. (68) we find

$$\Delta N(r) \propto 2\pi r \Delta r \frac{M_1}{p_{\perp}^0 r_0}. \quad (71)$$

The number of particles is proportional to the area of the ring, and this corresponds to equilibrium in two dimensions. Thus we have seen that isotropy of the momentum distribution far from strings ensures that the spatial distribution around the strings corresponds to equilibrium if it is averaged over a time (depth) longer than that spent in a collision with one string. The example is a special case of the general situation of an imposed external equilibrium in phase space. It may to some extent be realised in experiments if one performs an average over azimuthal angles in an axial scan (see Ch.15).

13. THREE STAGES IN PARTICLE MOTION

If we want to calculate the yield of some process as a function of incidence angle to an axis or a plane, it is useful to divide the particle motion into three stages:

1. Transmission through the crystal surface,
2. Penetration to the reaction depth z ,
3. Occurrence of the reaction.

Two different statistical pictures are useful. In stage 3, the reaction yield depends on the total flux distribution of the beam relative to the strings or planes. It would therefore appear natural to follow the development of the total flux through the three stages, and indeed, this is intuitively the simplest picture. However, in stage 2, conservation of transverse energy is the dominant feature, and hence it is convenient to divide the particles into groups with well-defined E_{\perp} . This approach is particularly useful where multiple scattering is included. The effect of thermal fluctuations in deflections by atoms and of electronic collisions may be described as a - fairly slow - diffusion in transverse energy.

1. Surface transmission

At the surface, the incident particles hit the ends of atomic strings. For zero incidence angle to an axis, the initially uniform particle flux is pushed away from the strings and gradually concentrated in the region in between, as illustrated in Fig. 25.

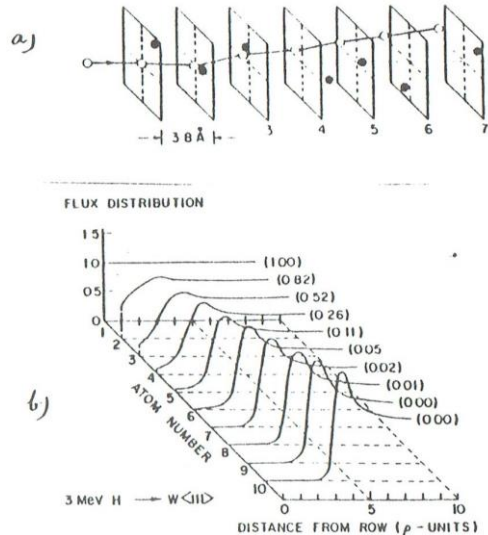


Fig. 25. Computer simulation of surface transmission of 3-MeV H along a $\langle 111 \rangle$ direction in W. In (a), the equilibrium positions of the atoms in a row or string are at the centre of the planes. The filled circles indicate atomic positions in the consecutive atomic planes, and the open circles are consecutive positions of an incident particle. The depth axis has been contracted for the display. The development of the flux distribution is shown in (b). The normalised backscattering yield from the different layers is given in parentheses. From [Feldman *et al.* 1982].

The yield of close encounters therefore falls from the random value at the surface to zero just inside, until at depths $z \sim d_s/\psi_1$, where d_s is the distance between strings, the deflected particles collide with neighbouring strings. This behaviour is reflected in the surface peak in yield, illustrated in Fig. 20. The number of surface layers exposed to the nearly uniform flux depends on the projectile energy and also on the magnitude of the vibrational amplitude ρ . At low energies and low temperature, only

one layer is exposed, but with increasing energy, the deflections become smaller, and many layers contribute to the surface peak. The decisive quantity is again $\rho/d\psi_1$, and in studies of surface structure, one must keep this quantity small to isolate the signal from the top layer [Feldman *et al.* 1982]. While scaling properties of the surface peak can be understood from analytical models, Monte-Carlo calculations are most useful for quantitative estimates. Only relatively few deflections are involved for each particle, and hence such calculations are efficient. If we denote the distribution of the flux (relative to random) at the n 'th atom on a string by $f_n(r)$ and the displacement distribution of the atom by $P_n(r)$, the effective number of atoms contributing to the surface peak is given by

$$N_s = \sum_n \int_0^{r_0} f_n(r) P_n(r) 2\pi r dr \quad (72)$$

with the usual normalisation of the displacement distribution over the area πr_0^2 (see Fig. 26). P_n and P_m are here assumed independent for $n \neq m$ but there can be significant correlation of vibrations of neighbouring atoms (Ch. 7).

To find the distribution in transverse energy behind the surface, we apply the continuum (or half-way-plane) picture. Then $E_\perp = E\varphi^2 + U(r)$ is conserved in the first collision with a string and may be evaluated at the surface plane (or, for that matter, at a distance $d/2$ in front of the surface). For particles incident at angle ψ to an axis, the distribution $g(E_\perp)$ in transverse energy is then obtained from the relation

$$g(E_\perp) dE_\perp = dA(E_\perp - E\psi^2), \quad (73)$$

leading to

$$g(E_\perp) = \frac{A'(E_\perp - E\psi^2)}{A_0}. \quad (74)$$



Fig. 26. Transverse plane with unit cell A_0 and the approximation of a circular unit cell with the same area.

In this description, surface transmission is not a process but a change of variable. A convenient way to perform such a change is to integrate the distribution over the old variables, here \mathbf{r} , weighted by a δ -function expressing the new variable, here E_\perp , in terms of the old ones,

$$g(E_\perp) = \frac{1}{A_0} \int_{A_0} d^2\mathbf{r} \delta(E_\perp - E\psi^2 - U(\mathbf{r})). \quad (74A)$$

To see that this expression is identical to Eq. (74), we introduce the area function $A(E_\perp)$ and its inverse $U(A)$,

$$g(E_\perp) = \frac{1}{A_0} \int_0^{A_0} dA \delta(E_\perp - E\psi^2 - U(A)).$$

Equation (74) then follows from the standard integral, $\int \delta(f(x))dx = |f'(x)|^{-1}|_{f(x)=0}$, where $f(x)$ is assumed to be monotonic. We just insert the relation $U'(A) = A'(U)^{-1}$. If the incident beam is not sharply collimated, or is scattered in an amorphous surface layer, we may describe the angular distribution by a normalised distribution $f(E\psi^2)$, and the expression above is then generalised to

$$g(E_\perp) = \int_0 f(E\psi^2)d(E\psi^2) \frac{1}{A_0} \int_{A_0} d^2\bar{r} \delta(E_\perp - E\psi^2 - U(\mathbf{r})). \quad (74B)$$

For particles described by a distribution $g(E_\perp)$, passing out through a surface, the surface transmission is a transformation to a distribution in $E\psi^2$ outside the crystal,

$$f(E\psi^2) = \int dE_\perp g(E_\perp) A(E_\perp)^{-1} \int_{A(E_\perp)} d^2\bar{r} \delta(E_\perp - E\psi^2 - U(\mathbf{r})), \quad (74C)$$

where we have assumed statistical equilibrium for fixed E_\perp .

When the potential is flat, the derivative of the area function is large, and hence the distribution in Eq. (74) has a maximum at $E_\perp = E\psi^2 + U_{\min}$ and a tail up to $E_\perp = E\psi^2 + U_{\max}$. (The thermally averaged potential has a finite maximum. We have omitted the index T for simplicity of notation.) A large deflection by one of the string atoms can of course lead to a larger value of E_\perp than this maximum. This correction to the continuum-model surface transmission is important for the close-encounter yield at $\psi = 0$, where only particles in the high- E_\perp tail of the distribution $g(E_\perp)$ contribute ('Barrett correction' to minimum yield, see Ch. 15).

For planes, analogous considerations apply. The distribution in transverse energy is determined by

$$g(E_\perp)dE_\perp = 2dx/d_p, \quad (75)$$

leading to

$$g(E_\perp) = L'(E_\perp)/d_p, \quad (76)$$

where $L(E_\perp) = d_p - 2x_m$ is the allowed one-dimensional space between planes.

2. Transmission through crystal

In the second stage, there is approximate conservation of E_\perp , and the flux development is characterised by a trend towards equilibrium. As we have seen, the equilibrium distribution (52) is obtained if the momentum distribution becomes isotropic. Again the situation for $\psi = 0$ is special because the initial distribution ($z =$

0) of particles with $E_{\perp} \geq E\psi_1^2$ is very far from equilibrium. The particles are all located close to the strings and have zero transverse momentum. We later discuss the restricted equilibrium approached in this case (Sec. 15). Here we note that the

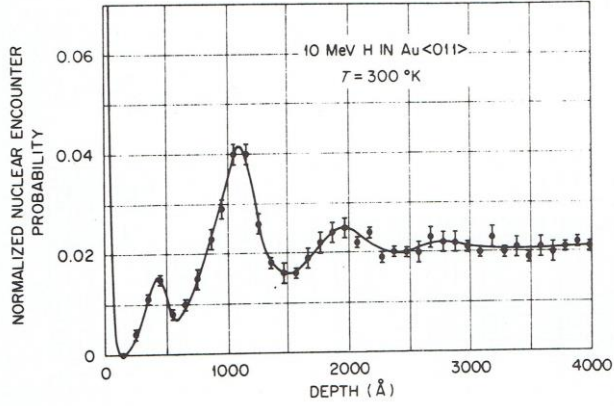


Fig. 27. Monte-Carlo simulation of backscattering yield from 10-MeV H incident along a $\langle 110 \rangle$ axis in Au. From [Barrett 1971].

close-encounter yield for $\psi = 0$ shows pronounced oscillations just behind the surface, as illustrated in Figs. 27 and 28 for the axial and planar cases, respectively. The maxima correspond to depths where particles deflected through an angle close to the critical angle by one string, or plane have moved across to neighbouring strings or have gone through an integral number of half periods of planar oscillations,

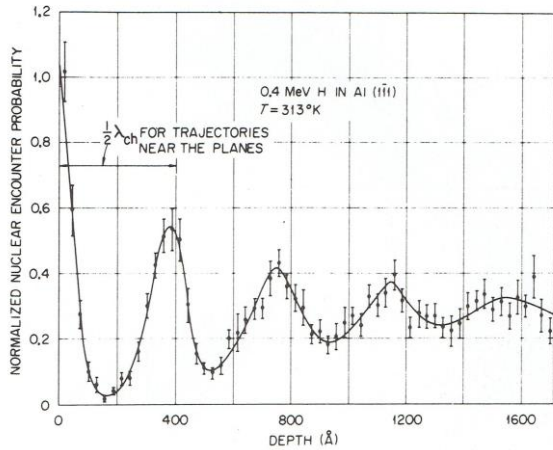


Fig. 28. Monte-Carlo simulation of backscattering yield from 0.4-MeV H incident parallel to a $\{111\}$ plane in Al. From [Barrett 1971].

respectively. After a few oscillations, the yield approaches a constant value, corresponding to some equilibrium flux distribution. Over much larger depths, however, the yield changes due to ‘dechanneling’ caused by thermal and electronic multiple scattering. We shall later discuss briefly how the change in distribution over transverse energies,

$$g(E_{\perp}, z = 0) \rightarrow g(E_{\perp}, z), \quad (77)$$

can be described by a diffusion equation (Ch. 18).

3. Reaction

If for the moment we assume stage 2 to conserve E_{\perp} and give a trend towards equilibrium for fixed E_{\perp} , we may combine formulas in Eqs. (74) and (53) to obtain an expression for the yield of a process with probability distribution $W(\mathbf{r})$ in the transverse plane,

$$\chi(E\psi^2) = \int_0^{\infty} dE_{\perp} g(E_{\perp}) \Pi_{\text{in}}(E_{\perp}) \quad (78)$$

with Π_{in} given by

$$\Pi_{\text{in}}(E_{\perp}) = \frac{A_0}{A(E_{\perp})} \int_{A(E_{\perp})} W(\mathbf{r}) d^2\mathbf{r} . \quad (79)$$

This leads to

$$\chi(E\psi^2) = \int^{\infty} dE_{\perp} \frac{A'(E_{\perp} - E\psi^2)}{A(E_{\perp})} \int W(\mathbf{r}) d^2\mathbf{r} |_{E_{\perp} > U(\mathbf{r})}. \quad (80)$$

In a blocking experiment, particles are emitted isotropically, i.e., with a constant distribution in the variable $E\varphi^2$, where φ is the angle of emission relative to the axis. The distribution $\Pi_{\text{out}}(E_{\perp})$ in transverse energy is therefore

$$\Pi_{\text{out}}(E_{\perp}) = \int d(E\varphi^2) \int d^2\mathbf{r} W(\mathbf{r}) \delta(E_{\perp} - E\varphi^2 - U(\mathbf{r})) = \int_{A(E_{\perp})} W(\mathbf{r}) d^2\mathbf{r}. \quad (79A)$$

The surface transmission is expressed by Eq. (74C), and the yield becomes

$$\chi(E\psi^2) = \int dE_{\perp} \Pi_{\text{out}}(E_{\perp}) / A(E_{\perp}) \int_{A(E_{\perp})} d^2\mathbf{r} \delta(E\psi^2 - E_{\perp} - U(\mathbf{r})), \quad (80A)$$

which is easily seen to be identical to Eq. (80). Thus the reversibility rule is satisfied by the continuum description with statistical equilibrium.

In the halfway-plane description, the distribution $\Pi_{\text{out}}(E_{\perp})$ becomes

$$\Pi_{\text{out}}(E_{\perp}) = \int d(E\varphi^2) \frac{1}{2\pi} \int_0^{2\pi} d\theta \int d^2\mathbf{r} W(\bar{\mathbf{r}}) \delta(E_{\perp} - E\varphi^2 - U(\mathbf{r}^*)), \quad (79B)$$

with $r^{*2} = r^2 + (\varphi d/2)^2 + \varphi d r \cos\theta$ (Fig. 7), and the yield is again obtained from Eq. (80A). It is not difficult to show that reversibility is also satisfied in this description.

In the numerical evaluation of the dip, e.g., in Fig. 9, the expression in Eq. (79B) was used in the following way: Particles were emitted with a distribution of values of (φ, θ) corresponding to the integrals, and for each set of values, E_{\perp} was calculated from the δ -function. The number of ‘events’ falling within an interval $[E_{\perp} - \Delta E_{\perp}/2, E_{\perp} + \Delta E_{\perp}/2]$ gives the value of $\Pi_{\text{out}}(E_{\perp})$ after appropriate normalisation [Andersen 1967].

If we invert the order of integration in Eq. (80) we obtain

$$\chi(E\psi^2) = \int_{A_0} W(\mathbf{r}) f(E\psi^2, \mathbf{r}) d^2\mathbf{r}, \quad (81)$$

where the particle flux is given by

$$f(E\psi^2, \mathbf{r}) = \int_{E_{\perp} > U(r)} dE_{\perp} \frac{A'(E_{\perp} - E\psi^2)}{A(E_{\perp})}. \quad (82)$$

The expressions in Eqs. (78), (81) correspond to the two different pictures we described early in this section. The two convolution integrals are illustrated in Fig. 29 for $\psi = 0$.

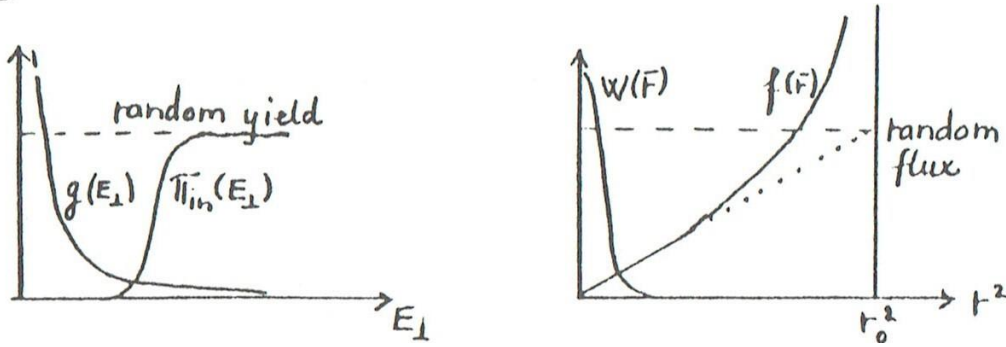


Figure 29.

14. STANDARD MODEL

The expression in Eq. (80) or (81) and (82) for the yield in a channeling experiment is based on approximations that we may refer to as the standard model:

1. Continuum model with conservation of transverse energy.
2. Statistical equilibrium on transverse-energy shell.

In the following, we consider the predictions of this model for the two basic characteristics of a channeling dip: The minimum yield χ_{\min} and the angular width $\psi_{1/2}$. Even when conditions (1) and (2) are not fulfilled, these predictions are useful first approximations. We consider corrections in the following section, mainly for deviations from statistical equilibrium. Lack of conservation of E_{\perp} causing 'dechanneling' is discussed in detail in Ch. 18.

A channeling dip in yield is obtained for nearly substitutional atoms, with a narrow distribution $W(\mathbf{r})$ around $\mathbf{r} = 0$, as illustrated in Fig. 29. The lowest yield is obtained for $\psi = 0$. For this angle, the flux distribution is particularly simple,

$$f(0, \mathbf{r}) = \int_{E_{\perp} > U(r)} dE_{\perp} \frac{d}{dE_{\perp}} \log(A(E_{\perp})) = -\log\left(1 - \frac{r^2}{r_0^2}\right), \quad r \ll r_0. \quad (83)$$

Close to strings, the flux is proportional to r^2 ,

$$f(0, \mathbf{r}) \cong r^2/r_0^2. \quad (84)$$

This expression can be used if the function $W(\mathbf{r})$ is confined to small distances, and we obtain a simple formula for the minimum yield, $\chi_{\min} = \chi(0)$,

$$\chi_{\min} = \int \frac{r^2}{r_0^2} W(\mathbf{r}) d^2\mathbf{r} = Nd\pi\langle r^2 \rangle. \quad (85)$$

It is remarkable that this formula does not depend on any potential parameters. It is purely geometrical. To see this clearly, it is perhaps useful to rewrite formula (82) for the particle flux. We introduce the differential area $A'(E_{\perp} - E\psi^2) dE_{\perp}$ at a potential contour corresponding to $U(\mathbf{r}') = E_{\perp} - E\psi^2$ (see Fig. 26) and obtain

$$f(E\psi^2, \mathbf{r}) = \int_{E\psi^2 + U(\mathbf{r}') > U(\mathbf{r})} \frac{dA(\mathbf{r}')}{A(E\psi^2 + U(\mathbf{r}'))}. \quad (86A)$$

The interpretation is simple: A particle incident at \mathbf{r}' obtains the transverse energy $E_{\perp} = E\psi^2 + U(\mathbf{r}')$ and is confined to move inside the area $A(E_{\perp})$, with uniform probability in statistical equilibrium. The only assumption about the potential which is made in Eq. (83) is that it is cylindrically symmetric and repulsive, which certainly is fulfilled at small distances r , as required in Eqs. (84) and (85). For close-encounter processes $\langle r^2 \rangle = \rho^2$ and we obtain

$$\chi_{\min} = \frac{\rho^2}{r_0^2} = Nd\pi\rho^2. \quad (86B)$$

Since $r_0 \sim 1 \text{ \AA}$ and $\rho \sim 0.1 \text{ \AA}$, $\chi_{\min} \sim 10^{-2}$.

At incidence angles $\psi \sim \psi_1$, the surface transmission is not very important since all particles contribute significantly to the yield, and the majority are incident on the surface far from strings where $U \ll E\psi_1^2$. Hence we can use the result in Eq. (56) for the halfwidth,

$$\psi_{1/2} \cong \psi_1 \left[\frac{1}{2} \log \left(\frac{(Ca)^2}{\rho^2 \log(2)} + 1 \right) \right]^{1/2}. \quad (86C)$$

We shall discuss the accuracy of these results, characterizing the dip in yield, in the following section.

For broader distributions $W(\mathbf{r})$ or for distributions centred away from strings, the simple approximations applied here break down. The flux distribution in Eq. (82) must be evaluated with a potential including contributions from several strings ('multistring potential'), and surface transmission will be important also for the width. An example is illustrated in Fig. 30, showing measurements of the dip in

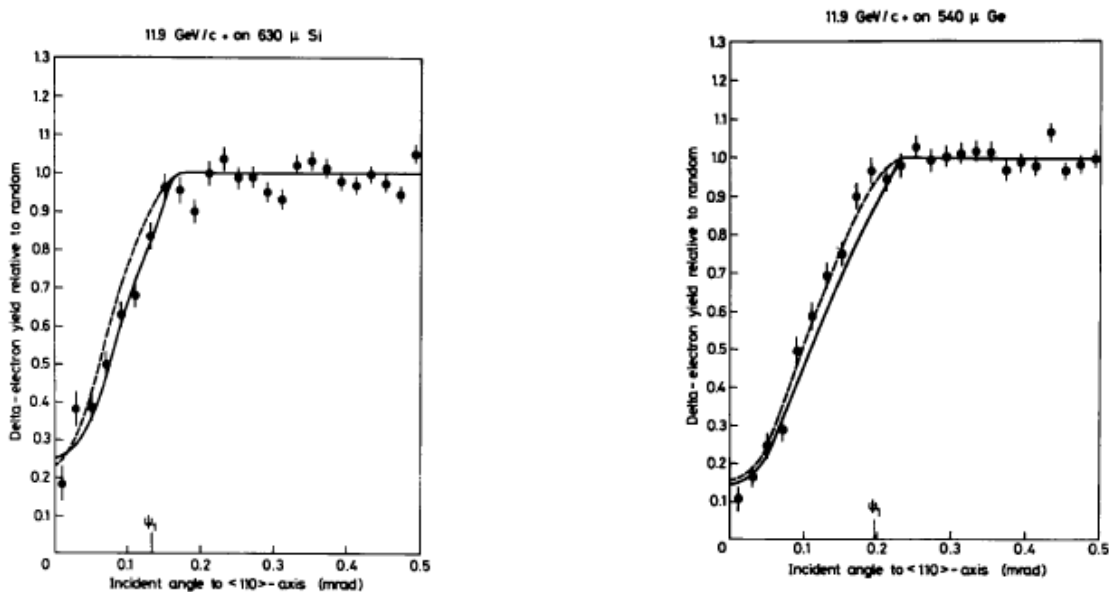


Fig. 30. $\langle 110 \rangle$ dips in δ -electron yield for 11.9-GeV/c protons and π^+ in a 630- μm Si crystal (left) and 540- μm Ge crystal (right). The curves represent calculations in the standard model, with a thermally averaged multistring potential and the corresponding electron density: dashed curve, standard potential, solid curve, DoyleTurner. From [Bak *et al.* 1982].

yield of δ -electrons (high-energy secondary electrons). Numerical calculations have been made both with the standard potential and with the Doyle-Turner potential, with the corresponding electron densities. The agreement is remarkable, although it is a bit surprising that the Ge measurement seems to favour the standard potential.

Even for this case, we can make reasonable estimates with our simple formulas. For the minimum yield, we use Eq. (78) with the Π_{in} function given by Eq. (63),

$$\chi_{\min} \cong \int_0^{r_0^2} \frac{d(r^2)}{r_0^2} \left(1 + \frac{r^2}{(ca)^2}\right)^{-1} = \left(\frac{ca}{r_0}\right)^2 \log\left(1 + \frac{r_0^2}{(ca)^2}\right). \quad (87)$$

For $\langle 110 \rangle$ Si, this leads to $\chi_{\min} = 18\%$ which is not so far from the value in Fig. 30. The halfwidth is close to the value given by Eq. (64) when defined as the angle corresponding to a yield halfway between χ_{\min} and random.

At large distances from strings, the flux is higher than in the random case, as shown in Fig. 29, and a peak in yield is predicted for, e.g., reactions with an interstitial atom. An example of an observation of this effect is shown in Fig. 31. It is in the literature

denoted ‘flux peaking’ for obvious reasons. In calculations of such peaks it is of course particularly important to use a multi-string potential.

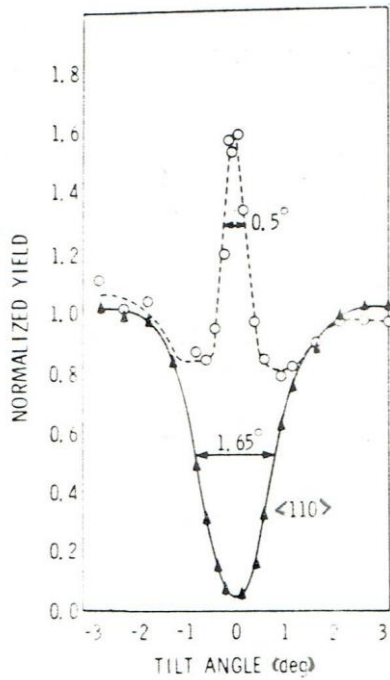


Fig. 31. Backscattering yield for 1-MeV He in Si implanted with 5×10^{14} Yb/cm² (60 keV, 450°C). The high yield for Yb (open circles) was the first indication of a strong flux-peaking effect. From [Andersen *et al.* 1971].

In [Andersen *et al.* 1971], a simple estimate of the peak height was given. If we assume that a central area A_1 in the middle of the channel is effectively flat, the area function has a step $\Delta A = A_1$ at $E_{\perp} = 0$, and the derivative is a δ -function, $A_1 \delta(E_{\perp})$. Integration of Eq. (82) for $\psi = 0$ then results in a flux at the centre, given by

$$f(A_1) = 1 + \log\left(\frac{A_0}{A_1}\right). \quad (88)$$

Again, it is easy to understand this result: The log term comes from particles incident outside A_1 , and those incident inside A_1 are confined to remain there, so they alone give the random flux. An effectively flat area in the centre of the channel can result, e.g., from beam divergence or multiple scattering, which prevents the flux from being ‘trapped’ by the very weak potential (see Fig. 12). A more satisfactory procedure is to include such effects in the surface transmission and in the depth development of $g(E_{\perp}, z)$ (Eq. (77)).

The transition from a substitutional dip in yield to a flux peak is illustrated in Fig. 31a. The curves are calculated in the standard model for the indicated displacements r_d towards the centre of a $\langle 110 \rangle$ channel in Al. For small displacements, the minimum yield changes by a large factor. It may be evaluated from Eq. (85) with $\langle r^2 \rangle = \rho^2 + r_d^2$. But the absolute change is small and in an experiment, it may be easier to establish the large change in width. For both quantities, it is important to take into account the corrections discussed in the following section.

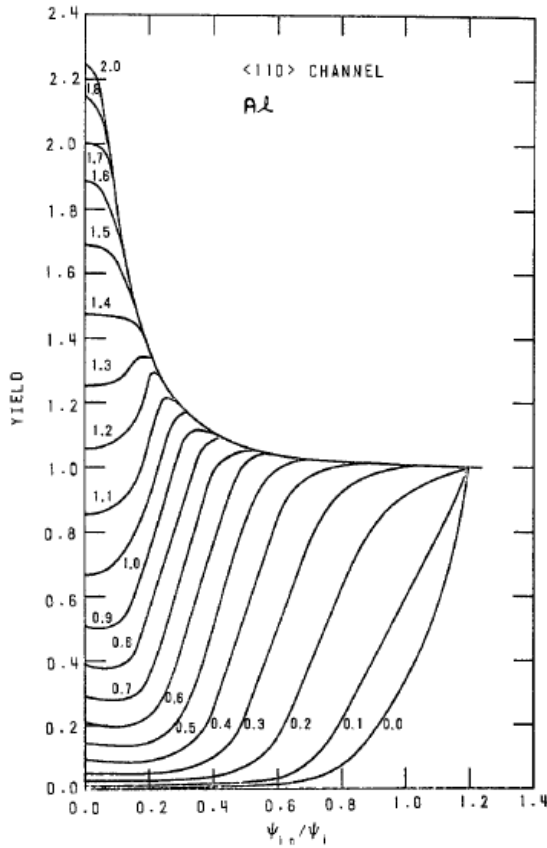


Fig. 31a. Calculation in the standard model, with a thermally averaged multi-string potential, of the close encounter yield from a solute atom with varying displacement from a $\langle 110 \rangle$ string in Al towards the centre of a $\langle 110 \rangle$ channel. The displacement in Å is indicated at the curves. From [Matsunami *et al.* 1978].

For planes, analogous considerations apply but the flux expression is complicated by the non-uniformity of the equilibrium distribution for fixed E_{\perp} . The analogue of Eq. (81) is simple,

$$\chi(E\psi^2) = \int_{-d_p/2}^{d_p/2} W(x) f(E\psi^2, x) dx, \quad (89)$$

where $x = 0$ corresponds to the centre of a plane. The flux distribution is given by

$$f(E\psi^2, x) = \int dx' \frac{K(E\psi^2 + V(x'))}{[E\psi^2 + V(x') - V(x)]^{1/2}} \Big|_{E\psi^2 + V(x') - V(x) > 0} \quad (90)$$

The function $K(E_{\perp})$ is determined by the normalisation condition,

$$\int_{E_{\perp} > V(x)} \frac{K(E_{\perp})}{(E_{\perp} - V(x))^{1/2}} \cdot \quad (91)$$

In the simple, and not very unrealistic case of a harmonic potential [Feldman *et al.* 1982], $V(x) = \frac{1}{2}k(d_p/2 - |x|)^2$, normalisation is independent of E_{\perp} ,

$$K(E_{\perp}) = \frac{1}{\pi} \left(\frac{k}{2} \right)^{1/2} \quad (\text{harm. pot.}) \quad (92)$$

The flux can then be evaluated analytically for $\psi = 0$,

$$f(0, x) = \frac{2}{\pi} \operatorname{acosh} \left(\left[1 - \frac{2|x|}{d_p} \right]^{-1} \right) \quad (\text{harm. pot.}), \quad (93)$$

where acosh is the inverse hyperbolic cosine. Qualitatively, this flux is similar to the axial flux in Eq. (83). It is zero at the plane, $x = 0$, and diverges at the centre of the channel, $|x| = d_p/2$, as illustrated in Fig. 32.

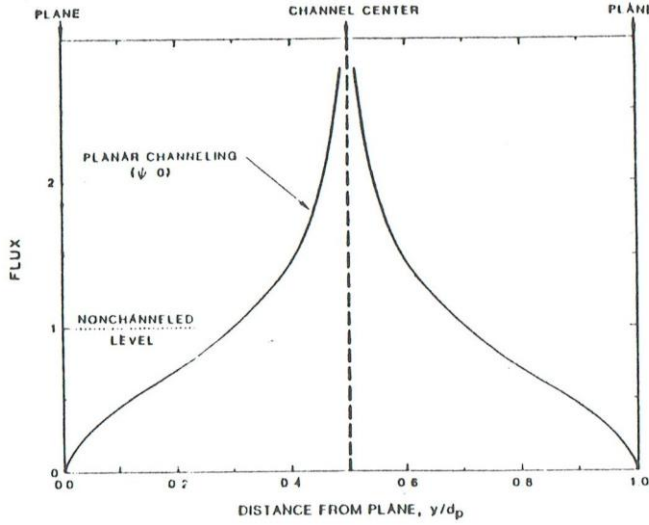


Fig. 32. The flux distribution in a planar channel for zero angle of incidence to the plane for a harmonic planar potential (Eq. (93)). From [Feldman *et al.* 1982].

We can use the expression in Eq. (93) to obtain an estimate of the minimum yield. A simple geometrical analogy to the axial result in Eq. (86) would lead to $\chi_{\min} \sim \sqrt{2\rho/d_p}$ since the mean-square displacement in one dimension is $\rho^2/2$. For $d_p = 1.92$ and $\rho = 0.11 \text{ \AA}$ (Si {110}, room temp.), the value is $\chi_{\min} = 8\%$. However, since in one-dimensional equilibrium, the intensity for fixed E_{\perp} is high where the potential is high, a considerable enhancement over this value may be expected.

For small displacements x , the flux (93) may be approximated by

$$f(0, x) \cong \frac{4}{\pi} \left(\frac{|x|}{d_p} \right)^{1/2} \quad (94)$$

since $\cosh(\varepsilon) \sim 1 + \varepsilon^2/2$ and hence $\operatorname{acosh}(1 + \delta) \sim (2\delta)^{1/2}$. For a Gaussian displacement distribution,

$$W(x) = (\pi\rho^2)^{-1/2} \exp\left(-\frac{x^2}{\rho^2}\right), \quad (95)$$

we can evaluate the integral in Eq. (89),

$$\chi_{\min} \cong \int_{-\infty}^{\infty} dx \frac{4}{\pi} \left(\frac{|x|}{d_p} \right)^{1/2} (\pi \rho^2)^{-1/2} \exp\left(-\frac{x^2}{\rho^2}\right) = \frac{8}{\pi^{3/2}} \left(\frac{\rho}{d_p} \right)^{1/2} \int_0^{\infty} d\xi \xi^{1/2} \exp(-\xi^2) = \frac{2}{\pi^{1/2}} \Gamma\left(\frac{3}{4}\right) \left(\frac{\rho}{d_p} \right)^{1/2} = 0.9 \left(\frac{\rho}{d_p} \right)^{1/2}. \quad (96)$$

For our example above, this leads to $\chi_{\min} = 22\%$, an increase by a factor of three over the geometrical estimate. Compared to the axial case, the minimum yield is higher by an order of magnitude. And in contrast to that case, the value does depend on details of the potential. Thus, it is important in quantitative calculations to include the thermal smearing of the potential.

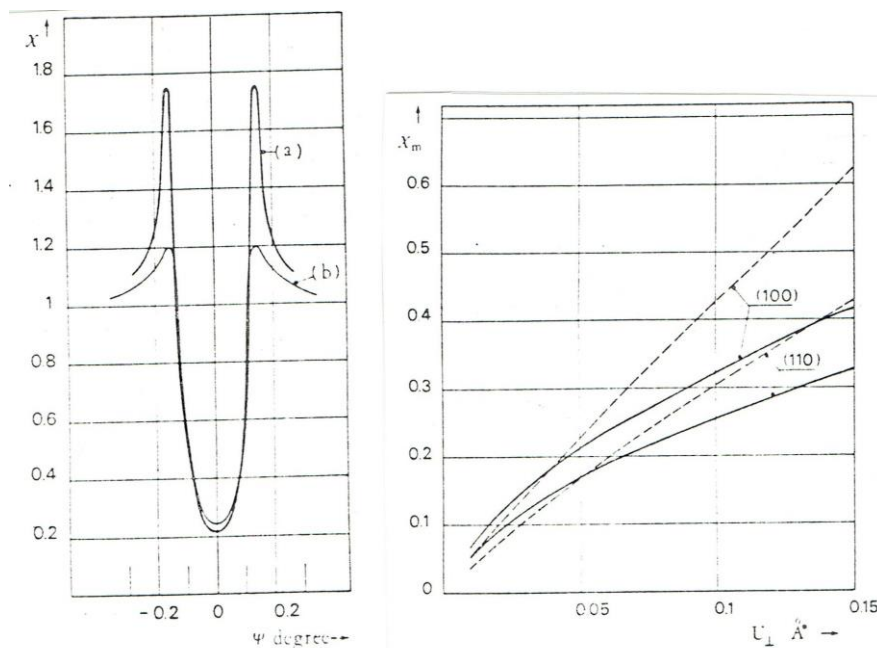


Fig. 33. Continuum-model calculations of planar dips for 3-MeV protons along a (110) plane in Si, with a thermally averaged potential from two planes. The influence of multiple scattering over a depth of 5000 Å has been estimated (curve (b) in the left-hand figure and dashed lines in the right-hand figure). U_{\perp} here denotes the vibrational amplitude in one dimension. From [Poizat and Remillieux 1971].

In numerical calculations with the standard potential from one plane, Eq. (24), a minimum yield of $\chi_{\min} = 16\%$ was obtained for our example above (Si{110}) [Picraux and Andersen 1969]. Later, these calculations were improved [Poizat and Remillieux 1971] by including the potential from two neighbouring planes and using the thermally averaged Molière potential, shown in Fig. 6. The resulting dip is shown in Fig. 33 ("Fig. 1(a)"). The minimum yield is increased to 21.5%. The dependence of χ_{\min} on $U_{\perp} \equiv \rho/\sqrt{2}$ is also shown ("Fig.2", solid line labelled (110)). It is close to the square root proportionality given in Eq. (96). Later, calculations with a thermally averaged Doyle-Turner potential (Eq. (19b)) from two planes have been performed [B. Bech Nielsen, private communication]. The results are very close to those given in Fig. 33, but the minimum yield is slightly higher, $\chi_{\min} \sim 22.5\%$.

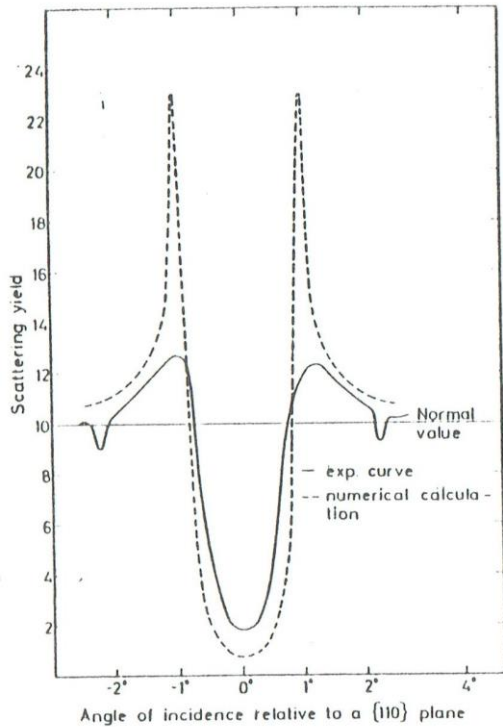


Fig. 34. Measurement and calculation of planar dip for 480-keV protons along (110) plane in W. The static standard potential from one plane has been applied. From [Andersen 1967].

In experiments, a value of $\chi_{\min} \sim 30\%$ is obtained, but the discrepancy may be due to multiple scattering ('dechanneling'). Estimates of this effect were made by [Picraux and Andersen 1969] and [Poizat and Remillieux 1971], and the curve labelled Fig. 1(b) in our Fig. 33 includes multiple scattering over 5000 \AA . The most dramatic influence of multiple scattering is the reduction of the very high and narrow shoulders, which indeed have only been observed in experiments with extremely high depth resolution.

Also the halfwidth of the dip turns out to be reproduced well when thermal averaging of the potential and multiple scattering is included [Poizat and Remillieux 1971]. Compared to calculations with the static standard potential and conservation of E_{\perp} , the measured widths were found generally to be smaller by 20-25%. An example of such a comparison is shown in Fig. 34.

15. CORRECTIONS TO χ_{\min} AND $\psi_{1/2}$

The dramatic reduction by about two orders of magnitude of the close-encounter yield by the string effect is the most important channeling effect, and one would like to be able to calculate χ_{\min} accurately. However, as mentioned earlier, the situation is for zero angle of incidence to an axis the worst possible one for application of the simplifying approximations, conservation of E_{\perp} , and statistical equilibrium for fixed E_{\perp} . A thorough analysis of this problem was made by Barrett on the basis of Monte-Carlo simulation of channeling [Barrett 1971]. His conclusion was that the formula in Eq. (86B) must be corrected by a factor $C \sim 2.5$,

$$\chi_{\min} \cong CNd\pi\rho^2. \quad (97)$$

(Do not confuse this C with the constant $C \sim \sqrt{3}$ in the standard potential).

There are two main reasons for this correction. First, the distribution $g(E_{\perp})$ after surface transmission, Eq. (73) for $\psi = 0$, must be corrected for single and multiple hard collisions in the first deflection by a string. Figure 35 shows a comparison between the distribution obtained from Eq. (73) and from a Monte-Carlo simulation. The main difference is a long tail towards high E_{\perp} in the computer simulation. This effect alone accounts for about a factor of 1.5 on χ_{\min} . With increasing energy of the projectiles, this factor decreases slowly, as should be expected since the continuum description of the string collisions should improve.

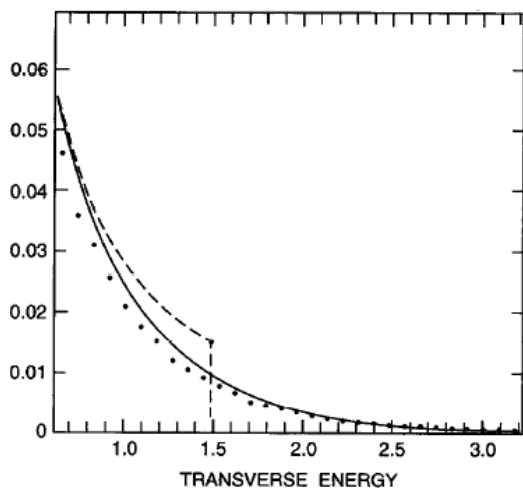


Fig. 35. Distribution in transverse energy, in units of $E\psi_1^2$, after surface transmission of 1-MeV H along a $\langle 110 \rangle$ axis in Si. The dashed curve is calculated in the continuum model, with a thermally averaged standard potential and the points are from a Monte-Carlo simulation. The full curve includes thermal multiple scattering calculated with the diffusion model, Ch. 18, applied to the first collision with a string. From [Andersen *et al.* 1994].

The second effect is illustrated in Figs. 36-38. In Fig. 36 are shown results of a computer simulation [Barrett 1973]. As the title of the paper indicates, Barrett claimed that the assumption of a trend towards statistical equilibrium in transverse phase space is contradicted by the simulations. For incidence parallel to an axis, the particles contributing to the yield of a close-encounter reaction impinge on the surface near a string and acquire a transverse energy of order $E\psi_1^2$. As illustrated in Fig. 36, such particles are focussed by deflection on neighbouring strings onto

another string, and this will continue. Hence they spend more time close to strings than for a spatial distribution corresponding to statistical equilibrium (Eq. (52)). The minimum yield is therefore enhanced over the prediction in Eq. (86B).

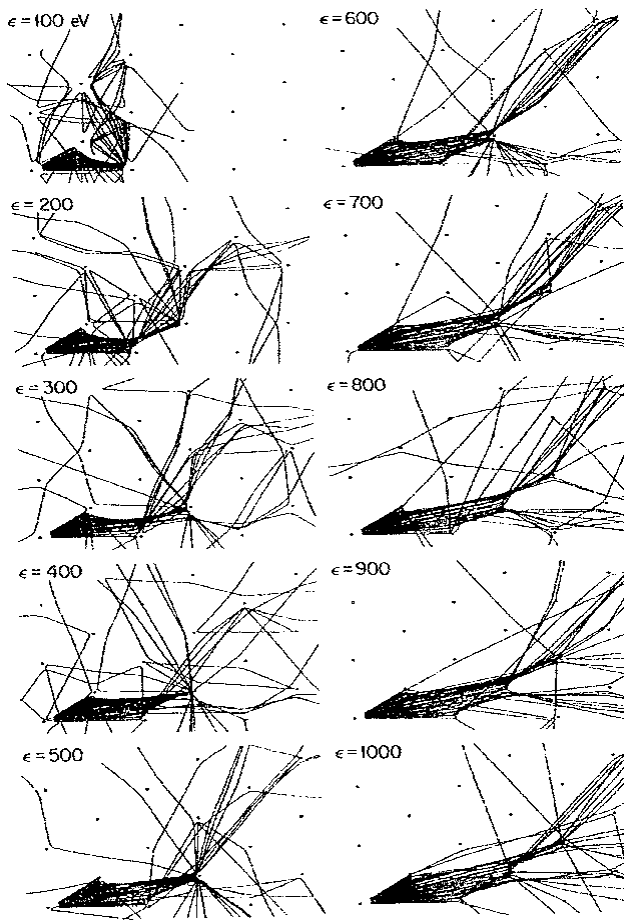


Fig. 36. Projection onto (111) plane of trajectories of 3-MeV protons moving nearly parallel to [111] direction in tungsten at 1200 K. The transverse energy ϵ is given for each simulation. From [Barrett, 1973].

From a general point of view, such a deviation from a rapid trend towards statistical equilibrium in the transverse phase space is expected to be rooted in a symmetry and a corresponding conservation law. A typical example is conservation of angular momentum, restricting the accessible phase space. The regular arrangement of strings and conservation of transverse energy relative to major planes could here be the explanation. Particles starting near a string, as in Fig. 36, cannot become channeled relative to major planes, and the accessible transverse phase space is restricted by the absence of such trajectories.

A study of this idea, based on computer simulation, was the subject of a thesis project (“speciale”) [Eriksen 1980]. The transverse motion in the continuum potential was evaluated numerically for a situation corresponding to incidence at $\psi = 0$. As in Fig. 36, particles with a given transverse energy $E_{\perp} = U(r)$ then start their motion in a ring with radius r around a string and move away radially due to the repulsive potential. Their angular distribution was recorded when, during their motion through the transverse plane, they happened to pass through central regions of a channel (A and B in Fig. 37b).

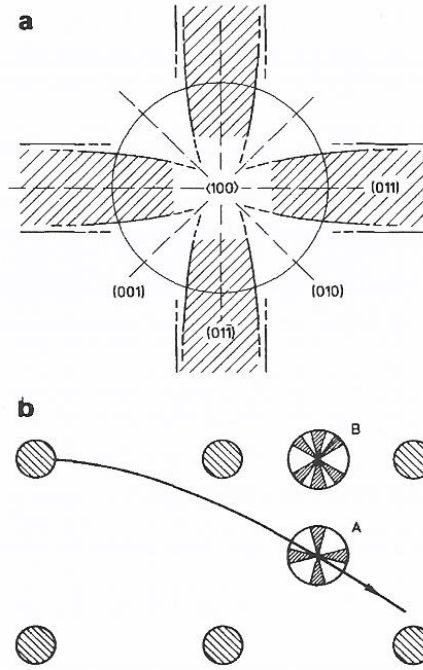


Fig. 37. **a)** Governing of the motion by planar channeling in the angular region around a $\langle 100 \rangle$ axis, for particles moving through the centre of $\langle 100 \rangle$ axial channels in a bcc lattice (region A below). The circle has radius ψ_1 , and $\{110\}$ planar channeling (or governing by strings of strings) is indicated by the hatched angular regions. **b)** In the computer simulation, the motion is started at a distance r from a string, with transverse energy $U(r)$. The particle moves through many unit cells and the direction of \bar{p}_\perp is recorded in the central regions equivalent to A and B. The blocked angular regions are indicated at these two positions by hatched areas. From [Andersen and Uguzzoni 1990].

Figure 38 shows the angular distributions of \bar{p}_\perp , recorded at positions equivalent to A and B in Fig. 37b for a fairly large transverse energy, $E_\perp = 1.25 E\psi_1^2$. In the A regions, large angular regions around the planar directions $\varphi = 0$ (vertical) and $\varphi = \pi/2$ (horizontal) are empty (in the figure the azimuthal angle is denoted by θ), owing to blocking by planes: Planar-channeled particles cannot get close to planes and, by reversibility, such trajectories are therefore not populated when particles are ‘emitted’ close to planes. At B there is no dip in the horizontal direction because the trajectories in this direction are not channelled. Similarly, there are dips along the (010) and (001) planes at B but not at A.

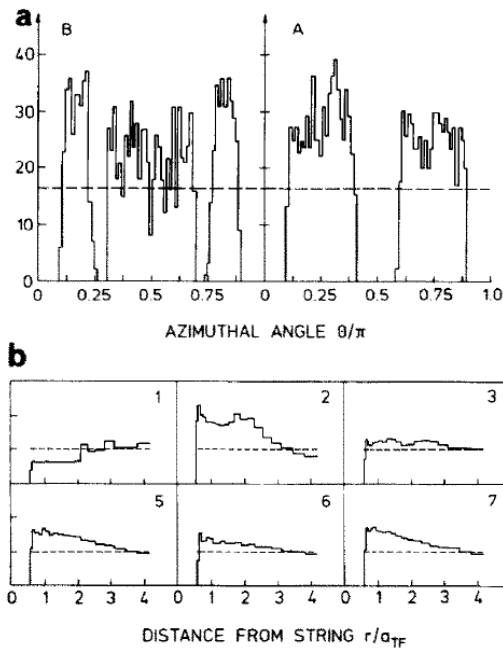


Fig. 38. **a)** Distribution of the direction of \bar{p}_\perp , recorded in the regions B and A in Fig. 37, for particle trajectories starting at the potential contour $U(r) = 1.25 E\psi_1^2$ with $p_\perp = 0$. The yield was registered over a depth region of 16 times the distance d_s between $\langle 100 \rangle$ strings. The horizontal (011) planar direction corresponds to $\theta = \pi/2$. The dashed line indicates the average intensity. Usually, the azimuthal angle is denoted by φ and this notation is used in the text.

b) Flux for the same particles, as a function of the distance to the nearest string, recorded over depth intervals corresponding to transverse motion from $(2n-1)d_s$ to $2nd_s$ after emission from a string, where n is given in the upper left corner. The flux corresponding to statistical equilibrium is indicated by dots. From [Andersen and Uguzzoni 1990].

If \mathbf{p}_\perp were isotropic far from strings, we have seen that the spatial distribution would be uniform, i.e., would correspond to a statistical equilibrium. If the density in the restricted phase space is uniform, the absence of \mathbf{p}_\perp directions corresponding to trajectories with low probability close to strings must lead to a spatial distribution with enhanced probability of being close to strings. This is confirmed by the computer simulation, as seen in Fig. 38b. The spatial density close to strings has been recorded for trajectories starting at a potential contour corresponding to $U(r) = 1.25 E\psi_1^2$, as illustrated in Fig. 37b. The distributions in r were accumulated over sequential depth intervals of about $2d_s/\psi_1$, where d_s is the distance between neighbouring strings.

In the first few intervals, there are considerable oscillations of the distribution, and χ_{\min} exhibits corresponding oscillations (cf. Fig. 27). However, the oscillations are damped fairly quickly. We note that the value of λ_\perp in Eq. (67) corresponds to the third interval in Fig. 38b. The development may be described as a trend towards a uniform density in the restricted phase space, the restriction being the exclusion of planar-channeled trajectories [Andersen and Uguzzoni 1990]. This may also be formulated as restriction in phase space due to a conservation law, conservation of transverse energy in planar channeling.

The enhancement of the probability close to strings is about a factor 1.5, and this is the second contribution to the Barrett factor C in Eq. (97). We have seen that it is closely connected to the angular distribution of \mathbf{p}_\perp and the connection may even be quantified. Denote by

$$P_0^R(\mathbf{r}, \mathbf{p}_\perp) d^2\mathbf{r} d^2\mathbf{p}_\perp \quad (98)$$

the distribution in the restricted equilibrium. The spatial distribution is obtained upon integration over \mathbf{p}_\perp ,

$$P_0^R(\mathbf{r}) = \int d^2\mathbf{p}_\perp P_0^R(\mathbf{r}, \mathbf{p}_\perp). \quad (99)$$

We assume, in accordance with Fig. 37, that the distribution in Eq. (98) is uniform in the restricted phase space, i.e.,

$$P_0^R(\mathbf{r}, \mathbf{p}_\perp) \propto R(\mathbf{r}, \varphi) \delta\left(E_\perp - \frac{p_\perp^2}{2M_1} - U(\mathbf{r})\right), \quad (100)$$

where $R(\mathbf{r}, \varphi)$ is either 0 or 1, depending on whether the angle φ of the momentum is inside the blocked region or not. The differential element in Eq. (99) is proportional to $d\left(\frac{p_\perp^2}{2M_1}\right) d\varphi$, and hence the integration leads to a spatial distribution proportional to the restriction factor

$$R(\mathbf{r}) = \frac{1}{2\pi} \int_0^{2\pi} d\varphi R(\mathbf{r}, \varphi). \quad (101)$$

The constant of proportionality is determined by normalisation, and inside the allowed area $A(E_{\perp})$ we obtain

$$P_0^R(\mathbf{r}) = \frac{R(\mathbf{r})}{\langle R \rangle} \frac{1}{A(E_{\perp})}, \quad (102)$$

where $\langle R \rangle$ denotes the average over $A(E_{\perp})$ of the restriction factor in Eq. (101).

According to Fig. 38a, the value of R in the central region of the channel is $R \sim 0.6$ (Eq. 101). In areas with less symmetry, the simulation showed larger values of R , as would be expected, and hence $\langle R \rangle$ must be somewhat larger than 0.6. Close to strings, there is no restriction in φ , i.e. $R(r_m)=1$, and the allowed area is close to A_0 ,

$$P_0^R(r_m) = \frac{1}{A_0 \langle R \rangle} \quad (103)$$

These considerations are consistent with the about 50% enhancement observed in Fig. 38b.

In contrast to the correction to the continuum picture of surface transmission, the correction of the spatial equilibrium distribution does not depend on projectile energy. In the high-energy limit, the Barrett factor should therefore approach a value $C \sim 1.5$, corresponding to the influence of planar blocking, only.

An important question is the dependence of the correction factor on the magnitude of $\langle r^2 \rangle$ in Eq. (85). Channeling and blocking dips are used to determine displacements of impurity atoms and of recoiling compound nuclei decaying by charged-particle emission, and the displacement is extracted from Eq. (85) with a correction factor. Often the Barrett value $C = 2.5-3.0$ has been used.

From our discussion, we see that it would be more correct to include single and multiple scattering during surface transmission as an additive correction. The minimum yield is essentially an integral of $g(E_{\perp})$ from $E_{\perp} \sim E\psi_{1/2}^2$ to infinity, where $E\psi_{1/2}^2$ is the halfwidth of the Π_{in} function in Eqs. (78) and (79). With increasing $\langle r^2 \rangle$ this lower limit of integration decreases and χ_{min} increases. However, the high- E_{\perp} tail of $g(E_{\perp})$, shown in Fig. 35, is already included for $\langle r^2 \rangle = \rho^2$. We may therefore expect a formula of type

$$\chi_{min} = Nd\pi[C'(\langle r^2 \rangle - \rho^2) + C\rho^2] \quad (104)$$

to apply, with $C \sim 2.5$ and $C' \sim 1.5$. This latter value derives from blocking by planes that according to Fig. 37 is not very dependent on E_{\perp} and therefore should be nearly independent of $\langle r^2 \rangle$. Similar results were arrived at by [Sharma *et al.* 1973] and by [Barrett *et al.* 1976].

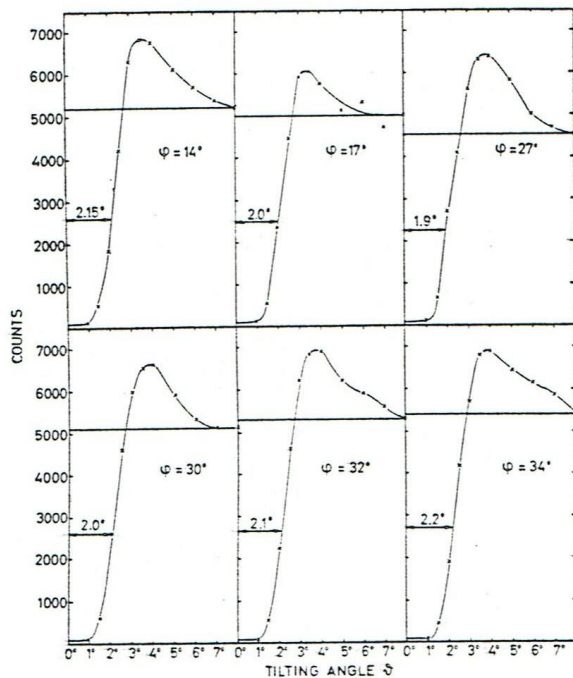
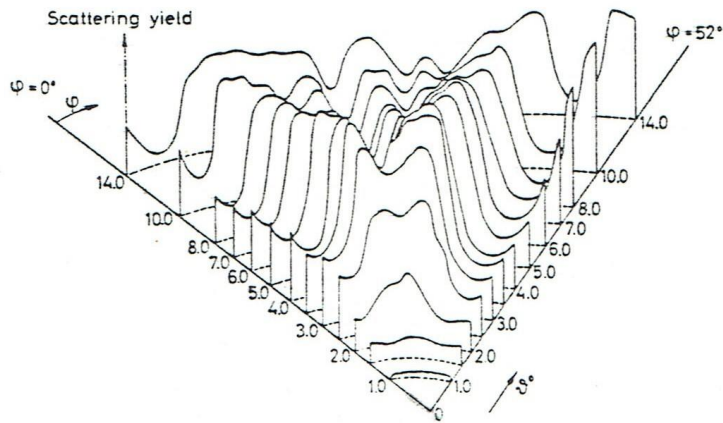


Fig. 39. Three-dimensional map of backscattering yield around $\langle 100 \rangle$ direction in W of 400-keV H^+ . At the time we did not have present days fancy plotting programs and the 3D-structure was constructed with tin foil! The curves in the lower figure correspond to scans through the axis at different azimuthal angles (from [Andersen and Uggerhøj 1968]).

Also the simple formula for the halfwidth in Eq. (87) needs correction in quantitative comparisons with experiments. First, one should be aware of the influence of planar effects on a scan through an axis, as visualised in Fig. 10. A three-dimensional mapping of the backscattering yield around an axis is shown in Fig. 39. Clearly a scan through the axis ($\theta = 0$) at a fixed value of φ depends on the choice of φ . The dips shown in the lower part of the figure correspond to different values of φ in between the planes. The halfwidth varies by about 15%. Also the shoulders are strongly influenced by the planes and are larger than predicted by calculations (see Fig. 16).

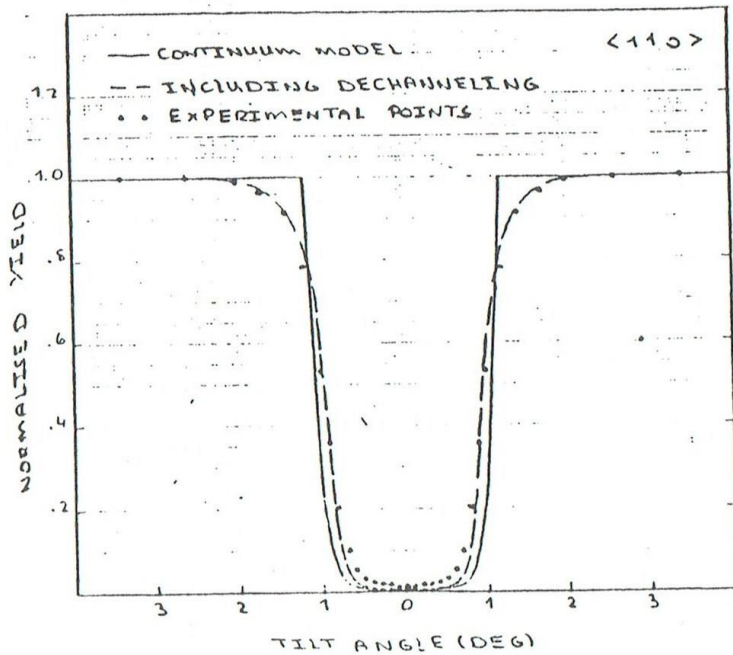


Fig. 40. Comparison of experiment and calculations for $\langle 110 \rangle$ dip in backscattering yield of 750-keV ^3He in Si. The target temperature was 30K, corresponding to a vibrational amplitude $\rho = 0.07\text{\AA}$. The solid curve is a standard-model calculation with a thermally averaged Doyle Turner potential, and the dashed curve includes dechanneling. The experimental points are averages over azimuthal angles. (B. Bech Nielsen, private communication 1986).

To a large extent, the planar structure may be eliminated by an average over the azimuthal angle φ , which in effect establishes a statistical equilibrium in E_{\perp} and hence also, as we have seen, in transverse space. A measurement of this kind is compared with continuum-model calculations in Fig. 40. A thermally averaged Doyle-Turner potential (Eq. 19a) was used. Compared to a calculation with the standard potential (Eq. (86C)), the halfwidth is reduced by 15-20%. When multiple scattering to the depth of $\sim 1500\text{\AA}$ is included (dashed curve), there is a further reduction of about 10%, and the measured width is reproduced extremely well. We note that the shoulders are absent. The large shoulders are an artefact caused by shoulders on planar channeling dips. The value of $\rho/d\psi_1$ is above unity in Fig. 40; the shoulders on the axial dip are then small and the continuum model should give a reliable value of the halfwidth at half dip, $\psi_{1/2}$ (see Fig. 8).

The excellent agreement between theory and experiment demonstrated in Fig. 40 solves a long persisting mystery. The widths of axial dips were generally found to be lower by $\sim 20\%$ than calculated (Fig. 41). The lesson is that all of the following points are important for quantitative agreement for the width:

1. Azimuthal average of yield.
2. Accurate atomic potential.
3. Thermal average.
4. Multiple scattering.

The last point will be discussed in detail in Chs. 17, 18.

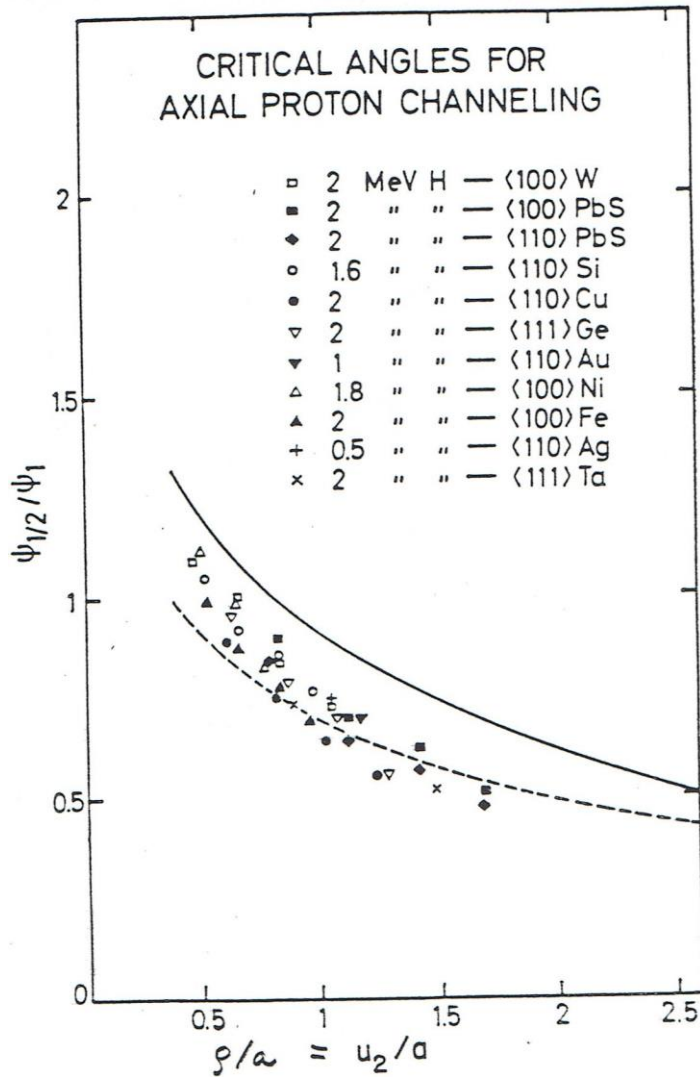


Fig. 41. Systematic measurements of critical angles (halfwidths) for axial dips, extrapolated to zero depth. The solid curve is from the standard model with a static potential, while the dashed curve is an estimate derived from Monte-Carlo simulations by Barrett (from [Andersen and Lægsgaard 1972]).

16. COMPENSATION RULES

We shall discuss in this section two general rules, angular and spatial compensation. They are general in the sense that their validity is not limited by the conditions for various approximations, like conservation of transverse energy or statistical equilibrium. In Ch. 10, we discussed another rule of this kind, the rule of reversibility, and we saw that it was fulfilled in the continuum approximation with statistical equilibrium. In contrast, it turns out that the rule of angular compensation is violated, and this is an important limitation of the approximation.

The general rules not only serve as tests of approximations but may be of direct practical importance: If, for example, a target used for measurement of a nuclear

reaction has polycrystalline structure, it is important to know that the target nuclei on the average are subjected to the same projectile flux as in an amorphous target.

Spatial compensation

First we consider the rule of spatial compensation. As we have seen from the detailed estimates in previous sections, the dip in yield for reaction with atoms on lattice sites turns into a peak for positions between atomic rows or planes, the so-called flux-peaking effect (see Fig. 31). When we apply the ‘flux picture’ in Eq. (81), illustrated in Fig. 29, this is easy to understand. Let $\chi(\psi, \varphi, \mathbf{r}, z)$ denote the probability, normalised to the random case, for a particle with incidence direction relative to an axis specified by angles ψ and φ to hit a point in the crystal at depth z and transverse coordinate \mathbf{r} in the unit cell A_0 . This is identical to the definition of the particle flux, and we may write down immediately a compensation rule,

$$\frac{1}{A_0} \int_{A_0} d^2\mathbf{r} \chi(\psi, \varphi, \mathbf{r}, z) = 1 \quad . \quad (105)$$

The analogous expression for planes is straightforward.

Eq. (105) expresses conservation of particle flux which, except near the end of the particle range, is very accurately fulfilled since the backscattered fraction of the beam is very small ($\sim 10^{-4}$ for 1-MeV He in 1- μm Si). In the blocking case, where $\chi(\psi, \varphi, \mathbf{r}, z)$ denotes the probability for a particle emitted at (\mathbf{r}, z) to emerge from the crystal with angles (ψ, φ) , the compensation rule does not have such a simple interpretation. However, from the rule of reversibility it follows that spatial compensation must be obeyed by blocking patterns, provided that energy loss can be neglected.

Angular compensation

This rule states that, e.g., the yield missing at small angles to an axis or a plane for reaction with a substitutional atom should be present as an excess at larger angles, i.e.,

$$\int_0^{2\pi} d\varphi \int_0 \sin\psi d\psi [\chi(\psi, \varphi, \mathbf{r}, z) - 1] = 0 \quad , \quad (106)$$

where the last integral should extend to angles much larger than the critical angle but still small. For planes, the compensation integral is one-dimensional, as for spatial compensation.

For blocking, this rule simply expresses conservation of particles, but the interpretation for the channeling case is less straightforward. From the general rule of reversibility it follows, however, that the rule must be obeyed provided that energy loss can be neglected.

We now turn to the question whether angular compensation is fulfilled by the standard model, the continuum approximation with statistical equilibrium. For

simplicity, we ignore surface transmission and consider emission from an isolated string or plane. It is easy to see that surface transmission does not alter the conclusions of the following analysis.

Let us look at the planar case first. A particle emitted at distance x and at angle ψ_e to a plane obtains a transverse energy $E\psi^2 = E\psi_e^2 + V(x)$. The emission is isotropic in the one-dimensional variable ψ_e , and we obtain for the compensation integral to a finite angle $\psi_0 \gg \psi_e$,

$$\int_0^{\psi_0} [\chi(\psi, x) - 1] d\psi = (\psi_0^2 - V(x)/E)^{1/2} - \psi_0 \approx \frac{V(x)}{2E\psi_0^2}. \quad (107)$$

Thus the integral converges rapidly towards zero with increasing angle ψ_0 and compensation is essentially obtained within an angle of a few times ψ_p .

The compensating shoulders on dips are very pronounced in the planar case, as illustrated in Figs. 33 and 34 but are quickly broadened and lowered by multiple scattering. The yield close to an axis is strongly influenced by planar effects, and as seen, e.g., in Fig. 39, planar effects (shoulders) give rise to apparent high shoulders on an axial scan. However, such effects may be eliminated by circular averaging, as shown in Fig. 40.

Although the compensation rule in Eq. (106) has the simplest interpretation in the blocking case, it is not difficult to understand the high yield for particles incident on a crystal at angles just outside the dip. Close to planes, such particles have a small transverse velocity and a high probability density. They spend a long time near planes and hence give a high yield.

We now turn to the axial case. For an isolated string, we have azimuthal symmetry, and the analogue of Eq. (107) is

$$\pi \int_0^{\psi_0^2} [\chi(\psi, \mathbf{r}) - 1] d(\psi^2) = \pi \left[\psi_0^2 + \frac{U(r)}{E} - \psi_0^2 \right] = -\frac{\pi U(r)}{E}. \quad (108)$$

The integral is independent of ψ_0 , and there is no compensation for the missing yield at angles $\psi < (U(r)/E)^{1/2}$. This is not surprising since the yield of close encounters never exceeds unity in the continuum model (see Eq. (55), for example). But it violates the general rule and it is important to understand the reason for and consequences of this error.

At first, one might argue (as, in fact, people often do) that there should be compensating shoulders on the axial dip, just as for planar dips, because particles incident at angles slightly above the critical angle spend a long time near strings where the transverse velocity is small. But this argument is wrong. In the two-dimensional statistical equilibrium, the probability density is constant in the allowed

area. A qualitative understanding of this result may be obtained from a consideration of water fountains, as mentioned in Ch. 12.

The missing compensation is retrieved when the discrete structure of strings is taken into account, for example in the halfway-plane model. The numerical results in Fig. 9 illustrate how the compensating shoulders depend on the parameter $\rho/d\psi_1$. At low energies, where this parameter is small, the shoulders are localised just outside the dip, and the yield is higher than the random value by several tens of percent. At high energies, on the other hand, where $\rho \gg d\psi_1$, the compensating shoulders are broad and only exceed the random yield by $\sim 1\%$. In comparison with experiments, such a small deviation from the continuum-model prediction is of little importance.

It is straightforward to show that compensation is obtained in the halfway-plane model. For emission from a distance r from a single string, the distribution in transverse energy may be written (see Eq. (79B) and Fig. 7)

$$\Pi_{\text{out}}(E_{\perp}, \mathbf{r}) = \frac{1}{\pi} \int_0 \frac{d^2 \mathbf{p}_{\perp}}{2M_1} \delta \left[\frac{p_{\perp}^2}{2M_1} + U \left(\mathbf{r} + \frac{\mathbf{p}_{\perp} d}{2p} \right) - E_{\perp} \right] , \quad (109A)$$

and the compensation rule may be expressed as an integral over transverse energy,

$$\int_0^{\infty} dE_{\perp} (\Pi_{\text{out}}(E_{\perp}, \mathbf{r}) - 1) = 0 . \quad (109B)$$

With a finite upper limit, the first term gives

$$\int_0^{E_{\perp}} dE'_{\perp} \Pi_{\text{out}}(E'_{\perp}, \mathbf{r}) = \frac{1}{2\pi M_1} \int d^2 \mathbf{p}_{\perp} \left| p_{\perp}^2 < 2M_1 \left(E_{\perp} - U \left(\mathbf{r} - \frac{\mathbf{p}_{\perp} d}{2p} \right) \right) \right. . \quad (109C)$$

For large values of E_{\perp} , the integral is equal to the area of a circle with radius

$$p_{\perp}^* = \left(2M_1 \left[E_{\perp} - U \left(\frac{p_{\perp} d}{2p} \right) \right] \right)^{1/2} , \quad \text{where } \frac{p_{\perp}^2}{2M_1} = E_{\perp} \quad (109D)$$

and we obtain

$$\int_0^{E_{\perp}} dE'_{\perp} [\Pi_{\text{out}}(E'_{\perp}, \mathbf{r}) - 1] \approx -U \left(\frac{d p_{\perp}}{2p} \right) . \quad (109E)$$

With increasing E_{\perp} , the integral converges towards zero. The standard potential in Eq. (23) is seen to decrease rapidly for $r \geq Ca$, and hence most of the compensation is contained within angles $\psi = p_{\perp}/p \sim 2Ca/d$.

Classical shadow behind one atom

The angular compensation of dips by shoulders can be elucidated by a calculation of the intensity distribution behind a single atom which is exposed to a parallel beam of positive particles. In fact, in some of the early work on channeling and blocking, it was attempted to explain the effects on the basis of a two-atom model, in which one atom shields the other from the beam, or blocks the particles emitted from the other atom [Oen 1965]. Although the calculation illustrates some features of the string effect, one should remember the very important difference between the shadows behind one atom and behind a string of atoms. One marked difference was soon discovered in numerical calculations [Andersen 1967], a much stronger sensitivity of the two-atom effect to thermal vibrations. This is illustrated by Fig. 25. Behind the first atom, the dip in flux has hardly been developed, but the combined effects of a few string atoms create a pronounced dip at the centre of the string. More subtle is the different applicability of a classical calculation. As discussed in Sec. 4, the classical picture becomes invalid at high projectile velocities for a single collision, while the interaction with a string of atoms remains classical in this limit.

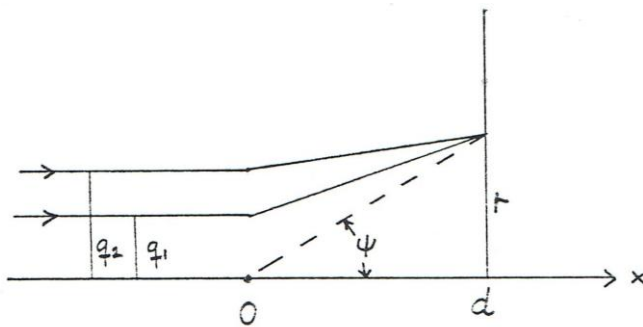


Fig. 42. Deflection by single atom.

Fig. 42 shows a beam of positive particles moving in the x -direction towards a scattering centre at the origin. The intensity distribution, $I(r)$, on a screen at $x = d$ can be calculated if we know the connection between the impact parameter q and the distance r from the x -axis at $x = d$. This distribution gives the normalised probability for a close encounter with an atom placed at (d, r) as a function of the angle ψ between the beam and the line connecting the two atoms. (Note the distorted scale; we only consider very small angles ψ .)

We first consider pure Coulomb scattering, in a potential $V(R) = Z_1 Z_2 e^2 / R$, and we obtain for small angles of deflection (Eqs. (114) and (118))

$$\begin{aligned} r &= q + d \frac{b}{q} \\ b &= \frac{Z_1 Z_2 e^2}{E} \end{aligned} \tag{110}$$

The connection between q and r is illustrated in Fig. 43.

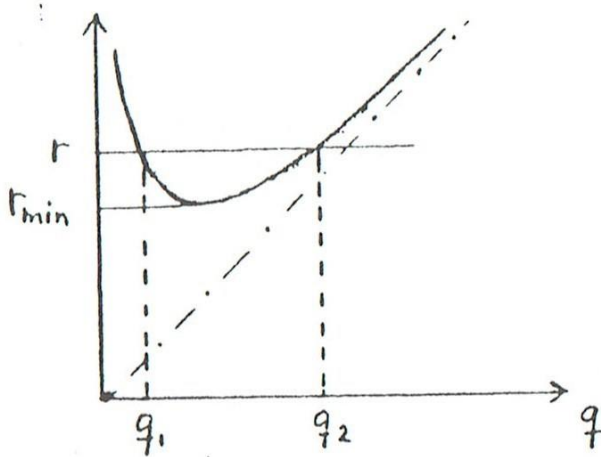


Fig. 43. Distance r from axis on screen behind atom, as a function of the impact parameter q .

A minimum value of r is found for $q = (bd)^{1/2}$, and thus the intensity is zero in the region $0 \leq r < r_{\min} = 2(bd)^{1/2}$. Outside this shadow, a given value of r corresponds to two impact parameters q_1 and q_2 , where $q_1 < (bd)^{1/2}$ and $q_2 > (bd)^{1/2}$. For a uniform intensity of one particle per unit area, we find (with ' d ' here indicating differentials)

$$I(r)\pi d(r^2) = \pi d(q_2^2 - q_1^2) = \pi d\{r(r^2 - r_{\min}^2)^{1/2}\}. \quad (111)$$

Changing the variable to $\psi = r/d$ to obtain the close-encounter probability $\Pi_{\text{in}}(\psi)$ with an atom at (d, r) and introducing the characteristic angle $\psi_1 = (2b/d)^{1/2}$, (Eq. (29)), we may write this result as

$$\Pi_{\text{in}}(\psi) = \begin{cases} 0 & \text{for } \psi < \sqrt{2}\psi_1 \\ \frac{1}{2}[(1 - 2\psi_1^2/\psi^2)^{1/2} + (1 - 2\psi_1^2/\psi^2)^{-1/2}] & \text{for } \psi > \sqrt{2}\psi_1 \end{cases}. \quad (112)$$

An infinitely high shoulder is observed just outside the shadow but the extra intensity quickly drops with increasing ψ . The enhancement is due to a focussing of trajectories near the minimum value of r where $dr/dq = 0$. Qualitatively, the explanation is the same for shoulders on dips evaluated in the halfway-plane model. For incidence angles just above the critical angle, individual atoms focus the intensity on their neighbours. The effect will be strongly smeared out if the fluctuations in atomic positions $\sim \rho$ are comparable to or larger than the distance r_{\min} defined above, i.e., $\rho > \sqrt{2}d\psi_1$, which is just our usual condition for application of the continuum model, Eq. (34).

Let us consider the question whether the compensation is complete in the limit $r \rightarrow \infty$ for our simple two-atom model. For this to be the case, we must have

$$\pi r^2 - \int_0^r I(r')2\pi r' dr' = \pi r^2 - \pi(q_2^2 - q_1^2) \rightarrow 0 \quad \text{for } r \rightarrow \infty. \quad (113A)$$

For Coulomb scattering, the difference in Eq. (113A) does not tend to zero but to the constant value $\pi r_{\min}^2/2$ according to Eq. (111). This means that only half the intensity missing in the shadow is compensated for by the excess yield in the shoulder. This may also be seen directly from the scattering law in Eq. (110). The flux is being pushed out by the scattering, and the number of particles pushed outside a radius r is for large r given approximately by

$$2\pi r \frac{bd}{r} = \frac{\pi r_{\min}^2}{2} \quad (113B)$$

It is clear from this argument that the compensation is complete for scattering in a screened potential, where the scattering angle decreases more rapidly than one divided by the impact parameter. For the standard potential in Eq. (22), the Coulomb deflection angle is multiplied by a factor $(1+q^2/(Ca)^2)^{-1}$, and the missing compensation is found at angles $\psi \sim Ca/d$. This is very similar to the result obtained in the half-way-plane model, (Eq. (109E)).

17. SCATTERING OF RANDOM AND ALIGNED BEAM

The multiple Coulomb scattering, which in a random medium gradually increases the divergence of a beam, is for channeled particles replaced by highly correlated scattering by atoms on strings or planes, with conservation of transverse energy. However, fluctuations of deflections by atoms, due to thermal displacements and scattering by electrons, lead to a gradual change in transverse energy of the projectiles. In this chapter, we derive estimates of the thermal and electronic scattering. For high defect concentrations, scattering by defects is important, but we shall treat only the case of a perfect crystal structure. In the following chapter, we shall discuss how the gradual change in transverse energy can be included in calculations of channeling dips.

Random Multiple Scattering

The basic phenomenon is scattering in a Coulomb potential, Rutherford scattering. In the following, the velocity v of the projectile with charge Z_1e and mass M_1 is assumed to be nonrelativistic, but relativistic corrections to the results are indicated. The target atom with charge Z_2e and mass M_2 is assumed to be at rest. If Bohr's parameter κ (Eq. (3)) is large, the classical impact parameter q is well defined, and the scattering angle θ in the CM system is given by

$$\tan \frac{\theta}{2} = \frac{b_0}{2q}, \quad b_0 = \frac{2Z_1Z_2e^2}{M_0v^2} \quad (114)$$

where M_0 is the reduced mass, $M_0 = M_1M_2/(M_1+M_2)$. From this relation, we can easily derive the differential cross section,

$$d\sigma = \pi d(q^2) = \frac{\pi b_0^2}{4} d\left(\cot^2 \frac{\theta}{2}\right) = \frac{\pi b_0^2}{4} \sin^{-4} \frac{\theta}{2} d\left(\sin^2 \frac{\theta}{2}\right), \quad (115)$$

where we have ignored a minus sign. We may introduce the energy transfer T ,

$$T = T_{\max} \sin^2 \frac{\theta}{2}, \quad T_{\max} = \frac{4M_1M_2}{(M_1+M_2)^2} E, \quad (116)$$

to obtain the cross section in a form which is often referred to as the Thomson cross section,

$$d\sigma = \frac{2\pi Z_1^2 Z_2^2 e^4}{M_2 v^2} \frac{dT}{T^2} . \quad (117)$$

For small-angle scattering T is proportional to the square of the deflection angle φ in the laboratory,

$$\begin{aligned} \tan \varphi &= \frac{M_2 \sin \theta}{M_1 + M_2 \cos \theta} \cong \frac{M_2}{M_1 + M_2} \theta \\ T &\cong \frac{M_1}{M_2} E \varphi^2 , \theta \ll 1 . \end{aligned} \quad (118)$$

Nuclear collisions: If the deflections are uncorrelated, they add in quadrature, and the average square deflection angle (in the lab frame) is proportional to the mean energy loss from ‘nuclear’ collisions (deflections with momentum transfer to atoms),

$$\langle \delta\Omega^2 \rangle_n \cong \frac{M_2 \langle \delta E \rangle_n}{M_1 E} . \quad (119)$$

The energy loss over a path length δz we can calculate from the Thomson cross section in Eq. (117)

$$\langle \delta E \rangle_n = N \delta z \int d\sigma T = \frac{4\pi Z_1^2 Z_2^2 e^4}{M_2 v^2} N \delta z L_n , \quad (120)$$

where the logarithm L_n is given by

$$L_n = \frac{1}{2} \log \left(\frac{T_{\max}}{T_{\min}} \right) . \quad (121)$$

The upper limit of T is determined by the kinetics of the collision, whereas the lower limit derives from screening of the atomic Coulomb field at distances of the order of the Thomas-Fermi radius a . For this reason, one usually expresses the logarithm in terms of impact parameters q . Combining Eqs. (114) and (116), we obtain

$$T \propto \sin^2 \frac{\theta}{2} = \left(1 + \cot^2 \frac{\theta}{2} \right)^{-1} \propto \left(q^2 + \frac{b_0^2}{4} \right)^{-1} \quad (122)$$

and hence the logarithm may be written as

$$L_n = \log \left(\frac{q_{\max}}{q_{\min}} \right) , \quad (123)$$

with $q_{\min} = b_0/2$ and $q_{\max} \sim a = 0.8853 Z_2^{-1/3} a_0$. The lower limit comes from the constant term in the last expression in Eq. (122) and in reality corresponds to $q = 0$.

From numerical evaluation of L_n with the Thomas-Fermi screening function, we obtain

$$L_n = \log\left(\frac{1.29a}{b_0}\right) . \quad (123A)$$

With the standard potential, L_n may be calculated analytically. The scattering law is for small deflection angles modified to

$$\theta \approx \frac{b_0}{q} \left(1 + \frac{q^2}{(Ca)^2}\right)^{-1} \quad (123B)$$

and the logarithm becomes

$$L_n = \int_{b_0^2/4}^{\infty} \frac{d(q^2)}{2q^2} \left(1 + \frac{q^2}{(Ca)^2}\right)^{-2} . \quad (123C)$$

Introducing the variable $\xi = q^2/(Ca)^2$, we may express the integral as

$$L_n = \frac{1}{2} [\log \xi - \log(1 + \xi)^{-1} + (1 + \xi)^{-1}] \Big|_{\xi = \frac{b_0^2}{4(Ca)^2}}^{\xi \rightarrow \infty} \cong \log\left(2C \frac{a}{b_0}\right) - \frac{1}{2} . \quad (123D)$$

Agreement with Eq. (123A) is obtained for $C \sim 1.06$ which is considerably smaller than the normal value $C = \sqrt{3}$. However, with $C \sim 1$, the Thomas-Fermi screening is much better reproduced at the small distances, $r < a/2$, which dominate the multiple scattering.

At higher velocities where Bohr's parameter κ becomes small the scattering may be treated by first-order Born approximation. The Rutherford cross section is still valid but there is no one-to-one relation between impact parameter and energy transfer. We may instead introduce the momentum transfer, Δp , as variable,

$$\Delta p = 2M_0 v \sin \frac{\theta}{2} , \quad T = \frac{(\Delta p)^2}{2M_2} , \quad (124)$$

and write the logarithm as

$$L_n = \log\left(\frac{\Delta p_{\max}}{\Delta p_{\min}}\right) . \quad (125)$$

The maximum value is again determined by kinematics and the minimum value by screening,

$$\Delta p_{\max} = 2M_0 v , \quad \Delta p_{\min} = \frac{\hbar}{\xi a} , \quad (126)$$

where ξ is a constant of the order of unity. With the exponentially screened Coulomb potential, $V(R) = (Z_1 Z_2 e^4 / R) \exp(-R/a)$, the cross section, which in the Born approximation is proportional to the square of the Fourier transform of V , has a simple form,

$$d\sigma \propto \frac{d(\Delta p^2)}{\left[\Delta p^2 + \left(\frac{\hbar}{a}\right)^2\right]^2}, \quad (127)$$

and for $2M_0v \gg \hbar/a$, Eq. (125) is obtained with $\xi = 1/\sqrt{e}$ in Eq. (126).

Since the maximum momentum transfer in Eq. (126) is the same in classical and quantum mechanics, the difference between the logarithms obtained in the two cases is associated with the lower cut-off in momentum in Eq. (126). Qualitatively, small momenta correspond to large distances, and one might therefore be tempted to associate the difference with scattering at large impact parameters. On the other hand, the logarithm obtained from Eqs. (125) and (126) may be written as ($\xi = 1$)

$$L_n \cong \log\left(\frac{2a}{\tilde{\lambda}_0}\right), \quad (127A)$$

where $\tilde{\lambda}_0$ is the reduced wavelength of the motion in the centre-of-mass system, $\tilde{\lambda}_0 = \hbar/M_0v$. Compared to the classical results, the minimum impact parameter in Eq. (123) has here been changed from $b_0/2$ to $\tilde{\lambda}_0/2$, and this change is associated with the scattering at small impact parameters! From the theory of energy loss, we know this latter picture to be correct. The average energy loss is the same at large impact parameters in the classical and quantal descriptions, and the effective upper cut-off q_{\max} is the same. The difference at small q may be derived from a description in terms of angular momentum in the collision, where the integral over T in Eq. (120) is expressed as a sum over angular momenta. In contrast to q , the angular momentum is a well-defined quantity also in a quantum description, $L = l\hbar$. Since angular momentum $L = \hbar$ corresponds to a classical impact parameter $q = \tilde{\lambda}_0$, it is perhaps not surprising that $q_{\min} = b_0/2$ is replaced by $q_{\min} = \tilde{\lambda}_0/2$ when $\kappa \equiv b_0/\tilde{\lambda}_0 < 1$. The question whether the difference between the classical and quantal results is associated with large or small impact parameters may appear to be of academic interest, only, but it becomes important when we consider the multiple scattering of channeled particles, for which the close collisions with nuclei are forbidden.

The average square deflection angle $\langle \delta\Omega^2 \rangle_n$ characterises the distribution in angle uniquely only if it is Gaussian. Rutherford scattering may qualitatively be divided into very frequent small deflections and rare events of scattering through a large angle, and the resulting angular distribution may be characterised as a Gaussian with a tail. Often the important quantity is the width $\delta\Omega_G$ of the Gaussian part, and in the evaluation of this angle, the large momentum transfers must be excluded in Eq. (120). According to Eq. (118) this corresponds to an upper cut-off at a scattering angle $\theta_{\max} \sim (M_1+M_2/M_2)\delta\Omega_G$. The maximum momentum transfer in Eq. (125) is reduced to $M_0v\theta_{\max}$, leading to multiplication by a factor $\theta_{\max}/2$ in the argument of the logarithm in Eq. (125),

$$\Delta p_{\max} = \theta_{\max}M_0v, \quad \Delta p_{\min} = \frac{\hbar}{\xi a} \quad (126A)$$

Note that already in the relation in Eq. (118) we have assumed all important deflections to be small. As shown in Ch. 3, we may then also avoid transformations

to the centre-of-mass system and evaluate all quantities as if the target atoms were infinitely heavy. In the following we shall therefore often omit the index on b and $\hat{\lambda}$. The resulting formula applies also for relativistic particles if the mass M_1 is replaced by the relativistic mass $M_1\gamma$ in the expression for $\hat{\lambda}_0$ as well as in the pre-factor in Eqs. (119) and (120).

For scattering in a thin amorphous surface layer the tail in the angular distribution may be important. The cross section in Eqs. (117) and (118) may be written as

$$d\sigma = \frac{\pi}{4} d^2 \psi_1^4 \frac{d\varphi^2}{\varphi^4}$$

and hence the probability for scattering to angles larger than ψ_1 in a layer of thickness δz is given by

$$P(\varphi > \psi_1) = \frac{\pi}{4} d^2 N \delta z \psi_1^2.$$

This is a rough estimate of the increase in minimum yield just behind the surface peak (Fig. 20). As a numerical example take 30 Å Si and <110> channeling of 1 MeV He. With $d = 3.84$ Å and $N = 0.05$ Å⁻³ the increase is 0.7%. Of course the backscattering in the amorphous layer also gives a large contribution to the surface peak. To avoid such effects in channeling experiments special precaution is often taken to remove or minimize natural oxide layers on crystals.

Electronic collisions: Without excitation of atoms, the electrons just screen the nuclear Coulomb field but momentum transfers to electrons in connection with electronic excitation contribute to multiple scattering. Since normally the momentum transfer in the excitation process is not correlated (in direction) with the simultaneous deflection in the atomic field, we may add the angles in quadrature and evaluate independently the average square deflection angles from nuclear and electronic scattering (in analogy to the normal treatment of energy loss). The connection to the average energy loss is similar to Eq. (119) but at high velocities, about half the energy loss is due to distant (resonant) collisions, with little momentum transfer (equipartition rule). Replacing M_2 by m_0 and multiplying by $\frac{1}{2}$ we then obtain

$$\langle \delta\Omega^2 \rangle_e \cong \frac{m_0}{2M_1} \frac{\langle \delta E \rangle_e}{E}. \quad (128)$$

The value of Bohr's parameter κ is smaller by a factor Z_2 compared to nuclear collisions, and we shall assume the velocity to be high enough for quantum perturbation theory to apply. The energy loss is in this limit given by the Bethe-Bloch formula,

$$\langle \delta E \rangle_e \cong \frac{4\pi Z_1^2 e^4}{m_0 v^2} N Z_2 \delta z L_e, \quad L_e = \log\left(\frac{2mv^2}{I}\right), \quad (129)$$

where NZ_2 is the electron density and I the mean ionisation potential, which is roughly proportional to Z_2 , $I \sim Z_2 \cdot 10$ eV.

The theory of energy loss of swift charged particles penetrating matter is subtle and contains

many pitfalls. An example is the tempting application of the Thomson cross section in Eq. (117) to derive a formula for electronic excitations analogous to Eq. (121). The maximum energy transfer is $2m_0v^2$ and the minimum I . This leads to Eq. (129) multiplied by a factor $\frac{1}{2}$. The problem is that one has then omitted the distant, resonant collisions with an average energy transfer smaller than I , which contribute half the stopping!

However, for estimation of the electronic multiple scattering for channeled particles, the connection to the energy loss is not very useful. The resonant collisions are non-local, and this complicates the evaluation of energy loss for channeled particles. In contrast, the multiple scattering is dominated by close collisions and hence determined by the local electron density traversed by the particle. The evaluation may be based on an approximate formula for scattering in an electron gas of density n . One obtains a result which may be expressed by Eqs. (128) and (129) but with NZ_2 replaced by n and a logarithm given by

$$L_e \rightarrow \log\left(\frac{2mv^2}{\hbar\omega_0}\right) - 1, \quad \omega_0^2 = \frac{4\pi ne^2}{m_0} \quad (130)$$

The correction -1 to the logarithm accounts mainly for the breakdown of the approximation $\theta \ll 1$ in Eq. (118) at large momentum transfers. The upper limit in Eq. (126) corresponds to scattering through 180° in the CM system, which involves only longitudinal momentum transfer. For heavy projectiles, $M_1 \gg m_0$, the scattering angle φ in the laboratory is, on the other hand, always very small, and all deflections contribute to the Gaussian part of the angular distribution.

For relativistic particles, the mass M_1 in Eq. (128) should again be replaced by the relativistic mass $M_{1\gamma}$. In addition, the logarithm L_e should be corrected by

$$\Delta L_e = \log(\gamma^2) - \beta, \quad \beta = \frac{v}{c}, \quad \gamma = (1 - \beta^2)^{-1/2}. \quad (130A)$$

The correction consists of equal contributions from close and distant collisions, so application of the equipartition rule in Eq. (128) is still valid.

The relative magnitude of the nuclear and electronic contributions to the multiple scattering is essentially determined by the atomic number Z_2 ,

$$\frac{\langle \delta\Omega^2 \rangle_n}{\langle \delta\Omega^2 \rangle_e} \cong 2Z_2 \frac{L_n}{L_e}. \quad (131)$$

Since L_n is usually somewhat larger than L_e and $Z_2 \gg 1$, the multiple scattering is normally dominated by the nuclear contribution. The reason is that the deflections by the Z_2 elementary charges in the nucleus add linearly, while the uncorrelated deflections by the Z_2 atomic electrons add in quadrature, on the average. As noted in Ch. 10, there is a close analogy to the doughnut scattering by strings of atoms. Here the correlation of deflections by atoms may lead to a strong increase in the multiple scattering.

Multiple Scattering of Channeled Particles

For particles moving through a crystal at a small angle to an axis or a plane, the atomic deflections are correlated, and this modifies the multiple scattering. The azimuthal scattering around the axis, ‘doughnut’ scattering, is very strong, and hence the mean-square deflection angle can be much larger than for transmission through an amorphous foil (Fig. 15). Here we shall consider only the slow change in polar angle, i.e., the change in transverse energy. The following is based mainly on our own papers, developing the earlier work in [Lindhard 1965]. Many groups have contributed over the years, e.g. [Beloshitsky *et al.* 1972, 1973].

The average change in E_{\perp} due to a number of uncorrelated momentum transfers $\delta\bar{p}_i$ is given by

$$\langle \delta E_{\perp} \rangle = \sum_i \frac{\langle (\delta \mathbf{p}_i)^2 \rangle}{2M_1} = E \sum_i \langle (\delta \varphi_i)^2 \rangle. \quad (132)$$

For nuclear scattering, the momentum transfers $\delta\mathbf{p}_i$ are due to the deviation of the real crystal potential from the continuum axial or planar potential,

$$\langle \delta E_{\perp} \rangle = \sum_i \left\langle \frac{(\mathbf{p}_i + \Delta\mathbf{p}_i + \delta\mathbf{p}_i)^2}{2M_1} - \frac{(\mathbf{p}_i + \Delta\mathbf{p}_i)^2}{2M_1} \right\rangle = \sum_i \frac{\langle (\delta\bar{p}_i)^2 \rangle}{2M_1}, \quad (132A)$$

where $\Delta\mathbf{p}_i$ is the average momentum transfer in the i 'th collision and \mathbf{p}_i is the momentum before the collision.

In Eq. (132A) we have ignored the change in potential energy at the $(i+1)$ 'th halfway plane due to the fluctuation $\delta\mathbf{p}_i$. The displacement is given by $\delta\mathbf{r}_{i+1} = (\frac{d}{2M_1 v})\delta\mathbf{p}_i$ and this leads to an average deviation of the potential energy given by

$$\langle \delta U_{i+1} \rangle \cong \frac{d^2 U''(r_{i+1}) \langle \delta p_i^2 \rangle}{8E \cdot 2M_1}. \quad (132B)$$

As discussed below, this is a small correction to Eq. (132A) for $r > d\psi_1$ if the static potential is applied. At distances $r < \rho$, the thermally averaged potential, which in principle should be used in Eq. (132B), is slowly varying, and hence we may ignore the correction for all distances r_{i+1} in the high-energy limit, $\rho > d\psi_1$.

For electronic scattering, we may use the result in Eqs. (128)–(130) for an electron gas to estimate the magnitude of $\langle \delta E_{\perp} \rangle$ as a function of E_{\perp} . In the axial case, we obtain

$$\frac{\langle \delta E_{\perp} \rangle}{\delta z} \cong \frac{\pi Z_1^2 e^4}{E} \frac{1}{A(E_{\perp})} \int_{A(E_{\perp})} d^2\mathbf{r} \frac{1}{d} \int_0^d dz n(\mathbf{r}, z) \left[\log \left(\frac{2m_0 v^2}{\hbar\omega_0(\mathbf{r}, z)} \right) - 1 \right]. \quad (133)$$

If the fairly slow variation of the logarithm is ignored, the right-hand side of Eq. (133) is proportional to the electron density ‘seen’ by the channeled particle, as given by Eq. (63) for the standard potential. With a constant electron density, n_e , and hence a constant value of the square parenthesis, one obtains

$$\frac{\langle \delta E_{\perp} \rangle}{\delta z} \cong \frac{\pi Z_1^2 e^4}{E} n_e [L_e - 1]. \quad (133A)$$

The formula analogous to Eq. (133) for the planar case is more complicated because the equilibrium spatial density is non-uniform,

$$\frac{\langle \delta E_{\perp} \rangle_e}{\delta z} \cong \frac{\pi Z_1^2 e^4}{2E} \frac{1}{L_y} \int_0^{L_y} dy \frac{1}{L_z} \int_0^{L_z} dz \int dx \frac{K(E_{\perp})}{[E_{\perp} - V(x)]^2} n(x, y, z) \left[\log \left(\frac{2m_0 v^2}{\hbar \omega_0(x, y, z)} \right) - 1 \right], \quad (134)$$

where the y - and z -integrations are over a lattice period and the x -integration over the allowed region with $E_{\perp} > V(x)$. The function $K(E_{\perp})$ is defined in Eq. (91). For constant electron density one obtains the simple expression in Eq. (133A), divided by two due to the reduction to one dimension,

$$\frac{\langle \delta E_{\perp} \rangle}{\delta z} \cong \frac{\pi Z_1^2 e^4}{2E} n_e [L_e - 1]. \quad (134A)$$

The electron densities in Eqs. (133) and (134) may in principle be derived from the crystal potential by application of the Poisson equation, given in two dimensions by Eq. (57). Far from atoms, the potential and the electron density are rather uncertain in many materials but simple estimates corresponding to a uniform distribution of the outer, delocalised atomic electrons may often suffice.

Axial channeling: An analysis of the accuracy of transverse-energy conservation in a static, perfect lattice was carried out in [Lindhard 1965] within the half-way-plane description. We shall instead illustrate the accuracy by a computer simulation of a single collision with a perfect string (Fig. *). The conservation is seen to be extremely accurate for small E_{\perp} , but when the minimum distance of approach in the collision becomes small, $r_{\min} < d\psi_1/2$, there is a sudden breakdown. This is in agreement with the condition derived by Lindhard,

$$E > \frac{d^2}{8} U''(r_{\min}), \quad (135)$$

which for $d\psi_1 \ll Ca$ is equivalent to $r_{\min} > d\psi_1/\sqrt{8}$. Note also that the scattering angle in a single collision at impact parameter $d\psi_1/2$ is $\varphi \sim \psi_1$ according to Eqs. (5) and (7).

In Fig. ** are shown the results of simulations including vibrations of the string atoms. Clearly, the non-conservation of E_{\perp} due to the discrete structure of the perfect string may be ignored compared to the fluctuations caused by vibrations. In general, we may expect this to be the case in the high- energy region, defined by the condition in Eq. (34), $\rho > d\psi_1$, where the critical angle for hitting a vibrating string atom is smaller than the critical angle for a perfect string.

As a first estimate of the thermal scattering, we may as for electronic scattering

assume the multiple scattering to be a local process and use a formula analogous to the overlap estimate in Eq. (133),

$$\frac{\langle \delta E_{\perp} \rangle_n}{\delta z} \cong E \frac{d}{dz} \langle \delta \Omega^2 \rangle_n \Pi_{\text{in}}(E_{\perp}), \quad (136)$$

where $\langle \delta \Omega^2 \rangle_n$ is given by Eqs. (119), (120). In the evaluation of L_n it is reasonable to exclude scattering angles larger than $\varphi \sim \psi_1 = (2b/d)^{1/2}$ if we want to estimate the width of the Gaussian part of the distribution in angle after the string collision. Replacing the maximum momentum transfer in Eq. (125) by $M_1 v \psi_1$ corresponds to multiplication by $\psi_1 M_1 / M_0$. According to Eq. (123D) with $C \sim 1.1$, this leads to

$$L_n \cong \log \left(\frac{\sqrt{2}C}{\sqrt{e}} \frac{a}{\sqrt{bd}} \right) \sim \log \left(\frac{\sqrt{2}a}{d\psi_1} \right), \quad \kappa > 1. \quad (137)$$

For $\kappa < 1$, the quantum-perturbation result, given by Eqs. (125), (126) should be applied. This leads to

$$L_n \cong \log \left(\frac{\xi a}{\lambda} \psi_1 \right) = \log \left(\frac{\sqrt{2}a}{d\psi_1} \kappa \right), \quad \kappa < 1, \quad (138)$$

if we adjust the numerical constant ξ to give agreement between the two formulas in Eqs. (137) and (138) for $\kappa = 1$ ($\xi = 1/\sqrt{2}$).

As an example, we consider 1-MeV protons channeled along a $\langle 110 \rangle$ axis in Si. The important parameters are then $\kappa = 4.4$, $a = 0.194 \text{ \AA}$, $b = 2.01 \times 10^{-4} \text{ \AA}$, and $d = 3.84 \text{ \AA}$. This leads to a value of $L_n = 1.95$ according to Eq. (137). Without the cut-off at $\varphi \sim \psi_1$, we obtain from Eq. (123D) $L_n = 7.1$. The smaller value of L_n is not very large and hence not very accurate but fortunately, as we shall see in the following chapter, the results of dechanneling calculations are not very sensitive to this value. Nevertheless, it is important to include the cut-off which reduces L_n by more than a factor of three in this case.

In both the classical and the quantal estimates of thermal scattering, we have ignored the fact that the fluctuations in ψ should be evaluated from the difference between the scattering by thermally displaced atoms and the governing by the thermally averaged string potential. For large momentum transfers, this is not important, but it may affect the lower limit in the logarithm associated with the soft collisions. It is straightforward to include this modification in a quantum perturbation calculation. The cross section is proportional to the square of a Fourier component of the scattering potential,

$$d\sigma(\mathbf{k}) \propto \left(\left| \int e^{-i\mathbf{k}\cdot\mathbf{r}} (U(\mathbf{r} - \mathbf{r}_a) - U_T(\mathbf{r})) d^2\mathbf{r} \right|^2 \right)_T, \quad (138A)$$

where $\Delta\mathbf{p} = \hbar\mathbf{k}$ is the momentum transfer, assumed to be perpendicular to the axis, and \mathbf{r}_a is the transverse position of a displaced atom. As before, we have indicated a thermal average by a subscript T . The average of an exponential over a Gaussian distribution of displacements, usually called a Debye-Waller factor, is easily evaluated,

$$(e^{-i\mathbf{k}\cdot\mathbf{r}_a})_T = \exp(-k^2 \rho_1^2 / 2), \quad (138B)$$

where ρ_1 is the rms displacement in one dimension. Thermal averaging of the potential corresponds to multiplication of the Fourier components $U(\mathbf{k})$ by this Debye-Waller factor, and we obtain

$$d\sigma(\mathbf{k}) \propto |U(\mathbf{k})|^2 (1 - \exp(-k^2 \rho_1^2)) . \quad (138C)$$

The subtraction of the thermally averaged potential in Eq. (138A) thus leads to a lower cut-off in momentum transfers at

$$\Delta p_{\min} \cong \hbar/\rho_1 . \quad (138D)$$

However, this value is usually not much larger than in Eq. (126), with $\xi = 1/\sqrt{2}$.

The predictions corresponding to the estimate in Eq. (136) are also shown in Fig. ** and they are seen to be in reasonable accord with the simulation for large angles of incidence. However, for decreasing ψ , the scattering is predicted to fall off much too rapidly. The overlap estimate in Eq. (136) must therefore be supplemented with an estimate of the contribution from distant collisions for channeled particles with a very small probability of close collisions.

In a collision with an atom at position (\mathbf{r}_a, z_a) the scattering angle is given by (Eqs. (4), (5), (6))

$$\boldsymbol{\varphi} = -\frac{d}{2E} \nabla_{\mathbf{r}} U(\mathbf{r} - \mathbf{r}_a) \equiv \frac{d}{2E} \mathbf{F}(\mathbf{r} - \mathbf{r}_a) , \quad (139)$$

where we have introduced the force \mathbf{F} in the continuum potential. The fluctuations of this force due to fluctuations in atomic positions lead on the average to an increase in E_{\perp} , given by Eq. (132),

$$\langle \delta E_{\perp} \rangle = nE \left(\frac{d}{2E} \right)^2 \langle (\delta \mathbf{F})^2 \rangle , \quad (140)$$

where we have averaged over the fluctuations in n collisions and used $n = \delta z/d$. For particles in statistical equilibrium at a transverse energy E_{\perp} , the average increase in E_{\perp} per path length is then given by

$$\frac{d}{dz} \langle E_{\perp} \rangle = \frac{d}{4E} \frac{1}{A(E_{\perp})} \int_{A(E_{\perp})} d^2 \mathbf{r} (\delta \mathbf{F})_T^2 , \quad (141)$$

where as usual the average over thermal displacements is indicated by a subscript T . To first order in the displacement \mathbf{r}_a the force fluctuation is given by

$$\delta \mathbf{F} = (x_a U''(r), \frac{y_a}{r} U'(r)) , \quad (142)$$

where x_a, y_a are the displacements parallel and perpendicular to \mathbf{r} , respectively. The thermal average of the square becomes

$$(\delta F)_T^2 = \frac{1}{2}\rho^2 \left[(U''(r))^2 + \frac{1}{r^2} (U'(r))^2 \right], \quad (143)$$

where $(x_a^2)_T = (y_a^2)_T = \rho^2/2$ is assumed. If the standard potential is used, a somewhat lengthy but straightforward evaluation of the integral in Eq. (141) leads to the following expression [Lindhard 1965],

$$\frac{d}{dz} \langle E_\perp \rangle = \frac{\pi}{4} N(d\psi_1)^2 E\psi_1^2 \frac{\rho^2}{(ca)^2} \left(\left(\frac{ca}{r_m} \right)^2 + \frac{5}{3} \right) \left(\left(\frac{r_m}{ca} \right)^2 + 1 \right)^{-3}, \quad (144)$$

where r_m is the minimum distance of approach, $U(r_m) = E_\perp$. This expression may also be written as a function of transverse energy by application of the relation

$$E_\perp = \frac{1}{2} E\psi_1^2 \log\left(\frac{(ca)^2}{r_m^2} + 1\right) \text{ and the reduced unit of transverse energy, } \varepsilon \equiv 2E_\perp/E\psi_1^2,$$

$$\frac{d}{dz} \langle E_\perp \rangle = \frac{\pi}{4} N(d\psi_1)^2 E\psi_1^2 \frac{\rho^2}{(ca)^2} \left(\exp(\varepsilon) + \frac{2}{3} \right) (1 - \exp(-\varepsilon))^3. \quad (144A)$$

Note, however, that if a more accurate potential is used for the channeling trajectory (e.g. thermally averaged Doyle-Turner [Nielsen 1987]) one should use Eq. (144) with r_m determined with this potential.

We have in this derivation ignored the fact that the motion on the average is governed by the thermally averaged potential U_T and not by the static potential. However, for $r > \rho$, the two potentials are not very different, and it is easily seen that taking the average deflection as a reference in Eq. (142) instead of the deflection by an atom at $r_a = 0$ leads to corrections of fourth order in ρ , only.

In Fig. ** a prediction based on Eq. (143) is also shown and it reproduces the results of the simulation fairly well at small transverse energies, where the overlap estimate is much too low. In an intermediate region, the simulation results lie above both of the two predictions but their sum appears to be a reasonable overall estimate. In the evaluation of the curve corresponding to a first-order expansion in ρ/r , which becomes invalid at small r and even diverges for $r \rightarrow 0$, the expression in Eq. (143) was replaced by its value at $r = \sqrt{2}\rho$ for distances $r < \sqrt{2}\rho$.

As discussed in Ch. 5, a more accurate approximation to the atomic potential is obtained with the Doyle-Turner fit in Eq. (16), in particular for light elements. This approximation becomes invalid at small distances and should therefore not be used to evaluate the random multiple scattering which is dominated by close collisions. However, the expression in Eq. (143) is used only at larger distances, and the Doyle-Turner potential should therefore be applicable. It is straightforward to evaluate the average corresponding to Eq. (144),

$$\begin{aligned}
\frac{d}{dz} \langle E_{\perp} \rangle &\cong \frac{4\pi}{E} (e^2 a_0)^2 \rho^2 N \sum_{i,j}^4 \frac{a_i a_j}{(B_i + B_j)^3} \\
&\times \left[4 + r_m^2 \left(\frac{1}{B_i} + \frac{1}{B_j} \right) \left(2 - \frac{B_i}{B_j} - \frac{B_j}{B_i} \right) + 2r_m^4 \left(\frac{1}{B_i} + \frac{1}{B_j} \right)^2 \right] \\
&\times \exp \left(-r_m^2 \left(\frac{1}{B_i} + \frac{1}{B_j} \right) \right),
\end{aligned} \tag{145}$$

where we have extended the integration to $r \rightarrow \infty$ in the statistical average over $A(E_{\perp})$. However, the approximation cannot be expected to be as accurate for the force fluctuations as for the potential since small oscillatory deviations will be strongly enhanced by the repeated differentiations. Even if a Doyle-Turner potential is used to describe the average motion, it may be preferable to use the smooth standard potential to describe the fluctuations, according to Eq. (144).

At this point, we should also note that the assumption in Eq. (132) of independent force fluctuations in consecutive collisions is not exactly fulfilled since the thermal displacements of nearby atoms are correlated. If neighbouring string atoms were vibrating pairwise together, the average increase in E_{\perp} would double for fixed ρ and more generally, we may estimate the increase due to correlation by the replacement,

$$\rho^2 = \langle r_a^2 \rangle \rightarrow \sum_j \langle \mathbf{r}_a^0 \cdot \mathbf{r}_a^j \rangle \equiv \rho^2 \sum_j \beta_j,$$

where j is an index of the atoms on a string, $j = 0, \pm 1, \dots$. The magnitude of the correlation coefficients β_j was discussed in Ch. 7. For a close-packed string, the enhancement of $d\langle E_{\perp} \rangle/dz$ may be as large as a factor of two.

For random multiple scattering, we made a distinction between classical and quantal regimes, corresponding to $\kappa > 1$ and $\kappa < 1$, respectively, and slightly different formulas were obtained in the two limits. It is natural to ask whether a similar distinction should be made for the influence of force fluctuations for channeled particles. However, according to our earlier discussion, the difference between the logarithms in Eq. (123) and Eqs. (125), (126) is associated with very close collisions, and these are eliminated for channeled particles. We may therefore expect the formula in Eq. (144) or (145) to apply also for $\kappa < 1$ provided the motion is restricted to the classically allowed area in the transverse plane ($r > r_m$). As mentioned in Ch. 2, this is always a good approximation for particles which are much heavier than an electron. In fact, as shown below, it is straightforward to demonstrate that a result equivalent to the classical expression is obtained from a quantum perturbation calculation, as we shall indicate in the following (first shown by [Ryabov 1975], as mentioned in [Andersen *et al.* 1988, Ref. 11]).

In a quantum treatment, the transverse motion of a channeled particle with transverse energy E_{\perp}^n is described by a wave function $\varphi_n(\mathbf{r})$ which is a solution of a Schrödinger equation,

$$\left(\frac{\mathbf{p}_{\perp}^2}{2M_1} + U_T(\mathbf{r}) \right) \varphi_n(\mathbf{r}) = E_{\perp} \varphi_n(\mathbf{r}), \tag{145A}$$

where the transverse momentum is an operator, $\mathbf{p}_{\perp} = -i\hbar\nabla$. For relativistic particles, M_1 should be replaced by the relativistic mass.

Transitions between eigenstates φ_n are induced by the fluctuations in the potential, $V-V_T$, and for small scattering angles the transition probability is proportional to the square of a matrix element of the integrated potential,

$$P_{n,0} \propto |\langle \varphi_n | U(\mathbf{r} - \mathbf{r}_a) - U_T(\mathbf{r}) | \varphi_0 \rangle|^2 . \quad (145B)$$

To obtain the average increase in transverse energy, we must sum over all transitions,

$$\langle \delta E_\perp \rangle = \sum_n (E_\perp^n - E_\perp^0) P_{n,0} . \quad (145C)$$

In analogy to the derivation of Bethe's formula for energy loss we may apply a sum rule to evaluate this expression. For brevity, we introduce the notation,

$$\Delta U \equiv U(\mathbf{r} - \mathbf{r}_a) - U_T(\mathbf{r}) \quad \text{and} \quad H_\perp \equiv \frac{\mathbf{p}_\perp^2}{2M_1} + U_T(\mathbf{r}) .$$

and obtain, with square brackets denoting commutators,

$$\begin{aligned} \langle \delta E_\perp \rangle &\propto \sum_n (\langle \varphi_0 | [\Delta U, H_\perp] | \varphi_n \rangle \langle \varphi_n | \Delta U | \varphi_0 \rangle - \langle \varphi_0 | \Delta U | \varphi_n \rangle \langle \varphi_n | [\Delta U, H_\perp] | \varphi_0 \rangle) = \\ &= \langle \varphi_0 | [[\Delta U, H_\perp], \Delta U] | \varphi_0 \rangle \end{aligned} \quad (145D)$$

since the functions φ_n form a complete set. Only the first term in H_\perp does not commute with ΔU , and we obtain

$$\begin{aligned} [[\Delta U, H_\perp], \Delta U] &= \frac{1}{2M_1} [\mathbf{p}_\perp [\Delta U, \mathbf{p}_\perp] + [\Delta U, \mathbf{p}_\perp] \mathbf{p}_\perp, \Delta U] = \\ &= -\frac{1}{M_1} ([\Delta U, \mathbf{p}_\perp])^2 \end{aligned} \quad (145E)$$

The commutator of ΔU with \mathbf{p}_\perp is proportional to the gradient of ΔU , and we finally obtain

$$\langle \delta E_\perp \rangle \propto \langle \varphi_0 | (\nabla_r \Delta U)^2 | \varphi_0 \rangle . \quad (145F)$$

The relation to the classical expression in Eq. (140) is now clear. If we make a first-order expansion of the force fluctuation and average over thermal displacements, we obtain Eq. (143), and if the spatial distribution $|\varphi_0|^2$, averaged over states with energy near E_\perp , is the classical one, the result in Eq. (144) or (145) is retrieved, apart from constants that of course also turn out to agree.

The different contributions to $d\langle E_\perp \rangle/dz$ are illustrated for a typical case in Fig. 44. Although the electronic scattering is unimportant for random multiple scattering it plays a very important role in the increase of the minimum yield with depth because the thermal scattering is extremely weak at the lowest transverse energies. More elaborate schemes for calculation of the thermal scattering were discussed by [Schjøtt *et al.* 1983], but the simple addition of the two expressions in Eqs. (136), (137) and (144) (replaced by the random multiple scattering when the sum becomes larger than this at small distances) represents their estimate fairly well. Also, in [Matsunami and Howe 1980] this procedure was found to give reasonable results in calculations of dechanneling.

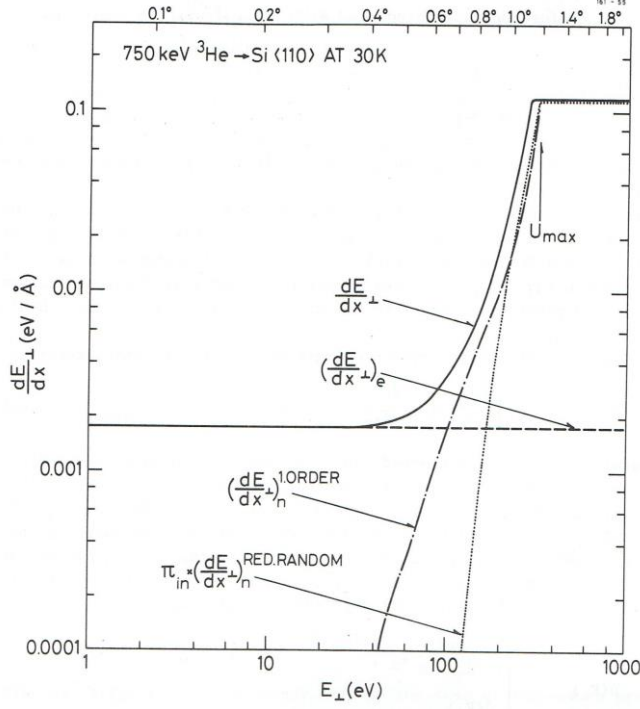


Fig. 44. The total increase per unit depth of the transverse energy from nuclear and electronic multiple scattering, together with the separate components. The two nuclear contributions are given by Eqs. (136), (137) and Eq. (144). The electron density is assumed constant equal to 0.20 electrons/Å³, corresponding to the 4 valence electrons in Si (Eq. (133A)). The angles ψ at the top correspond to $E\psi^2 = E_{\perp}$. (From [Nielsen 1987]).

Planar channeling: For planar channeling, the correlation of atomic deflections in a static lattice is less perfect and the accuracy of transverse-energy conservation hence more uncertain. An evaluation of the deflection in one collision at an impact parameter equal to the minimum distance of approach to a plane was used by Lindhard to obtain a simple estimate of the breakdown of conservation for E_{\perp} approaching V_{\max} , the potential maximum. [Beloshitsky *et al.* 1973] have derived a formula for the multiple scattering, assuming a random distribution of atoms in the planes. They concluded that the additional fluctuations induced by thermal displacements of atoms perpendicular to the planes are much smaller and hence may be ignored. (Discussion of this and of the following in [Andersen *et al.* 1988].)

When a particle moves a small distance δz at a distance x from a plane, the number n_i of collisions with momentum transfer $\Delta p_{x,i}$ follows Poisson statistics in this model. We may then apply the usual argument to derive the average increase in transverse energy,

$$\begin{aligned} \langle \delta E_{\perp} \rangle &= \frac{1}{2M_1} \langle (\sum_i (n_i - \langle n_i \rangle) \Delta p_{x,i})^2 \rangle = \\ &= \frac{1}{2M_1} \langle \sum_i (n_i - \langle n_i \rangle)^2 \Delta p_{x,i}^2 \rangle = \frac{1}{2M_1} \sum_i \langle n_i \rangle \Delta p_{x,i}^2 \end{aligned} \quad (146A)$$

where we have used $\langle (n_i - \langle n_i \rangle)(n_j - \langle n_j \rangle) \rangle = 0$ for $i \neq j$. We may use the formula in Eq. (139) to evaluate this expression,

$$\frac{d}{dz} \langle E_{\perp} \rangle = \frac{d^2}{4E} N d_p \int dy (U'(r))^2 \frac{x^2}{r^2}. \quad (146B)$$

With the standard potential, the integral may be calculated by application of the residue technique, and we obtain

$$\frac{d}{dz}\langle E_{\perp} \rangle = \frac{\pi}{8} E \psi_1^4 N d_p d^2 (Ca)^{-1} g(x/Ca) \quad \text{with} \quad (146C)$$

$$g(\xi) = \xi^{-1} + \xi^2(\xi^2 + 1)^{-3/2} + 4\xi^2(\xi^2 + 1)^{-1/2} - 4\xi ,$$

as given by [Beloshitsky *et al.* 1973]. From an expansion in $\xi^{-1} = Ca/x$, this expression may be seen to be proportional to ξ^{-5} at large ξ , $g(\xi) \approx \frac{5}{8}\xi^{-5}$ for $\xi \gg 1$.

Estimates based on a gas picture of the atomic distribution in a plane may, however, be expected to predict much too large fluctuations because the density of atoms in the plane does not fluctuate. To check this question, we have carried out computer simulations of collisions with a single plane, analogous to the axial simulations illustrated in Figs. * and **. The atoms were arranged in a simple square pattern in the plane, and for a fixed angle of incidence to the plane, ψ_{in} , the angle φ relative to the closest-packed strings in the planes was varied. For each angle (ψ_{in}, φ) , the particles were incident at a fixed (large) distance x from the plane and at positions y parallel to the plane which covered uniformly one period of the structure. Results are shown in Fig. 45 for an intermediate value of ψ_{in} , corresponding to a closest distance of approach of about $x_{min} = 0.7Ca$. The relative increase in transverse energy after the collision with the plane is generally smaller than given by formula in Eq. (146C) by more than an order of magnitude.

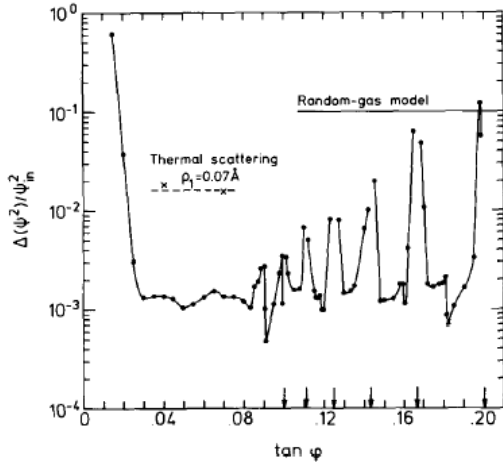


Fig. 45. Average relative increase in square angle relative to a plane after deflection by a single plane. The parameters in the simulation correspond to 1-MeV H^+ on a static (100) Si plane, φ being then the angle to the strongest axis in the plane, the [011] direction. The initial angle to the plane is $\psi_{in} = 0.0035$, corresponding to a distance of closest approach, $x_{min} = 0.7Ca$. The dots represent simulation results. At the angles indicated by arrows, negative values of $\Delta(\psi_x^2)$ were obtained. The two crosses are from simulations including thermal vibrations. The gas-model result was obtained from numerical integration of Eq. (146C) along the path. From [Andersen *et al.* 1988].

Close to the axis, $\varphi \rightarrow 0$, the conservation of E_{\perp} with respect to the plane suddenly breaks down. As discussed in Ch. 8, the plane here appears to the projectiles as a string of strings, and stability of the planar motion requires several strings to contribute to the deflection by the plane. We find by inspection that for decreasing φ the instability sets in when the particle crosses ~ 2 strings during the time it spends at distances $x < 2x_{min}$. Also when the particles move nearly parallel to higher-order axes in the plane, there are sharp increases in $\langle \delta E_{\perp} \rangle$, and the above condition on φ for onset of an axial instability of planar motion is found to hold also for these higher-order axes.

On the basis of these results, we may expect thermal scattering to play an important

role also for planes. In analogy with the axial case, we shall estimate the scattering by a combination of the overlap contribution in Eq. (136) from close collisions and the fluctuations at large distances evaluated to first order in the thermal displacements of atoms. The deflection in a single collision is given by Eq. (139) in terms of the integrated atomic potential $dU(x,y)$ and with $n = Nd_p d\delta z$ Eq. (140) is replaced by

$$\langle \delta E_{\perp} \rangle = \delta z N d_p d^2 (4E)^{-1} \int_{-\infty}^{\infty} dy \langle (\delta F_x(x,y))^2 \rangle_T \quad (147)$$

for a particle moving at distance x to a plane. The average square of the x -component of the force fluctuation is given by

$$\langle (\delta F_x(x,y))^2 \rangle_T = \rho_1^2 \left((U''(r))^2 \frac{x^2}{r^2} + (U'(r))^2 \frac{y^2}{r^4} \right). \quad (148)$$

The integral in Eq. (147) can be evaluated with the residue technique if we apply the standard potential, and the result is

$$\frac{d\langle E_{\perp} \rangle}{dz} = \frac{\pi}{8} E \psi_1^4 N d_p d^2 \frac{\rho_1^2}{(Ca)^3} f\left(\frac{x}{Ca}\right) \quad \text{with} \quad (149)$$

$$f(\xi) = 16(\xi^2(\xi^2 + 1)^{-1/2} - \xi) + 4(\xi^2(\xi^2 + 1)^{-3/2} + (\xi^2 + 1)^{-1/2}) + (\xi^{-3} + (\xi^2 + 1)^{-3/2}) - \frac{5}{2} \xi^2 (\xi^2 + 1)^{-7/2}$$

Asymptotically, $f(\xi) \approx 5 \xi^{-7}$ for $\xi \gg 1$.

If the Doyle-Turner potential is inserted into Eq. (148) and the two terms are added before the integration in Eq. (147), the Gaussian integrals are simple and we obtain

$$\begin{aligned} \frac{d\langle E_{\perp} \rangle}{dz} &= 4\sqrt{\pi} E^{-1} (e^2 a_0)^2 \rho_1^2 N d_p \sum_{i,j}^4 \frac{a_i a_j}{B_i^2 B_j^2} \left(\frac{1}{B_i} + \frac{1}{B_j} \right)^{-1/2} \times \\ &\times \left(\frac{4x^4}{B_i B_j} + 2x^2 \left(\frac{1}{B_i + B_j} - \frac{1}{B_i} - \frac{1}{B_j} \right) + 1 \right) \exp \left(-x^2 \left(\frac{1}{B_i} + \frac{1}{B_j} \right) \right). \end{aligned} \quad (150)$$

Both Eqs. (149) and (150) give the increase of E_{\perp} at distance x to the plane, and to obtain the average increase for fixed E_{\perp} , the expressions should be averaged over the equilibrium x -distribution, i.e., over one period of the motion,

$$\left. \frac{d\langle E_{\perp} \rangle}{dz} \right|_{E_{\perp}} = 2 \int_{x_{min}}^{d_p/2} dx \frac{K(E_{\perp})}{(E_{\perp} - V(x))^{1/2}} \left. \frac{d\langle E_{\perp} \rangle}{dz} \right|_x, \quad (151)$$

with $K(E_{\perp})$ given by Eq. (91).

To test the estimates of thermal scattering, the collision with an atomic plane has been simulated with random thermal displacements of the atoms, and the results are

shown in Fig. 46. The curve representing close collisions was calculated from Eq. (136), with a logarithm limited to scattering angles $\varphi < \psi_{\max}$ where ψ_{\max} corresponds to the maximum in the planar potential, $V_{\max} = E\psi_{\max}^2$. The rare scattering events with $\varphi > \psi_{\max}$ were also excluded in the simulation. In the evaluation according to Eq. (151) of the contribution from distant collisions, $d\langle E_{\perp} \rangle/dz$ was set equal to its value at $x = 2\rho_1$ for distances $x < 2\rho_1$, in order to avoid the unphysical divergence at small distances. The comparison in Fig. 46 indicates that the larger of the two analytical estimates (or their sum as for the axial case) should be used in dechanneling calculations, and it confirms that Eq. (146C) is a gross overestimate.

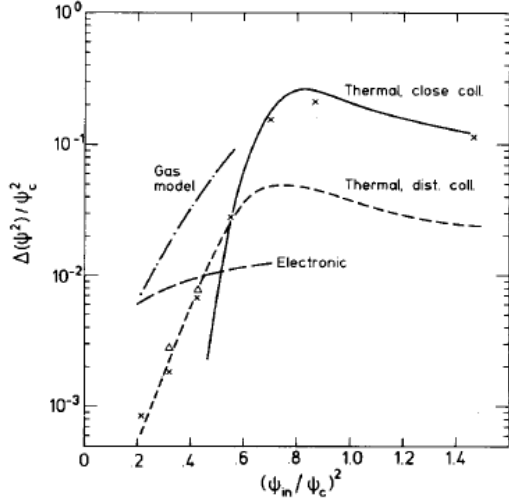


Fig. 46. Comparison of simulation results with analytical estimates. The parameters correspond to 1-MeV H⁺ on a (100) Si plane, with atoms vibrating with one-dimensional vibrational amplitude $\rho_1=0.07$ Å. The angles are normalised to the value $\psi_c=0.0054$, corresponding to the maximum of the static planar potential. The values of $\tan\varphi$ are 0.07 (x) or 0.04 (Δ). The analytical estimates were obtained by numerical integration along the path of Eq. (136) (full line), Eq.(149) (short dashed), Eqs. (128)-(130) (long dashed), and Eq. (146C) (dot-dashed). (From [Andersen *et al.* 1988]).

18. DECHANNELING

Multiple scattering may be introduced into the description of channeling provided that the assumption of statistical equilibrium on a transverse energy shell may be retained. The qualitative condition must be that the characteristic length λ_{\perp} for the trend towards equilibrium (Eq. (67)) is short compared to a characteristic length for multiple scattering. According to Eqs. (119) and (120), the path length l_{n,ψ_1} corresponding to a multiple-scattering angle $\langle\delta\Omega^2\rangle_n^{1/2} = \psi_1$ in an amorphous target is given by

$$l_{n,\psi_1} = \frac{E}{\pi N d Z_1 Z_2 e^2 L_n} = \left(\frac{\pi}{2} N d^2 \psi_1^2 L_n \right)^{-1}, \quad (152)$$

and for $\psi = \psi_1$ the ratio between the two lengths is

$$\frac{\lambda_{\perp}}{l_{n,\psi_1}} = \frac{a\psi_1 L_n}{a} \cdot \quad (153)$$

Since multiple scattering is strongly reduced for channeled particles, the hypothesis of statistical equilibrium appears well justified, at least for high energies where $\psi_1 < a/d$. The special problems with planar effects, considered in Ch. 15, will be discussed later.

For electronic scattering we obtain from Eqs. (128) and (129) the length corresponding to Eq. (152),

$$l_{e,\psi_1} = \frac{2E}{\pi N d Z_1 e^2 L_e}. \quad (152A)$$

The ratio between the two lengths, $l_{e,\psi_1}/l_{n,\psi_1}$, given by Eq. (131) is typically large compared to unity.

Integral equation. The equilibrium hypothesis implies that the change in transverse energy may be described as a Markov process: The probability of a jump from the energy E_\perp to an interval $[E'_\perp, E'_\perp + dE'_\perp]$ during passage from depth z to $z+dz$ is independent of the history of the particle and may be written as $p(E'_\perp, E_\perp) dE'_\perp dz$.

For the distribution in transverse energy, $g(E_\perp, z)$, we may then write down an integral equation expressing conservation of probability,

$$g(E_\perp, z) dE_\perp = \int dE'_\perp g(E'_\perp, z - dz) p(E_\perp, E'_\perp) dE'_\perp dz + g(E_\perp, z - dz) dE_\perp (1 - \int dE'_\perp p(E'_\perp, E_\perp) dz). \quad (154)$$

The first term gives the contribution from scattering into the interval $[E_\perp, E_\perp + dE_\perp]$ and the second the contribution from particles staying in this interval.

Letting $dz \rightarrow 0$, we obtain the Master Equation,

$$\frac{\partial g(E_\perp, z)}{\partial z} = \int dE'_\perp \{p(E_\perp, E'_\perp) g(E'_\perp, z) - p(E'_\perp, E_\perp) g(E_\perp, z)\}. \quad (155)$$

The physical interpretation is very simple: Only the difference between scattering in and scattering out changes the probability in the interval $[E_\perp, E_\perp + dE_\perp]$.

It is useful at this point to consider the discrete case, $g(E_\perp, z) \rightarrow \{f_n(z)\}$, where f_n may be the population of a quantum state with energy E_n . The integral equation then reduces to the matrix form,

$$f_n(z) = \sum_m T_{n,m} f_m(z - dz), \quad (154A)$$

with

$$T_{n,m} = \begin{cases} p_{n,m} dz & n \neq m \\ 1 - \sum_{k \neq n} p_{k,n} dz & n = m \end{cases}. \quad (154B)$$

The master equation becomes

$$\frac{\partial}{\partial z} f_n(z) = \sum_m (p_{n,m} f_m - p_{m,n} f_n). \quad (155A)$$

where $p_{n,m}$ is the probability per path length for a transition $m \rightarrow n$.

Two basic features are particularly transparent in this discrete case:

(i) *Symmetry*

$$p_{n,m} = p_{m,n} \quad (155B)$$

If the transitions are caused by a perturbation δV that may be treated to first order, the transition rate is proportional to the square of a matrix element of δV ,

$$p_{n,m} \propto |\langle n | \delta V | m \rangle|^2, \quad (155C)$$

and the symmetry is obvious.

(ii) *Equilibrium*

It follows from Eqs. (155A) and (155B) that a uniform population of quantum states is an equilibrium solution. The point of the following transformations is to reveal the corresponding properties of Eq. (155).

Density in phase space. For a discussion of symmetry of the scattering and equilibrium solution to the master equation, it is useful to introduce a probability distribution $f(E_\perp)$ in transverse phase space. Denote by $IS(E_\perp)$ the phase space (per unit cell in one or two dimensions) available to particles with a transverse energy below E_\perp and by $S(E_\perp)$ the derivative of this function. The relation between the distributions f and g may then be expressed as

$$f(E_\perp) = g(E_\perp)/S(E_\perp). \quad (156)$$

In two dimensions, we have

$$\begin{aligned} IS(E_\perp) &= \int_{A(E_\perp)} d^2\mathbf{r} \int_{\frac{p_\perp^2}{2M_1} < E_\perp - U(\bar{r})} \pi d(p_\perp^2) \\ &\propto \int_{A(E_\perp)} d^2\mathbf{r} (E_\perp - U(\mathbf{r})) \end{aligned}, \quad (157)$$

and hence

$$S(E_\perp) = \frac{d}{dE_\perp} IS(E_\perp) \propto A(E_\perp). \quad (158)$$

In one dimension, Eq. (157) is replaced by

$$IS(E_\perp) = \int_{L(E_\perp)} dx \int_{\frac{p_x^2}{2M_1} < E_\perp - V(x)} dp_x \propto \int_{L(E_\perp)} dx (E_\perp - V(x))^{1/2}, \quad (159)$$

and hence

$$S(E_\perp) \propto \int_{L(E_\perp)} dx (E_\perp - V(x))^{-1/2} \propto T(E_\perp), \quad (160)$$

where $T(E_{\perp})$ is the time of passage between neighbouring planes, which for bound states is half a period of the oscillatory motion. Collecting the results, we have

$$f(E_{\perp}) \propto \begin{cases} \frac{g(E_{\perp})}{A(E_{\perp})} & \text{axial case} \\ \frac{g(E_{\perp})}{T(E_{\perp})} & \text{planar case} \end{cases} \quad (161)$$

It may be noted that for high transverse energies, $A(E_{\perp}) \rightarrow A_0$ while $T(E_{\perp}) \propto E_{\perp}^{-1/2}$.

Symmetry of scattering. The scattering processes leading to dechanneling may often be treated in the first Born approximation, as discussed in Ch. 17, and then the symmetry in Eq. (155B) of transitions between quantum states follows from a relation of type Eq. (155C). As we shall show now, the corresponding symmetry relation for the probability $p(E'_{\perp}, E_{\perp})$ involves the density of states which is proportional to the differential phase space.

Let us select small energy intervals of width δE_{\perp} around the energies E_{\perp} and E'_{\perp} and denote by δN and $\delta N'$ the numbers of channeling states within these intervals. The probability for scattering between these intervals, e.g., $E_{\perp} \rightarrow E'_{\perp}$, may be expressed in terms of the interstate transition probabilities $p_{n,m}$ as an average over initial states m and a sum over final states n ,

$$p(E'_{\perp}, E_{\perp})\delta E_{\perp} = \frac{1}{\delta N} \sum_{n,m} p_{n,m} \begin{cases} |E_n - E'_{\perp}| < \frac{1}{2}\delta E_{\perp} \\ |E_m - E_{\perp}| < \frac{1}{2}\delta E_{\perp} \end{cases} \quad (162)$$

From the symmetry relation in Eq. (155B), it follows that

$$p(E_{\perp}, E'_{\perp}) = \frac{\delta N}{\delta N'} p(E'_{\perp}, E_{\perp}). \quad (163)$$

Since the number of states is proportional to the differential volume in transverse phase, we obtain

$$p(E'_{\perp}, E_{\perp})A(E_{\perp}) = p(E_{\perp}, E'_{\perp})A(E'_{\perp}) \quad (164)$$

for the axial case and

$$p(E'_{\perp}, E_{\perp})T(E_{\perp}) = p(E_{\perp}, E'_{\perp})T(E'_{\perp}) \quad (165)$$

for the planar case.

These symmetry relations may also be derived without reference to quantum states. In a classical description, the transitions $E_{\perp} \rightarrow E'_{\perp}$ are associated with jumps in momentum, in the axial case $\mathbf{p}_{\perp} \rightarrow \mathbf{p}'_{\perp}$ at fixed \mathbf{r} and we may introduce the

corresponding probability, $p_r(\mathbf{p}'_{\perp}, \mathbf{p}_{\perp})$. We shall argue that to a good approximation it satisfies the relation

$$p_r(\mathbf{p}'_{\perp}, \mathbf{p}_{\perp}) = p_r(-\mathbf{p}_{\perp}, -\mathbf{p}'_{\perp}) . \quad (166)$$

For electronic scattering \mathbf{p}_{\perp} and $-\mathbf{p}'_{\perp}$ are transverse momenta of two different trajectories through \mathbf{r} before an electronic excitation, and the probability of an excitation with component $\delta\mathbf{p}_{\perp} = \mathbf{p}'_{\perp} - \mathbf{p}_{\perp}$ of the momentum transfer in the transverse plane is not dependent on small differences in angle of the trajectory with the string. For thermal scattering, \mathbf{p}_{\perp} and $-\mathbf{p}'_{\perp}$ are transverse momenta after deflection at \mathbf{r} by a string atom with no thermal displacement. The two trajectories deviate by a small angle, only, so the atomic displacements required in the collision to change the two momenta by $\delta\mathbf{p}_{\perp}$ are very nearly identical. Hence the probabilities for this to happen must be nearly equal, as expressed in Eq. (166).

To obtain the probability for transitions between transverse-energy shells in phase space, we must integrate over the directions of \mathbf{p}_{\perp} and \mathbf{p}'_{\perp} . Hence the minus signs are unimportant, and the symmetry in Eq. (166) again leads to the relation in Eq. (164).

In a classical description of thermal scattering, we may also apply an argument which is analogous to the proof of equivalence between channeling and blocking given in Ch. 9. The thermal displacements of atoms may be considered static during the passage of a projectile and, according to Ch. 3, the trajectories can be calculated from Hamiltonian motion in a fixed lattice potential for each displacement configuration ν , occurring with a probability P_{ν} . Consider for axial channeling two transverse planes A and B, at depths $z_A < z_B$ in the crystal, and two transverse-energy intervals around E_{\perp} and E'_{\perp} , of widths ΔE_{\perp} and $\Delta E'_{\perp}$. Transitions from E_{\perp} to E'_{\perp} during passage from A to B can be associated with classical paths in phase space, which for $z = z_A$ belong to the transverse-energy shell around E_{\perp} and for $z = z_B$ to the shell around E'_{\perp} . Assuming statistical equilibrium at A, we may calculate the probability for the transition from the volume in transverse phase space at A of such trajectories. We denote points in transverse phase space by s and the differential volume by ds , while, as before, $S(E_{\perp})$ is the derivative of the volume associated with transverse energies below E_{\perp} , and the volume of an energy shell is $S(E_{\perp})\Delta E_{\perp}$. The probability may be expressed as

$$P_{BA}(E'_{\perp}, E_{\perp})\Delta E'_{\perp} = \sum_{\nu} P_{\nu} \frac{1}{S(E_{\perp})\Delta E_{\perp}} \int ds_A \left| \begin{array}{l} s_A \in S(E_{\perp})\Delta E_{\perp} \\ s_B^{\nu} \in S(E'_{\perp})\Delta E'_{\perp} \end{array} \right. , \quad (167)$$

where the index ν on s indicates that the phase-space coordinates at B are connected to those at A through motion in a lattice with the displacement configuration ν .

We now invoke reversibility of the motion. The trajectories included in the integral in Eq. (167) are then seen to be precisely those which with time-reversed motion lead

from E'_\perp at B to E_\perp at A, and we may express the probability for transition as

$$P_{AB}(E_\perp, E'_\perp)\Delta E_\perp = \sum_\nu P_\nu \frac{1}{S(E'_\perp)\Delta E'_\perp} \int ds_B \left| \begin{array}{l} s'_A \in S(E_\perp)\Delta E_\perp \\ s_B \in S(E'_\perp)\Delta E'_\perp \end{array} \right. . \quad (168)$$

Since, as was discussed in Ch. 9, the differential volume in transverse phase space is conserved along trajectories, we obtain from Eqs. (167) and (168) the relation

$$P_{BA}(E'_\perp, E_\perp)S(E_\perp) = P_{AB}(E_\perp, E'_\perp)S(E'_\perp) . \quad (169)$$

If the transition probabilities are the same for motion in the two directions, which holds exactly if the crystal has reflection symmetry, then the relations in Eqs. (164) and (165) follow from Eq. (169).

We may introduce the symmetry of the scattering explicitly into the master equation by expressing the scattering probability as a function of the mean of the initial and final transverse energies and of the magnitude, $|\Delta E_\perp|$, of the jump,

$$S(E_\perp + \Delta E_\perp/2)\tilde{p}(E_\perp + \Delta E_\perp/2, |\Delta E_\perp|) \equiv S(E_\perp)p(E_\perp + \Delta E_\perp, E_\perp) , \quad (170)$$

where the differential phase space $S(E_\perp)$ should be replaced by the area function $A(E_\perp)$ and the period $T(E_\perp)$ in the axial and planar cases, respectively. The symmetry relations in Eqs. (164), (165) guarantee the consistency of the definition, i.e., that the right-hand side is invariant under a change of sign of ΔE_\perp for fixed $E_\perp + \Delta E_\perp/2$. In the following we shall sometimes omit the explicit indication of this symmetry of \tilde{p} . When the relation in Eq. (170) and the phase-space density $f(E_\perp)$ are introduced into the master equation in Eq. (155), we obtain

$$\begin{aligned} \frac{\partial}{\partial z} f(E_\perp, z) = & \frac{1}{S(E_\perp)} \int d\Delta E_\perp S(E_\perp + \Delta E_\perp/2)\tilde{p}(E_\perp + \Delta E_\perp/2, |\Delta E_\perp|) \times \\ & \times \{f(E_\perp + \Delta E_\perp, z) - f(E_\perp, z)\} . \end{aligned} \quad (171)$$

It is now obvious that a constant $f(E_\perp)$ is an equilibrium solution!

Diffusion Equation. If the jumps, ΔE_\perp , in transverse energy are small compared with E_\perp , we may make a Taylor expansion around E_\perp in Eq. (171). For brevity, we omit arguments of functions and introduce the more compact notation $\varepsilon \equiv \Delta E_\perp$,

$$\frac{\partial f}{\partial z} = \frac{1}{S} \int d\varepsilon \left(S + \frac{\varepsilon}{2} S' + \dots \right) \left(\tilde{p} + \frac{\varepsilon}{2} \tilde{p}' + \dots \right) \left(\varepsilon f' + \frac{\varepsilon^2}{2} f'' + \dots \right), \quad (172)$$

where differentiation with respect to E_\perp is indicated by a dash and all terms are evaluated at E_\perp . Since \tilde{p} at E_\perp depends on the magnitude, only, of ε , the integration eliminates the lowest-order term proportional to ε (all odd-order terms, in fact). To second (or third) order, we then have

$$\frac{\partial f}{\partial z} = \frac{1}{S} \int d\varepsilon (\varepsilon^2/2) [S\tilde{p}f'' + S'\tilde{p}f' + S\tilde{p}'f'] ,$$

or

$$\frac{\partial}{\partial z} f(E_{\perp}, z) = \frac{1}{S(E_{\perp})} \frac{\partial}{\partial E_{\perp}} S(E_{\perp}) D(E_{\perp}) \frac{\partial}{\partial E_{\perp}} f(E_{\perp}, z) , \quad (173)$$

where the function $D(E_{\perp})$ is given by

$$D(E_{\perp}) = \frac{1}{2} \int d\varepsilon \varepsilon^2 \tilde{p}(E_{\perp}, \varepsilon) . \quad (174)$$

Eq. (173) is of diffusion type, with a current $-DSf'$ proportional to the derivative of the phase-space density f and to a diffusion function D . A constant density f is obviously still an equilibrium solution.

The simplification obtained by the approximation Eq. (173) to Eq. (171) is the representation of the complicated scattering function p , depending on two variables, by its second moment, $D(E_{\perp})$. This function is defined by the integral in Eq. (174) but it may be evaluated in a simpler way. Consider a narrow distribution in E_{\perp} , i.e., a particle with a well-defined transverse energy. In Ch. 17, we have derived simple analytical estimates of the change in the average transverse energy for such a distribution and through the diffusion equation this change is related to the diffusion function,

$$\frac{d}{dz} \langle E_{\perp} \rangle = \int dE_{\perp} E_{\perp} \frac{\partial}{\partial E_{\perp}} SD \frac{\partial}{\partial E_{\perp}} \frac{g}{S} .$$

By repeated partial integration we obtain

$$\begin{aligned} &= \int dE_{\perp} SD \frac{\partial}{\partial E_{\perp}} \frac{g}{S} \\ &= \int dE_{\perp} g(SD)' / S , \end{aligned}$$

and since $g(E_{\perp})$ is narrow, this may be written as

$$\frac{d}{dz} \langle dE_{\perp} \rangle = \frac{d}{dE_{\perp}} (S(E_{\perp})D(E_{\perp})) / S(E_{\perp}) . \quad (175)$$

Normally, this relation is used to evaluate the diffusion function, with the boundary condition (in the simplified geometry in Fig. 26)

$$D(E_{\perp} = U(r_0)) = 0 . \quad (176)$$

The derivation above of Eq. (175) is based on the diffusion equation and hence valid only if all changes in transverse energy are small, $\varepsilon/E_{\perp} \ll 1$. This may not always be

fulfilled for thermal scattering. To investigate corrections to Eq. (175) we consider axial channeling. If in the collision with a string atom the deviation from the average deflection is $\delta\boldsymbol{\psi}$, the change in transverse energy is given by

$$\varepsilon = 2E\psi\delta\psi\cos\gamma + E\delta\psi^2, \quad (177)$$

where γ is the azimuthal angle between $\boldsymbol{\psi}$ and $\delta\boldsymbol{\psi}$ which we may assume to be randomly distributed ($\mathbf{p}_\perp = p\boldsymbol{\psi}$ isotropic in statistical equilibrium, $\delta\mathbf{p}_\perp = p\delta\boldsymbol{\psi}$ independent of direction of \mathbf{p}_\perp). Hence the left hand side of Eq. (175) becomes

$$\frac{d}{dz}\langle E_\perp \rangle = \frac{1}{a} \frac{1}{A} \int_A d^2\mathbf{r} \langle E\delta\psi^2 \rangle_T. \quad (178)$$

Here the brackets $\langle \rangle$ denote an average over the differential transverse phase space, and $\langle \rangle_T$ indicates an average over thermal displacements of the string atom responsible for the deflection at \mathbf{r} .

To evaluate the right-hand side of Eq. (175), we apply the definition in Eq. (174) of the diffusion function, with \tilde{p} replaced by the original function $p(E_\perp + \varepsilon, E_\perp)$ (for corrections see below). In our model (Eq. (177)) the result may be written as

$$D(E_\perp) = \frac{1}{a} \frac{1}{A} \int_A d^2\mathbf{r} \left[(E_\perp - U) \langle E\delta\psi^2 \rangle_T + \frac{1}{2} \langle (E\delta\psi^2)^2 \rangle_T \right]. \quad (179)$$

If the second term may be ignored, the relation in Eq. (175) is clearly fulfilled. The requirement that scattering angles be small is a condition for the diffusion approximation and thermal scattering through large angles must be treated separately, as discussed later.

Conversely, we may also from Eq. (175) derive an expression with the form in Eq. (179), without the second term. In Eqs. (133) and (141), the average increase of the transverse energy is written as the average over the available area of a local function, i.e. of the statistical average of the increase in transverse energy for a trajectory at \mathbf{r} . Multiplying Eq. (175) by $S(E_\perp)$ we obtain for the axial case, where $S(E_\perp) = A(E_\perp)$,

$$\int_{A(E_\perp)} d^2\mathbf{r} \frac{d}{dz} \langle E_\perp \rangle_{\mathbf{r}} = \frac{d}{dE_\perp} (A(E_\perp) D(E_\perp)).$$

Integrating with the condition in Eq. (176) we obtain

$$A(E_\perp) D(E_\perp) = \int_{U(r_0)}^{E_\perp} dE'_\perp \int_{A(E'_\perp)} d^2\mathbf{r} \frac{d}{dz} \langle E_\perp \rangle_{\mathbf{r}}$$

The condition on the double integral is $E'_\perp > U(r)$, and keeping this condition we may invert the order,

$$A(E_{\perp})D(E_{\perp}) = \int_{A(E_{\perp})} d^2\mathbf{r} [E_{\perp} - U(\mathbf{r})] \frac{d}{dz} \langle E_{\perp} \rangle_{\mathbf{r}}. \quad (175A)$$

The expression in Eq. (179) was derived from Eq. (174), with the approximation $\tilde{p} \sim p$. As shown below inclusion of correction terms of first and second order in ε leads to a lowest order correction term of 3/2 times the magnitude of the last term in Eq. (179) with opposite sign. This is an indication of the arbitrariness of this term.

Correction to the approximation $\tilde{p} \rightarrow p$ in Eq. (174):

$$\Delta D(E_{\perp}) \equiv \frac{1}{2} \int d\varepsilon \varepsilon^2 (\tilde{p}(E_{\perp}, \varepsilon) - p(E_{\perp} + \varepsilon, E_{\perp})).$$

Expansion to second order in ε around E_{\perp} gives according to Eq. (170):

$$\begin{aligned} \tilde{p}(E_{\perp}, \varepsilon) - p(E_{\perp} + \varepsilon, E_{\perp}) &= \tilde{p}(E_{\perp}, \varepsilon) - S(E_{\perp})^{-1} S\left(E_{\perp} + \frac{\varepsilon}{2}\right) \tilde{p}\left(E_{\perp} + \frac{\varepsilon}{2}, \varepsilon\right) \cong \\ &\cong -\left(\frac{\varepsilon}{2} \tilde{p}' + \frac{\varepsilon^2}{8} \tilde{p}'' + \frac{\varepsilon}{2} S^{-1} S' \tilde{p} + \frac{\varepsilon^2}{4} S^{-1} S' \tilde{p}' + \frac{\varepsilon^2}{8} S^{-1} S'' \tilde{p}\right). \end{aligned}$$

The function $\tilde{p}(E_{\perp}, \varepsilon)$ and its derivatives are even in ε and hence the terms with an odd power of ε vanish in the integration over ε . This leaves

$$-\left(\frac{\varepsilon^2}{8} \tilde{p}'' + \frac{\varepsilon^2}{4} S^{-1} S' \tilde{p}' + \frac{\varepsilon^2}{8} S^{-1} S'' \tilde{p}\right) = -\frac{\varepsilon^2}{8} S^{-1} (S \tilde{p})''$$

to be inserted in the correction integral,

$$\Delta D(E_{\perp}) = -\frac{1}{16S(E_{\perp})} \frac{d^2}{dE_{\perp}^2} \int d\varepsilon \varepsilon^4 S(E_{\perp}) \tilde{p}(E_{\perp}, \varepsilon).$$

We now specialize to the axial case and use the model in Eq. (177) for the change in transverse energy over a path length d ,

$$\varepsilon = 2E\psi\delta\psi\cos\gamma + E\delta\psi^2$$

$$\varepsilon^2 = 4E^2\psi^2\delta\psi^2\cos^2\gamma + (E\delta\psi^2)^2 + 4E^2\psi\delta\psi^3\cos\gamma.$$

In the square of this we ignore the last two higher order terms,

$$\varepsilon^4 \cong 16E^4\psi^4\delta\psi^4\cos^4\gamma = 16\cos^4\gamma(E_{\perp} - U)^2(E\delta\psi^2)^2.$$

The average over γ : $\langle \cos^4\gamma \rangle = \langle \cos^2\gamma(1 - \sin^2\gamma) \rangle = \frac{1}{2} - \langle \frac{1}{4} \sin^2 2\gamma \rangle = \frac{3}{8}$.

Finally we obtain the result announced above,

$$\Delta D(E_{\perp}) = -\frac{6}{16dA(E_{\perp})} \frac{d^2}{dE_{\perp}^2} \int_{A(E_{\perp})} d^2\bar{r} (E_{\perp} - U(\bar{r}))^2 (E\delta\psi^2)^2 = -\frac{1}{dA(E_{\perp})} \int_{A(E_{\perp})} d^2\bar{r} \frac{3}{4} (E\delta\psi^2)^2.$$

In most derivations of the diffusion equation in the literature, a Taylor expansion in ε is applied directly to the master equation without introduction of \tilde{p} . The relation (175) then appears as a condition in the derivation, with a diffusion function given by Eq. (174) with \tilde{p} replaced by p .

Often the discussion of the validity of the diffusion approximation has been confused by omission of the phase-space function in Eq. (173), i.e.,

$$\frac{\partial}{\partial z} g(E_{\perp}, z) = \frac{\partial}{\partial E_{\perp}} D(E_{\perp}) \frac{\partial}{\partial E_{\perp}} g(E_{\perp}, z) . \quad (173A)$$

This equation is a good approximation only when $S(E_{\perp})$ is nearly constant, i.e., at high E_{\perp} for axial channeling ($A(E_{\perp}) \equiv A_0$) and at low E_{\perp} for planar channeling ($T(E_{\perp})$ independent of E_{\perp} for harmonic potential).

Damping. In the derivation of Eq. (173) energy loss of the particles has been ignored. Typically this loss is relatively small over the target thicknesses studied by channeling. Here we derive a simple estimate of the influence of stopping on dechanneling.

If the energy of a particle is changed from E to $E - \delta E$, the transverse energy is changed by $\delta E_{\perp} = -\delta E \varphi^2$ where φ is the angle of motion relative to the axis or plane. Since $E \varphi^2 \leq E_{\perp}$, we obtain the inequality

$$\left| \frac{dE_{\perp}}{dz} \right|_{\text{loss}} \leq \left| \frac{dE}{dz} \right| \frac{E_{\perp}}{E} ,$$

where a stopping power appropriate for channeled particles should be applied.

The decrease of E_{\perp} due to stopping contributes a probability current $-g(E_{\perp}, z) \left| \frac{dE_{\perp}}{dz} \right|_{\text{loss}}$, and minus the derivative of this current should be added to the diffusion equation,

$$\frac{\partial g(E_{\perp}, z)}{\partial z} = \frac{\partial}{\partial E_{\perp}} S(E_{\perp}) D(E_{\perp}) \frac{\partial}{\partial E_{\perp}} \frac{g(E_{\perp}, z)}{S(E_{\perp})} + \frac{\partial}{\partial E_{\perp}} g(E_{\perp}, z) \left| \frac{dE_{\perp}}{dz} \right|_{\text{loss}} . \quad (173B)$$

This term is typically not very important. However, it is interesting that it breaks the reversibility symmetry between channeling and blocking. While the damping of the motion due to stopping reduces the rate of dechanneling it increases the ‘feeding-in’ in blocking experiments, i.e., it gives a faster increase of the minimum yield with depth of penetration.

Random multiple scattering. Small-angle scattering in an amorphous foil is a two-dimensional, random-walk process which can be described as diffusion in the angle $\boldsymbol{\psi} = (\psi_x, \psi_y)$ to the initial direction of motion,

$$\frac{\partial f(\boldsymbol{\psi}, z)}{\partial z} = D^{(2)} \Delta_{\boldsymbol{\psi}} f(\boldsymbol{\psi}, z) . \quad (180)$$

It may be instructive to connect this well-known result to the diffusion equation (173) for the axial and planar cases. If we introduce polar coordinates, $\psi_x = \psi \cos \theta$ and $\psi_y = \psi \sin \theta$, we have

$$\Delta_\psi = \frac{\partial^2}{\partial \psi_x^2} + \frac{\partial^2}{\partial \psi_y^2} = 4 \frac{\partial}{\partial(\psi^2)} \psi^2 \frac{\partial}{\partial(\psi^2)} + \theta - \text{part.} \quad (181)$$

A more common form of the radial part of the Laplacian is $\Delta_\psi = \frac{1}{\psi} \frac{\partial}{\partial \psi} \psi \frac{\partial}{\partial \psi}$, but the form in Eq. (181) is easily obtained using the chain rule, $\frac{\partial}{\partial \psi} = \frac{\partial(\psi^2)}{\partial \psi} \frac{\partial}{\partial(\psi^2)} = 2\psi \frac{\partial}{\partial(\psi^2)}$. The distribution will be axially symmetric, so we can ignore the θ -part and obtain

$$\frac{\partial f}{\partial z} = \frac{\partial}{\partial(\psi^2)} 4\psi^2 D^{(2)} \frac{\partial}{\partial(\psi^2)} f. \quad (182)$$

Comparison with Eq. (173) shows that the diffusion function is given by

$$D(E_\perp) = 4D^{(2)} E E_\perp \quad (183)$$

when $S(E_\perp) = A_0 = \text{const.}$ Thus random scattering leads to an axial diffusion function which is linear in E_\perp , as may also be seen from the relation in Eq. (175).

For planar scattering Eq. (180) may be integrated over the angle ψ_y parallel to the plane to obtain

$$\frac{\partial f(\psi_x, z)}{\partial z} = D^2 \frac{\partial^2}{\partial \psi_x^2} f(\psi_x, z). \quad (184)$$

This may be compared with Eq. (173) with $S \propto E_\perp^{-1/2}$ which may be written

$$\frac{\partial f}{\partial z} = \frac{\psi_x}{E^2} \frac{\partial}{\partial(\psi_x^2)} D \psi_x^{-1} \frac{\partial}{\partial(\psi_x^2)} f = \frac{1}{4E^2} \frac{\partial}{\partial \psi_x} D \psi_x^{-2} \frac{\partial}{\partial \psi_x} f. \quad (185)$$

The random-diffusion function for the planar case is hence also given by Eq. (183). It is easy to see that this is consistent with Eq. (175).

Model solution of diffusion equation. Eqs. (182) and (184) can be useful approximations also for channeled particles. As seen in Figs. 44 and 46, the multiple scattering is for low transverse energies dominated by electronic scattering, which does not vary strongly with E_\perp . At large E_\perp , the thermal scattering sets in abruptly, increasing the multiple scattering by at least an order of magnitude. This behaviour suggests a simple model: For transverse energies smaller than a critical value, $E_{\perp,c} = E\psi_c^2$, we assume random multiple scattering in an electron gas of constant density, and the onset of thermal scattering is represented by a boundary condition, $f(E_{\perp,c}, z) = 0$. Such a model was applied to planar dechanneling by [Feldman and Appleton 1973] and [Beloshitsky *et al.* 1973].

First we consider Eq. (184), corresponding to one-dimensional diffusion without spatial restriction, i.e., $S(E_\perp) \propto \psi^{-1}$. Physically, this corresponds to a rectangular Kronig-Penney-type planar potential. In analogy to a standard technique for solving the

Schrödinger equation in quantum mechanics, the equation may be solved by expansion in eigenfunctions, $f \propto \exp(\alpha\psi_x)$, where α is a complex number and $D^{(2)}\alpha^2$ the eigenvalue. The boundary conditions are $f(\psi_c) = 0$ which leads to the expansion

$$f(\psi_x) = \sum_1^\infty f_n(z) \cos\left(\frac{\pi(2n-1)\psi_x}{2\psi_c}\right). \quad (186)$$

According to Eq. (184), the coefficients decrease exponentially,

$$f_n(z) = f_n^0 \exp\left(-D^{(2)} \frac{\pi^2(2n-1)^2}{4\psi_c^2} z\right), \quad (187)$$

where the initial amplitudes are given by

$$f_n^0 = \frac{2}{\psi_c} \int_0^{\psi_c} d\psi_x f(\psi_x, z=0) \cos\left(\frac{\pi(2n-1)\psi_x}{2\psi_c}\right). \quad (188)$$

For an initially well-channeled beam, the first few coefficients f_n^0 are similar in magnitude but according to Eq. (187) the $n = 1$ term will dominate for large depths, and the channelled fraction of the beam will decrease with a characteristic half-depth $l_{1/2}$ given by

$$l_{1/2} = \log 2 \frac{4\psi_c^2}{\pi^2 D^{(2)}} = 1.12 \frac{\psi_c^2}{\frac{d}{dz}\langle\psi^2\rangle}, \quad (189)$$

where we have introduced the relation for multiple scattering in two dimensions,

$$\frac{d}{dz}\langle\psi^2\rangle = 4D^{(2)}, \quad (190)$$

which follows from Eq. (182) by repeated partial integration of

$$\frac{d}{dz}\langle\psi^2\rangle = \frac{d}{dz} \int d^2\boldsymbol{\psi} \psi^2 f(\boldsymbol{\psi}, z) = \int_0^\infty \pi d(\psi^2) \psi^2 \frac{\partial}{\partial(\psi^2)} 4D^{(2)} \psi^2 \frac{\partial}{\partial(\psi^2)} f(\boldsymbol{\psi}, z).$$

The result in Eq. (189) contains an important scaling rule. As a function of beam energy, the critical angle scales as $\psi_c^2 \propto E^{-1}$ (Eqs. (29) and (35)) and the multiple scattering as $\langle\delta\Omega^2\rangle \propto E^{-2}$ (ignoring the logarithmic dependence in Eq. (129)). Hence we obtain the scaling

$$l_{1/2} \propto E, \quad (191)$$

which has been confirmed experimentally over many orders of magnitude in E . (At relativistic energies, $E \rightarrow \frac{1}{2}pv$.)

Also the magnitude of $l_{1/2}$ is obtained quite accurately from Eq. (189). As an example, we may take the results given by [Feldman and Appleton 1973]. For 8.9-MeV protons along a (110) Si plane, $l_{1/2} = 16.6 \mu\text{m}$. For the angle ψ_c in Eq. (189), we may use formula in Eq. (35) for the

characteristic planar angle ψ_p giving $\psi_c = 7.5 \times 10^{-7}$. The electron density between (110) planes is about 4 electrons/atom in Si, or $n = 0.2 \text{ \AA}^{-3}$. This gives a plasmon energy of $\hbar\omega_0 = 16.6 \text{ eV}$ and a multiple-scattering angle $d/dz \langle \psi^2 \rangle = 4.8 \times 10^{-8} \text{ \mu m}^{-1}$ according to Eqs. (128)-(130). Inserting into Eq. (189), we obtain $l_{1/2} = 17.5 \text{ \mu m}$, which is very close to the experimental value. However, this close agreement may be somewhat fortuitous.

Axial-dechanneling experiments. First we consider the depth dependence of the minimum yield. Owing to thermal and electronic multiple scattering, the distribution $g(E_\perp)$ broadens, the tail towards high E_\perp becomes more pronounced and χ_{\min} increases. Figure 47 shows a comparison between a measurement of $\chi_{\min}(z)$ and a calculation [Pedersen *et al.* 1975] with the diffusion equation (173). The diffusion function was taken from [Schjøtt *et al.* 1975] and includes electronic scattering from a uniform distribution of the four valence electrons per atom, Eq. (133A). The thermal scattering was represented by a diffusion function close to the sum of a first-order perturbation expression, Eq. (144), and a term equal to the random diffusion function multiplied by $\Pi_{\text{in}}(E_\perp)$, Eq. (136), limited from above by the random diffusion function.

Fig. 47 illustrates the temperature dependence of dechanneling in Si, a material with very high quality crystals due to the technological development. The agreement between experiment and the calculation is excellent except at very small depths. This can be explained by the Barrett correction, discussed in Ch. 15. We shall later discuss how to include this effect in the calculations.

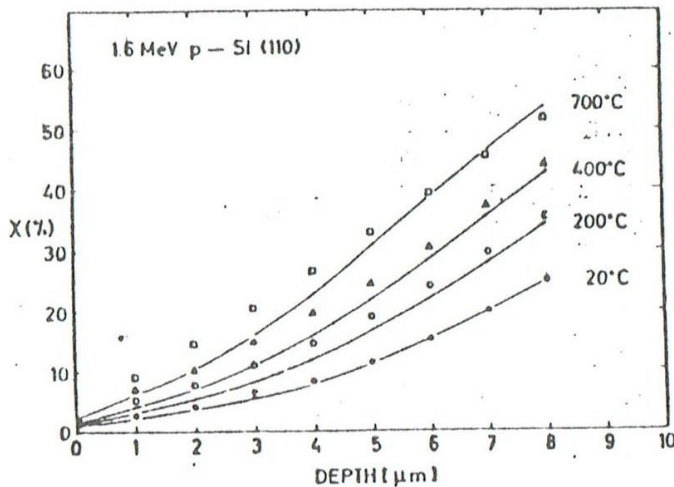


Fig. 47. Minimum yield in backscattering dips as a function of depth, for different crystal temperatures, compared with diffusion calculations. From [Pedersen *et al.* 1975].

In Fig. 48 are shown results from measurements in W, another material with very perfect crystals, described at one time by John Davies as “God’s gift to channelers”! For other materials investigated by Pedersen *et al.* (Fe, Nb, Mo, Ta) the agreement with calculations was much worse, indicating presumably a high density of crystal defects.

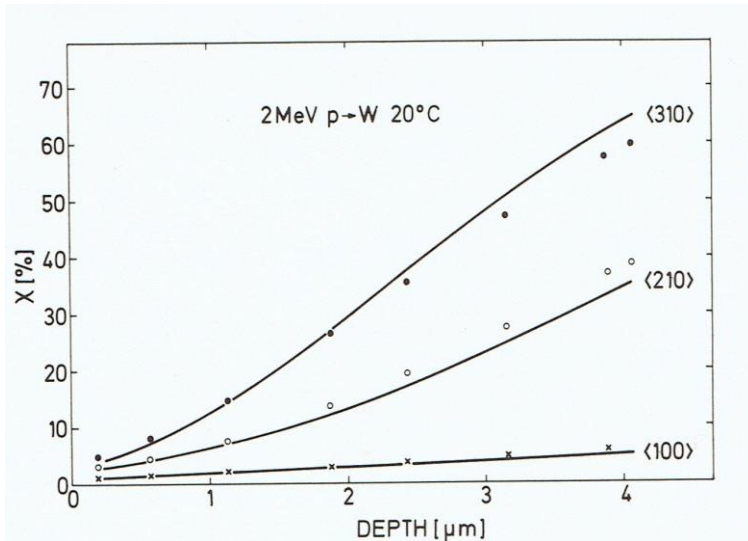


Fig. 48. Minimum yield in back-scattering dips as a function of depth in tungsten for different axial directions, compared with diffusion calculations. From [Pedersen *et al.* 1975].

Not only the minimum yield but also the width of the channeling dips change with depth due to multiple scattering. This is illustrated in Fig. 49 for channeling in both Si and W. Again the reproduction by diffusion calculations is quite good.

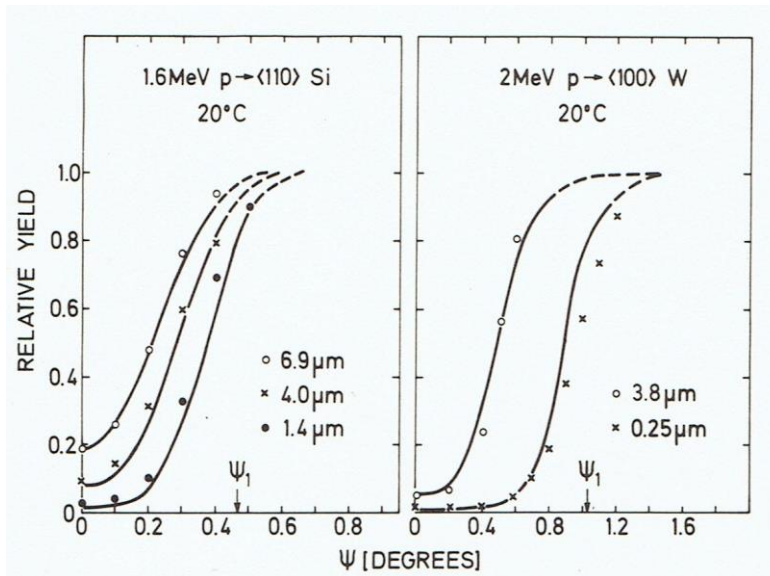


Fig. 49. Comparison of measured angular scans through a major axis in silicon and tungsten with diffusion calculations. From [Pedersen *et al.* 1975].

Perhaps the most direct test of the diffusion model is a measurement of the angular distribution of particles incident on a thin crystal parallel to an axis after exit from the backside of the crystal. One advantage is the well-defined depth of penetration. In backscattering experiments there is some uncertainty in the conversion of energy loss to depth due to the modification of the energy-loss rate by channeling (see discussion of Fig. 19). Such transmission experiments were also conducted by [Pedersen *et al.* 1975], as illustrated in the following figures.

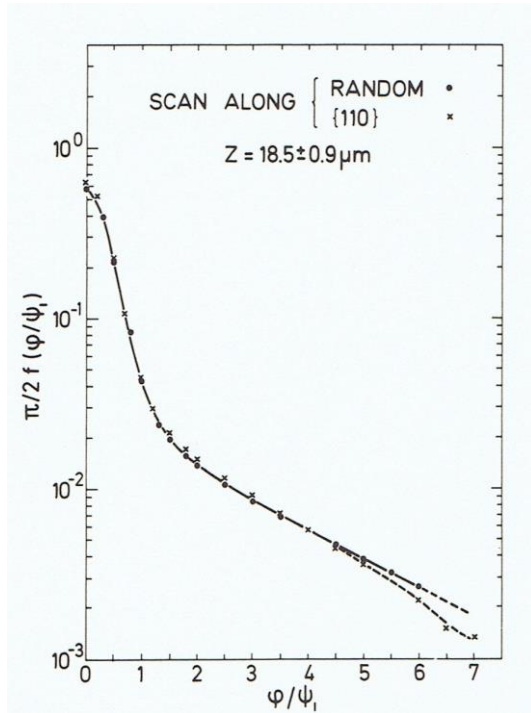


Fig. 50. Measured forward angular distribution of 1.6 MeV protons incident on a thin Si crystal along a $\langle 110 \rangle$ direction. Note that the (polar) exit angle to the axis is here denoted φ instead of the more common θ . The scan was performed at two azimuthal angles, one corresponding to a $\{110\}$ plane and one to a direction between major planes (RANDOM). From [Pedersen *et al.* 1975].

The agreement in Fig. 50 is almost too perfect (see below). The sharp change of slope around the critical angle reflects the rapid increase of the nuclear scattering at high transverse energies. Compared to the distribution for the off-plane scan, the angular distribution for the $\{110\}$ scan is slightly lower near the critical angle and falls off more rapidly at large angles. This was to be expected due to the weaker multiple scattering for planar channeled particles. The surprise was that the difference is so small. In photographic recordings of particles transmitted through thin crystals (so called star patterns) the contrast appears to be much larger. This may be due to the high sensitivity of films to small contrasts. According to Fig. 50 planar channeling seems to play a fairly weak role in axial dechanneling. (See, however, the discussion below of the Barrett correction in dechanneling.)

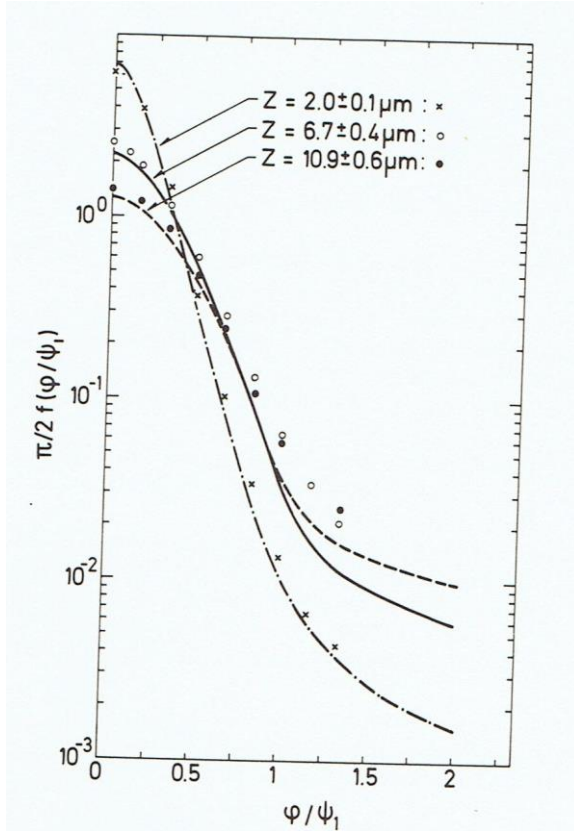


Fig. 51. Forward angular distributions of 1.6 MeV protons incident along a $\langle 110 \rangle$ direction in Si crystals of different thickness. The experimental points are compared with diffusion calculations. From [Pedersen *et al.* 1975].

That the fantastic agreement with calculations in Fig. 50 is to some extent fortuitous is shown in Fig. 51. For the thicker crystals, the calculated curve is well below the experimental points at the larger angles. As noted in [Pedersen *et al.* 1975] and [Schjøtt *et al.* 1975], the explanation may be an overestimate of random multiple scattering. The logarithm (Eq. (125)) in the formula for the mean square multiple scattering angle should be reduced to include only scattering angles below $\sim \psi_1$ and this reduction was not included in the calculations. The modification was estimated to reduce the calculated increase of minimum yields by 10-20% and would therefore make the agreement a little worse in Figs. (47) and (48). However, there are other uncertainties, e.g. due to application of the (simple) standard potential. As noted in Ch. 15, the Doyle-Turner potential is more accurate for Si and gives slightly narrower channeling dips, which again leads to faster dechanneling [Nielsen 1987].

Restriction in phase space and Barrett correction. In Ch. 15 we discussed the corrections to minimum yields in axial channeling found by Barrett from computer simulation of channeling. The main correction could be accounted for by the introduction of a restriction in phase space for axial channeling. For incidence parallel to an axis, the particles contributing to the minimum yield start out near a string in their transverse motion, thereby acquiring a transverse energy $U(r) \sim E\psi_1^2$. Such particles are restricted from becoming channeled relative to a major plane containing the axis and hence have an enhanced close-encounter probability (planar shoulders). A systematic inclusion of this restriction into the diffusion model for dechanneling was discussed in [Andersen *et al.* 1994].

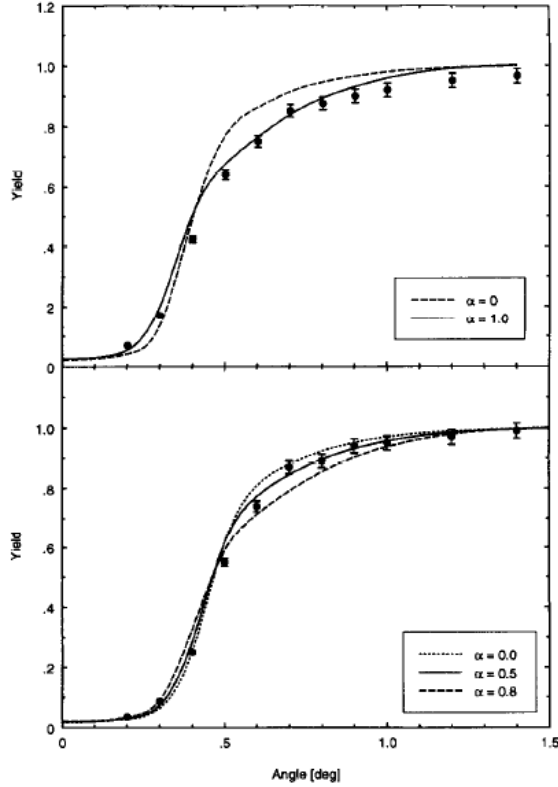


Fig. 52. Comparison of azimuthally averaged axial scans of the backscattering yield of 2-MeV He in Si with calculations based on restricted equilibrium. The yield is shown as a function of the angle of incidence to the axis and it is normalized to random yield. The depths were 4080 Å and 4240 Å for the <111> axis (upper) and <110> axis (lower), respectively. The values of the critical angle ψ_1 are 0.53 and 0.59 deg., respectively. For both cases the calculation corresponding to complete statistical equilibrium ($\alpha = 0$) is also shown.

From [Andersen *et al.* 1994].

A restriction to particles that are not channeled relative to a plane reduces the available phase space by a factor $R(\varepsilon, \mathbf{r})$ (notation $\varepsilon = E_{\perp}/E\psi_1^2$) and the spatial average of this factor is denoted $R(\varepsilon)$. A parameter α was introduced to vary the average restriction factor and a dependence on transverse energy was included,

$$R(\varepsilon) = 1 - \frac{\alpha}{1 + 0.02\varepsilon^{-2} + \varepsilon^{1/2}}. \quad (192)$$

The form of this expression was chosen to correspond qualitatively with the stereogram shown in Fig. 10. For $\varepsilon \gg 1$ the fraction of the circle at constant ψ corresponding to planar channeling decreases proportional to $\varepsilon^{-1/2}$ and the restriction also disappears at very small ε . Near $E_{\perp} = E\psi_1^2$, the restriction factor is close to $(1 - \alpha/2)$ and the yield enhancement is the reciprocal of this factor (Eq. (102)).

Consider the three stages of particle motion in this model. The surface transmission in Eq. (74A) is modified to

$$g_0(\varepsilon) = \frac{1}{A_0} \int d^2\mathbf{r} R(\varepsilon, \mathbf{r}) \delta(\varepsilon - \psi^2 - U(\mathbf{r})), \quad (193)$$

where the angle of incidence has been expressed in units of ψ_1 . Note that the integral of this distribution is less than unity because planar channeled trajectories have been omitted. In stage 2 the distribution is modified by multiple scattering as described by the diffusion equation in Eq. (173) (with $f = g/S$). Here the restriction is included through the replacement $S(\varepsilon) \rightarrow R(\varepsilon)S(\varepsilon)$. In stage 3, the close-encounter

process, the restriction enhances the yield (Eq. (102)).

We first focus on the yield near the critical angle (Fig. 52). The values of α used in the various calculations are given in the figure. Except for very small angles ψ the spatial dependence of the restriction factor in Eq. (193) is not important and it was not included in the calculations. Without multiple scattering, this factor then cancels the enhancement in Eq. (102) and the yield is therefore at small depths not influenced by the restriction. However, for incidence near the critical angle the particles are quickly scattered to larger angles where the yield enhancement is smaller. This reduces the yield just above the critical angle, and the effect is reproduced quite well by the calculations. The strongest effects of restriction are seen in the dip for the $\langle 111 \rangle$ axis which is contained in three strong $\{110\}$ planes at 60° to each other (Fig. 10).

For the Barrett factor on the minimum yield the spatial dependence of R in Eq. (193) is decisive. The minimum yield is due to particles incident close to a string where R is close to unity and hence does not cancel the enhancement in Eq. (102). However, due to multiple scattering this enhancement is decreasing slowly with depth. This was studied by computer simulation of blocking for 2.12 MeV He in Al. It was found that the enhancement decreases roughly exponentially with a characteristic decay depth of $1.4 \mu\text{m}$. Fig. 53 shows the results of dechanneling calculations with a diffusion model including this depth dependence of restriction in phase space.

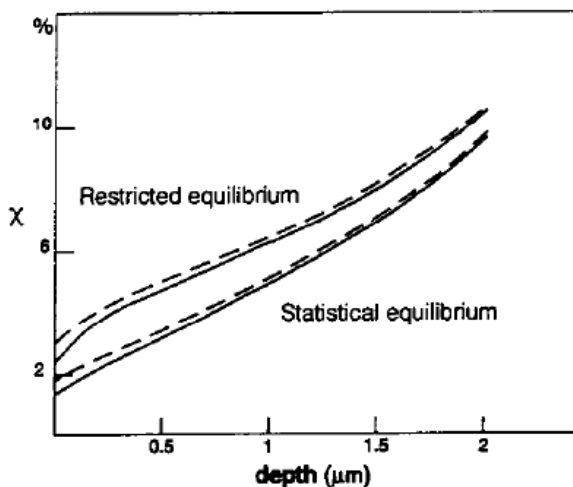


Fig. 53. Depth dependence of the minimum yield in $\langle 110 \rangle$ axial blocking of 2.12 MeV α particles in Al. The curves refer to calculations with restricted equilibrium (upper two) or complete equilibrium (lower two). The dashed lines correspond to calculations including the effects of thermal fluctuations in surface transmission (Fig. 35). From [Andersen *et al.* 1994].

The restriction increases the minimum yield close to the surface by nearly a factor of two but when the minimum yield reaches about 10% the relative effect of restriction is reduced to about 10%, only. Hence the Barrett correction is not a serious complication for studies of dechanneling like in Fig. 47. Note also that the modification of the surface transmission by thermal fluctuations, illustrated in Fig. 35, only has a significant effect on the minimum yield near the surface.

Experiments on planar dechanneling. The accuracy of the description for planar dechanneling discussed above was investigated in [Kennedy *et al.* 1992] and we show here a few of the results. A Doyle-Turner potential was used together with the prescriptions for electronic and nuclear multiple scattering from [Bak *et al.* 1988] (Eqs. (134A), (136) and (149)).

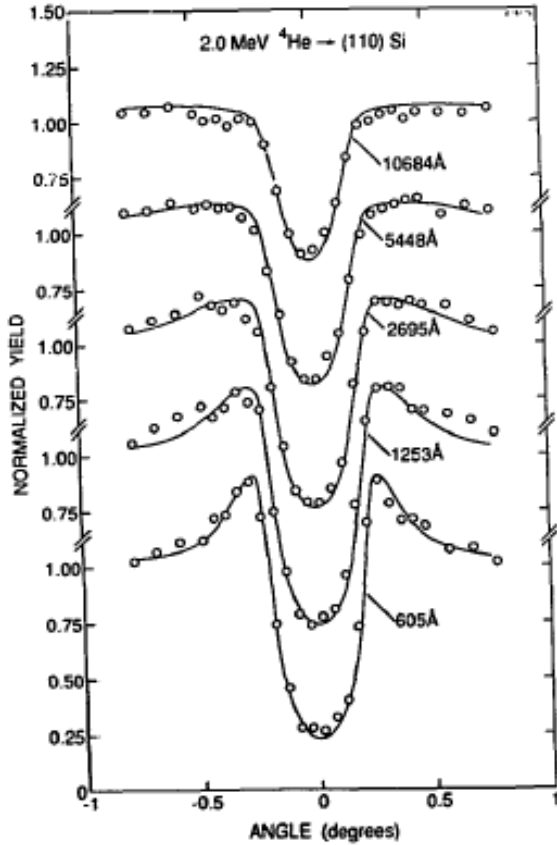


Fig. 54. Normalized yield of backscattering of 2 MeV He at various depths in a Si crystal for incidence near a {110} plane. The solid lines represent the results of diffusion-model calculations. From [Kennedy *et al.* 1992].

The agreement is extraordinarily good! The same holds for the comparison in Fig. 55 with scans through weaker planes in Si. For the scan through the strongest plane in a tungsten crystal (bcc structure), shown in Fig. 56, the calculations predict a too rapid disappearance of the high shoulders but are otherwise also in excellent agreement with the experiment. We may conclude that the diffusion model works very well for planar channeling where there is no complication by an interplay between axial and planar effects.

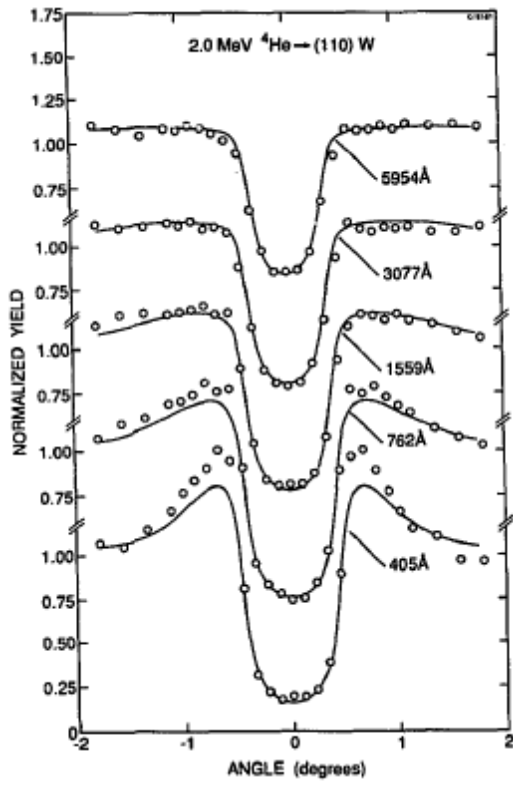


Fig. 55. As Fig. 54 but for 2 MeV He along {100} and {111} planes in Si.

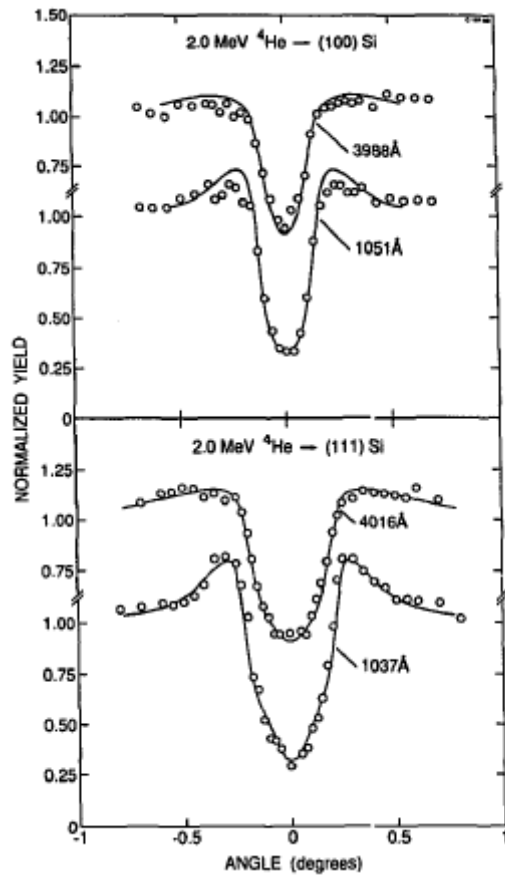


Fig. 56. As Fig. 54 but for 2 MeV He along a {110} plane in W.

19. STOPPING AND ATOMIC PROCESSES IN CHANNELED IONS

We shall now turn to aspects of channeling which Lindhard denoted secondary phenomena, i.e., phenomena which are influenced by channeling but do not in turn affect the steering of the ions very much. The most prominent example is stopping.

Stopping

Studies of ion ranges, both computer simulations and range measurements, played a very important part in the discovery of channeling (see, for example, the introduction to [Eriksson *et al.* 1967]). The energy loss to atomic recoils, the so-called nuclear energy loss, is subject to the largest reduction by channeling, and very long ranges of low-energy heavy ions were observed for incidence parallel to an axis in a crystal.

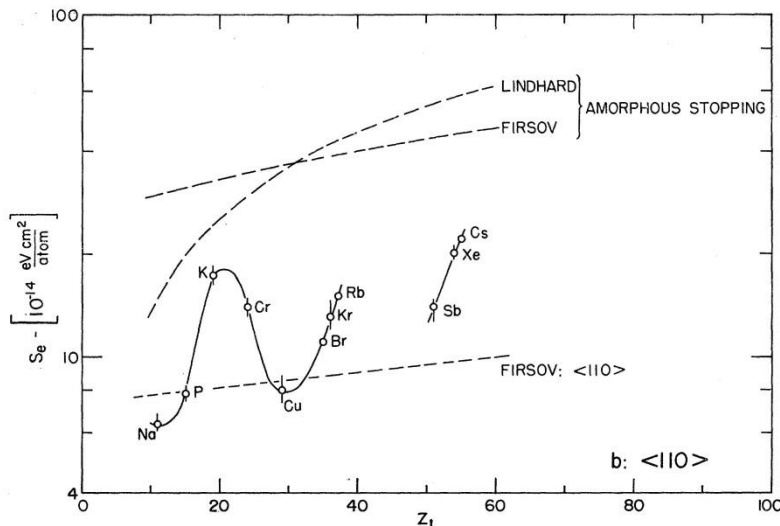


Fig. 57. Electronic-stopping cross section at velocity $v=1.5 \times 10^8$ cm/s versus the atomic number of the projectile, derived from the range of a perfectly channeled ion along a $\langle 110 \rangle$ direction in tungsten [Eriksson *et al.*, 1967].

The selection by channeling of large impact parameters with atoms makes it possible to study the electronic energy loss at low velocities where nuclear energy loss dominates in an amorphous material. A nice example is illustrated in Fig. 57 showing the dependence on Z_1 of the electronic stopping cross section, S_e (energy loss per unit length divided by the electron density). The oscillatory dependence stems from the so-called Ramsauer-Townsend effect. The cross section for electron scattering on the penetrating ion may be written as a sum over angular momenta and at low velocity the s-wave cross section dominates. With increasing strength of the scattering potential, the s-wave phase shift increases, and the cross section has strong minima when the phase shift passes through multiples of 2π [Finnemann 1968], [Briggs and Pathak 1973]. The oscillations were first seen in

the stopping in amorphous foils but the elimination of atomic recoils and the restriction of electronic scattering to the thin electron gas far from atoms make the oscillations much more prominent.

At high velocities the slowing down is mainly due to electronic energy loss. For small Z_1 it may be obtained by a quantum perturbation calculation. The resulting Bethe-Bloch formula may be written as an integral over impact parameters, leading to a logarithm of the ratio of an adiabatic radius divided by half the reduced wavelength of the electrons in the ion rest frame (Eq. (129)),

$$-\frac{dE}{dz} \cong \frac{4\pi Z_1^2 e^4}{m_0 v^2} N Z_2 \log\left(\frac{v/\langle\omega\rangle}{\lambda/4\pi}\right), \quad (194)$$

where $\omega = I/\hbar$ is an appropriately averaged frequency of virtual oscillators. (A numerical factor close to unity on the adiabatic radius has been omitted [Bohr 1948]). The observations of a reduced electronic energy loss for a substantial fraction of MeV protons penetrating several micron thick crystals demonstrated convincingly that channeling is not a simple transparency effect for low energy ions (Fig. 2).

Asymptotically for large v the expression in Eq. (194) has equal contributions from large and small impact parameters (equipartition). Therefore the energy loss is at high velocities reduced by about a factor of two for the best channeled particles [Lindhard 1965]. As demonstrated by [Esbensen and Golovchenko 1976], the theory simplifies in the high-velocity limit, and excellent agreement with measurements of the energy loss for relativistic channeled particles in thin Si and Ge crystals was obtained [Esbensen *et al.* 1978]. Also the shape of the energy distribution for channeled particles could be accounted for when fluctuations of large energy transfers in single collisions with electrons were taken into account (Landau distribution). Many other experiments and calculations on the stopping of channeled ions have been published [Cohen and Dauvergne 2004].

An attempt at a detailed comparison with standard stopping theory for swift heavy ions is discussed in the following [Andersen *et al.* 1996]. In the experiment 15.3 MeV/u Br³³⁺ ions (u or amu is the atomic mass unit) were passed through a very thin (1 μm) Si crystal and both the emergent charge state and the energy-loss spectrum were measured with a magnetic spectrometer. As illustrated in Fig. 58, the 33+ ions with only the K-shell electrons remaining undergo very little capture or loss of electrons when incident along a $\langle 110 \rangle$ axis. This phenomenon of ‘frozen charge state’ was first observed and applied by Datz and co-workers in Oak Ridge in their pioneering experiments on channeling of high-energy, heavy ions [Krause

and Datz 1996]. It is important for the analysis of the energy loss because the complication of a fluctuating charge state is removed.

The energy spectra for exiting 33+ and 32+ ions are shown in Fig. 59. For reference, also the energy spectrum for ions incident in a random (i.e., non-channelling) direction is shown, and the energy loss is given as a fraction of the random energy loss (4.9 MeV for 1 μm Si). Nearly all the 33+ ions have a much lower energy loss than for random incidence, reflecting that nearly all the ions are channeled. The spectrum for the much fewer 32+ ions contains two parts, well channeled ions which have captured a valence electron, with an energy spectrum similar to that for 33+ ions, and poorly

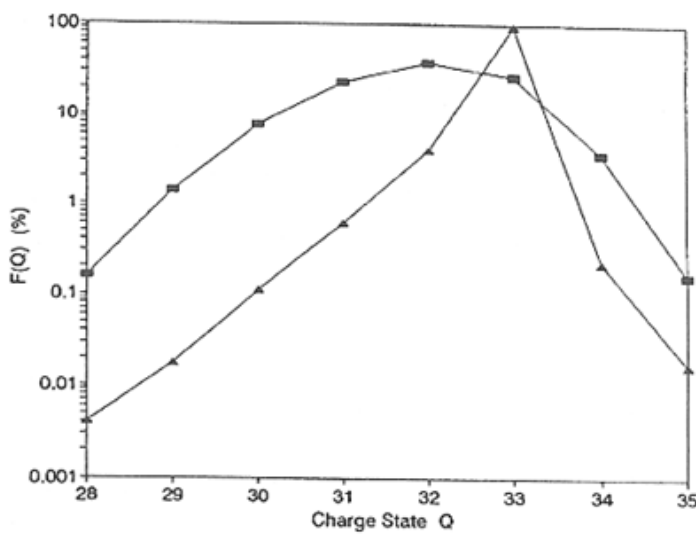


Fig. 58. Charge-state distributions for a random (□) and a $\langle 110 \rangle$ aligned (Δ) beam of 15.3 MeV/u Br^{33+} ions after passage of a 1 μm Si crystal [Andersen *et al.* 1996].

channeled ions which have entered the crystal close to a string and scattered to angles of order ψ_1 , with energy loss

similar to or even larger than random. There is also a small component of such ions in the 33+ spectrum but it is strongly enhanced for 32+ ions because the capture probability is much higher for random than for channeled ions (Fig. 58).

For the analysis of the energy loss, the well channeled ions have been divided into three groups. For fixed trajectory, the straggling in energy loss is small. This can be seen from the width of the random energy loss peak which has about equal contributions from charge-exchange straggling and Bohr straggling (fluctuations in hard collisions). For channeled particles there is only the Bohr straggling and it is reduced due to the lower electron density. The width of the energy loss distribution therefore comes mainly from the distribution in transverse energy and the associated variation of the allowed area in the transverse plane. If the spatial variation of the energy loss rate is known, the energy distribution can be calculated and compared with the measurement.

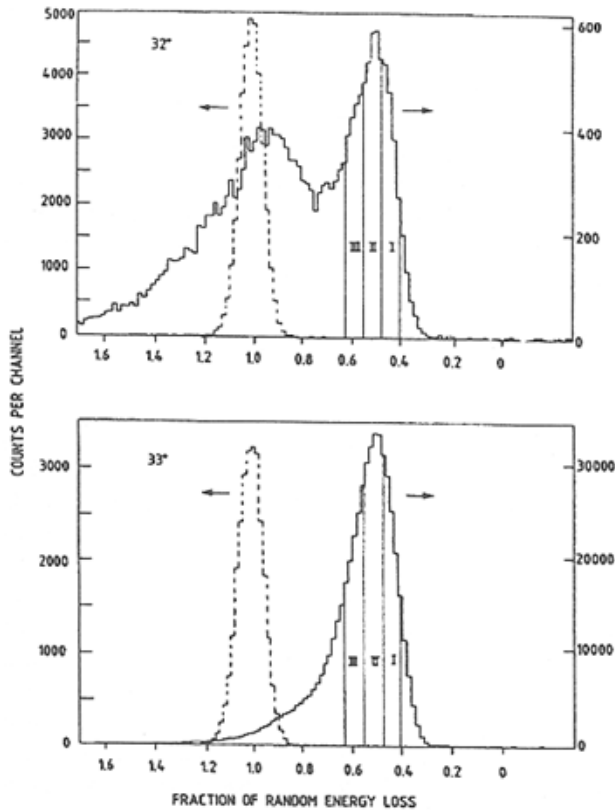


Fig. 59. Energy-loss of ions exiting with charge states $32+$ and $33+$ for a beam of $15.6 \text{ MeV/u } ^{79}\text{Br}^{33+}$ ions. Spectra for random (----) and $\langle 110 \rangle$ (—) alignment are shown as functions of the energy loss relative to the average random loss of $\Delta E=4.9 \text{ MeV}$ for the $1 \mu\text{m}$ thick Si target [Andersen *et al.* 1996]. Three energy windows, I, II, and III, are indicated that were used in the analysis of charge exchange.

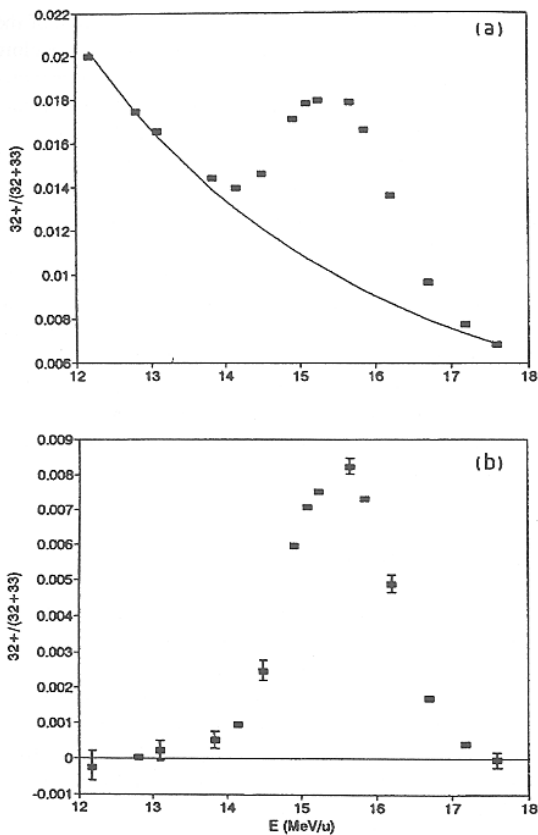


Fig. 60. (a) The charge state fraction $32+/(32++33)$ for channeled ions with energy loss in the combined windows I, II, and III in Fig. 59, as a function of the ion energy. (b) Data in (a) after subtraction of a smooth background. [Andersen *et al.* 1996].

The analysis was based on a simple description of the energy loss as consisting of three parts, the energy transfers to K-, L-, and M-shell electrons. The corresponding oscillator strengths and excitation frequencies could be estimated rather accurately, and the dependence of the energy loss on transverse energy was then calculated. Compared with the Bethe-Bloch formula given above there are two important corrections for heavy ions. First Bohr's kappa (Eq. (3) with $Z_2=1$) is larger than unity and the classical counterpart, the Bohr formula, should be applied instead, with the reduced electron wavelength replaced by the classical collision diameter. Second, there may be a significant, so-called Barkas correction which is of third order in Z_1 . It is about 5%, only, for the present case. Good agreement with the measurement was obtained. The dependence of the stopping on transverse energy turns out to come partly from the spatial variation of the density of valence (M-shell) electrons, partly from the adiabatic cut-off of energy loss to the L-shell at large impact parameters with atoms. For well-channeled ions, excitation of L-shell electrons contributes about 10% of the energy loss.

Crystal as special target for atomic processes

Studies of energy loss are just one example of the use of crystals as special targets for measurements on atomic processes [Krause and Datz 1996]. For channeled ions, the target is essentially a gas of the valence electrons. This has been utilised to study capture processes like radiative electron capture (REC) and dielectronic electron capture (or dielectronic recombination (DR)). The latter process can be viewed as a resonance enhancement of REC when the radiation energy matches an atomic transition.

An example from the experiment on Br^{33+} ions discussed above is illustrated in Fig. 60. The ratio between the numbers of $32+$ and $33+$ ions within the energy window I+II+III in Fig. 59 is here plotted as a function of the bombarding energy. The DR peak in Fig. 60b, obtained after subtraction of a smooth background from other capture processes, occurs at a velocity where the energy of a Si valence electron recorded in the ion rest-frame matches the K-shell binding energy minus twice the L-shell binding in the ion. An electron can then be captured with simultaneous excitation of a K-shell electron. The width of the resonance comes from the spread of electron velocities in the electron gas. The electron capture at the resonance should be followed by K-xray emission and this was indeed observed in the experiment.

Another process which should be mentioned in this connection is resonant coherent excitation (RCE), sometimes called the Okorokov effect [Okorokov 1965]. Here a Fourier component of the periodic field from strings of atoms is used to excite a bound electron. Channeling is again used to avoid close collisions and thereby to

maintain a well-defined atomic state during the interaction. The excitation can be observed either by detection of radiative de-excitation outside the crystal or by observation of the emergent charge state distribution as a function of bombarding energy. At velocities where a multiple of the frequency of collisions with atoms on a string matches a transition frequency in the ion, the atomic excitation gives rise to an increase in the rate of electron loss and hence to an increase in the charge state. The effect was first observed unambiguously at Oak Ridge [Moak *et al.*, 1973]. Recently, mainly a Japanese group working at the high-energy accelerator laboratory RIKEN has been active in this area, extending the observations to heavier ions carrying a few electrons [Nakai *et al.* 2005].

In the Aarhus-Chalk River collaboration on channeling studies we investigated this effect for hydrogen-like Si^{13+} ions channelled along $\langle 111 \rangle$ and $\langle 112 \rangle$ axes in Si. The resonance condition for excitation of an electron in the hydrogenic ground state, $n=1$, by the k 'th harmonic of the string potential is

$$E_n - E_1 = kh \frac{\gamma v}{d}, \quad (195)$$

where v is the velocity, d/γ is the period of the string potential, contracted by the relativistic factor $\gamma = (1-v^2/c^2)^{-1/2}$, and h is Planck's constant. The arrows in Fig. 61 indicate the beam energies calculated from Eq. (195) for transitions to $n = 2, 3, 4$ induced by the 7th and 8th harmonic of the string field.

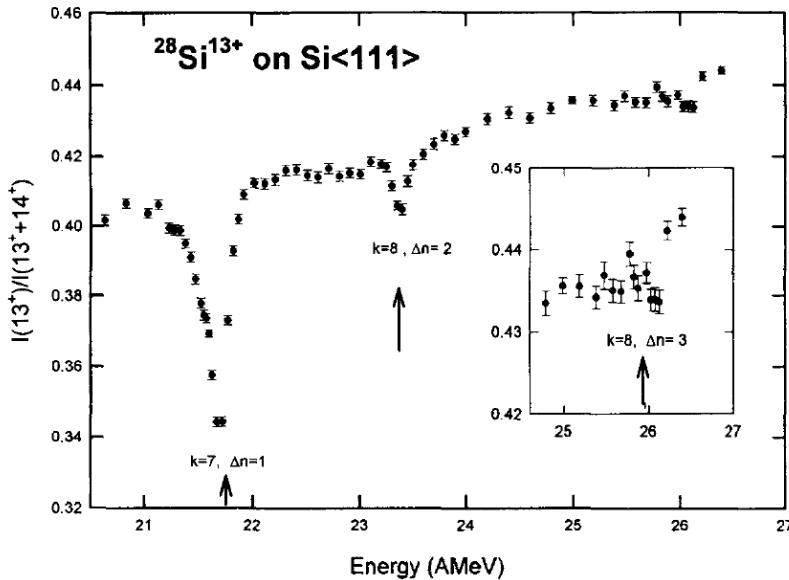


Fig. 61. Dependence on beam energy (MeV/u) of the ratio of 13+ to (13+ +14+) ions exiting from the crystal for a Si^{13+} beam incident parallel to a Si $\langle 111 \rangle$ direction. Predicted resonances are indicated by arrows. The order of the Fourier component of the $\langle 111 \rangle$ string potential is denoted by k and the change of the main quantum number of the hydrogen-like electronic state by Δn . From [Forster *et al.* 1996] and [Andersen *et al.* 1996a].

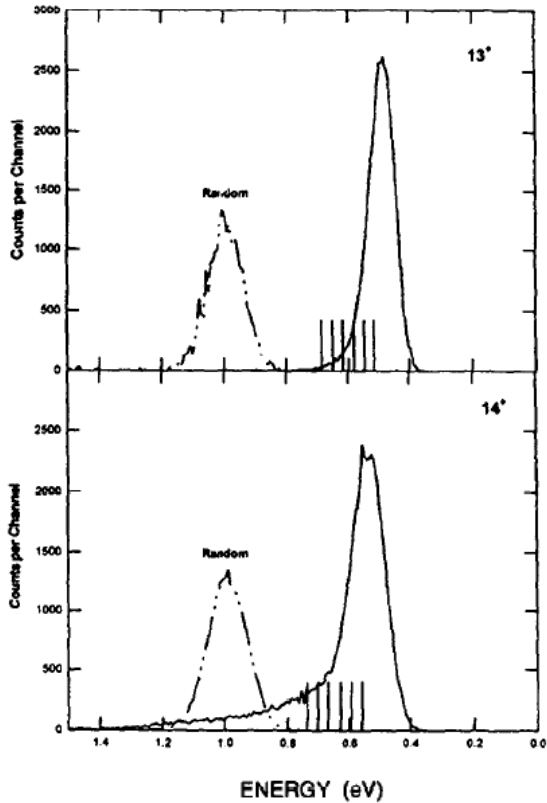


Fig. 62. Energy-loss spectra of transmitted 13+ and 14+ ions, measured simultaneously for an incident beam of 22.5 MeV/amu Si^{13+} ions. Spectra for random (---) and $\langle 111 \rangle$ aligned (—) incidence are shown together. Windows indicated by vertical lines are used in the analysis. From [Andersen *et al.* 1996a]

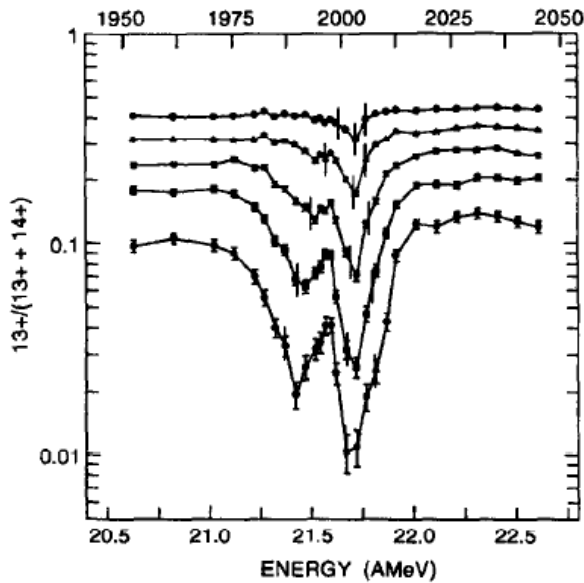


Fig. 63. As Fig. 61 but for windows on the energy loss, as shown in Fig. 62. The charge-state ratio decreases with increasing energy loss. The upper scale shows the energy of virtual photons for the $k=7$ harmonic of the $\langle 111 \rangle$ string potential. The predicted resonance position are indicated by vertical lines. From [Andersen *et al.* 1996a].

When the ions are close to a $\langle 111 \rangle$ string the transverse electric field from the string Stark-mixes the 2s and 2p states and creates hybridized 2s2p states with an energy split that increases with the field strength. With the assumption that the energy spectrum in Fig. 62 reflects the distribution in transverse energy after surface transmission, a minimum distance of approach to strings can be calculated

for the different windows. Hence the maximum transverse field experienced by the ions can be calculated, as well as the corresponding energy of the two Stark states. These energies are indicated by vertical lines in Fig. 63 and are seen to match the observation quite well. Also absolute cross sections for excitation due to absorption of virtual photons from the string field were found to be in excellent agreement with calculations. For such an analysis the Doyle-Turner potential is both accurate and very convenient since analytical expressions for Fourier components are easily obtained.

Capture and loss of electrons

As noted above, it is an important constraint in the derivation of the diffusion equation for dechanneling that a constant density in phase space should be an equilibrium. The requirement follows from basic symmetries of the multiple scattering. However, in the late nineties experiments by Assman *et al.* on transmission of heavy ion beams through thin crystals appeared to violate this rule.

The set up shown in Fig. 64 was designed to give a sensitive test of the equilibrium hypothesis for heavy ions transmitted through a thin crystal [Assmann *et al.*, 1999], [Grüner *et al.*, 2003]. By scattering of a heavy-ion beam in a thin foil, a thin Si crystal was illuminated with a beam with large angular divergence, and behind the crystal the angular distribution of the scattered ions and recoiling target atoms was measured with a position sensitive detector. An isotropic beam with

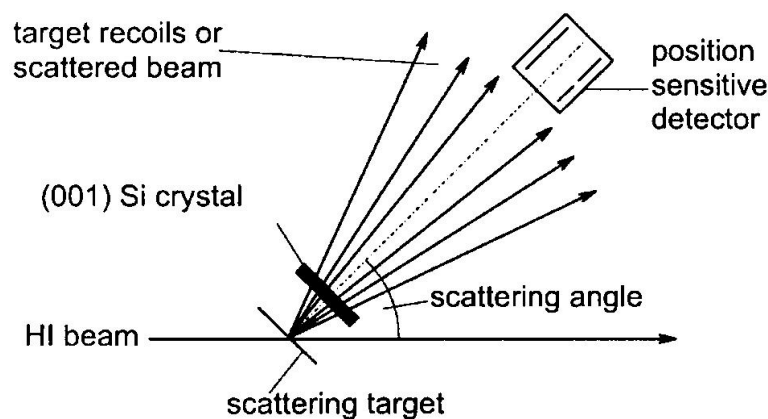


Fig. 64. Geometry for transmission experiment [Assmann *et al.* 1999]. A heavy-ion beam (HI) was incident on a thin scattering target and the angular distribution of scattered ions and target atom recoils after passage of a thin Si crystal was observed with a position sensitive detector (scale distorted).

uniform intensity gives a constant distribution in transverse phase space inside the crystal and if this distribution is stable, the beam should remain isotropic after the passage of the crystal.

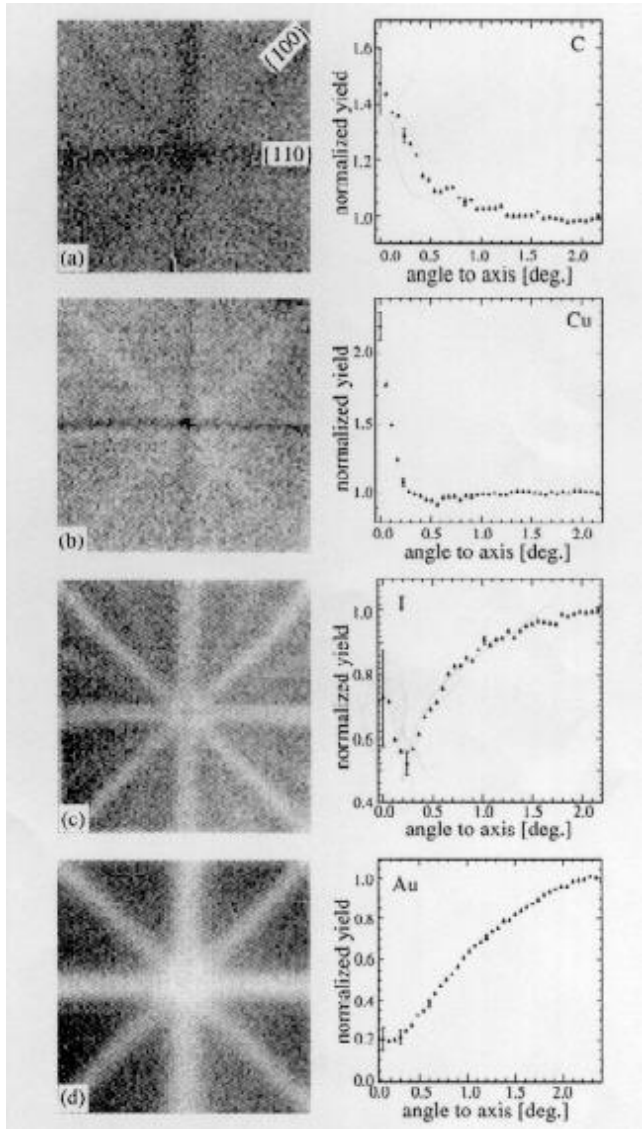


Fig. 65. Flux distributions of heavy ions after transmission through (001) Si crystal. To the right circularly averaged intensities: (a) C recoils at 18 MeV after 8.7 μm ; (b) Cu recoils at 46 MeV after 8.7 μm ; (c) scattered I ions at 121 MeV after 2.9 μm ; and (d) scattered Au ions at 92 MeV after 2.9 μm . The angular range is $\pm 2.2^\circ$ [Assmann *et al.* 1999].

The results shown in Fig. 65 are dramatically different. To the left are the two-dimensional intensity distributions and to the right the azimuthally averaged intensity as a function of the angle to the axis. For carbon ions there is a strong accumulation of flux near the axis and the planes, denoted cooling (reduction of transverse energy). The transmission of Cu ions is an intermediate case, with cooling along the axis and the strongest planes but a depletion of the flux ('heating') along the weaker planes. For transmission of the heavier iodine ions, there is almost exclusively heating, and for the heaviest Au ions there is strong heating along all channeling directions.

According to the discussion in Ch. 18 under the heading *Symmetry of scattering*, the stability of a constant distribution in transverse phase space (constant $f(E_\perp)$), as expressed in Eq. (171), can be seen as a necessary consequence of the

reversibility of ion trajectories. Hence an explanation of results shown in Fig. 65 must involve a phenomenon breaking the reversibility of trajectories. Energy loss is such a phenomenon but the effects are far too strong to be caused by energy loss. I discussed the experiments with Walter Assman at a conference and proposed that capture and loss of electrons by the penetrating ions might be responsible. For highly stripped ions only tightly bound electrons are left and the ion may be treated as a point charge. With net charge Q the effective continuum potential is proportional to Q (Eqs. (23) and (24) with $Z_1e \rightarrow Q$). Electron capture then leads to a reduction of the transverse potential energy and electron loss to an increase. If, on the average, electron capture takes place at smaller distances from strings than electron loss there will be a net cooling effect, and this is indeed predicted to be the case at very high velocities, from the known impact-parameter dependence of capture and loss in this limit.

The mechanism is illustrated in Fig. 66. A C^{6+} ion is moving away from a string with transverse energy close to 1100 eV. At the distance r_c it captures an electron and loses the transverse energy $U^{(1)}(r_c)$. Later at a distance r_l the electron is lost again and the transverse energy $U^{(1)}(r_l)$ is gained. The cycle has led to a net loss of transverse energy, i.e. to cooling.

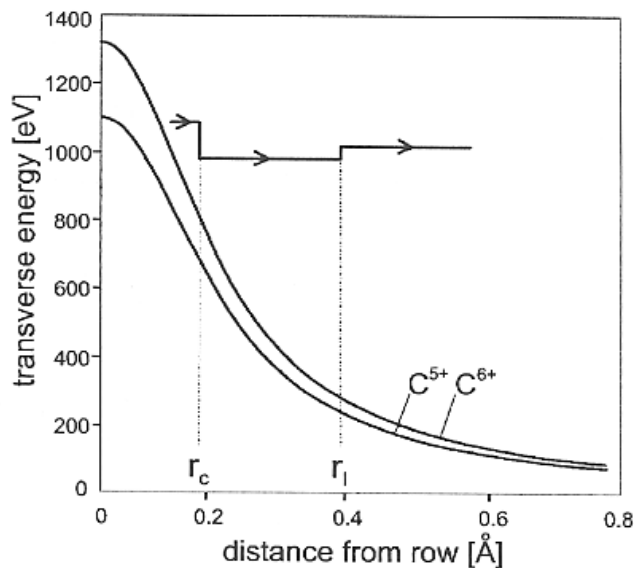


Fig. 66. $\langle 100 \rangle$ Si string potentials for C^{5+} and C^{6+} ions, in the point-charge approximation. The horizontal line indicates the transverse energy of an ion capturing an electron at r_c and losing it at r_l [Assmann *et al.* 1999].

20. APPLICATIONS OF CHANNELING AND BLOCKING

In this chapter we briefly review some of the most important applications of channeling and blocking. No doubt the studies of crystal damage after ion implantation and of the lattice location of implanted impurities have been most important, having had a major impact on the application of ion implantation in the fabrication of semiconductor electronic devices. However, although the studies of nuclear lifetimes have had limited impact on nuclear physics, some very interesting results have been obtained.

Crystal damage after implantation

The detection of crystal defects after ion implantation has probably been the most important application of channeling. For example, it has been of decisive importance in the development of ion implantation as a technique for doping of semiconductors. With backscattering of MeV beams of protons or helium ions, the crystal perfection as a function of depth can be measured, as illustrated in Fig. 67 [Feldman *et al.* 1982]. This has allowed systematic development of optimal implantation conditions and annealing procedures.

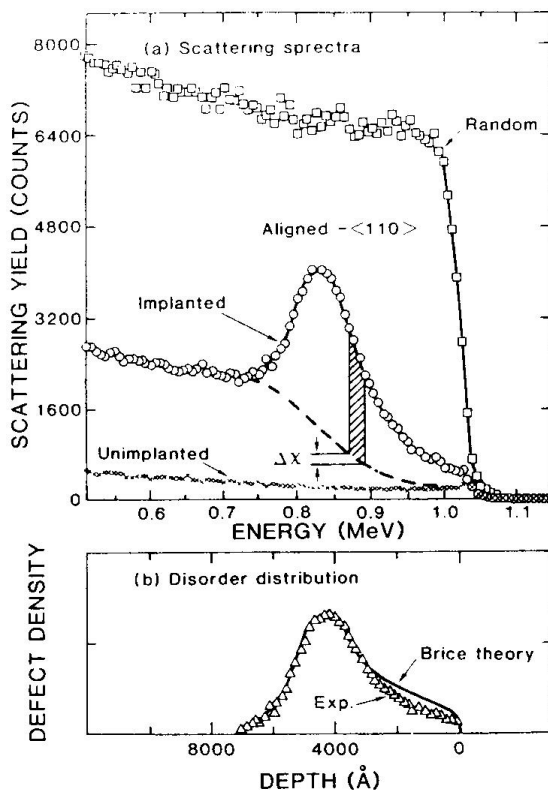


Fig. 67. Illustration of the extraction of a damage profile from backscattering of 2 MeV He ions in $\langle 110 \rangle$ aligned and random directions in Si. The energy spectrum for an undamaged crystal is compared with that from a crystal damaged by implantation. In the hatched interval the increase from dechanneling is $\Delta\chi$. From [Feldman *et al.* 1982].

The energy scale for the backscattered particles can be converted into a depth scale, as shown at the bottom. The spectrum for a beam aligned with an axis is shown for a virgin crystal as well as for an implanted crystal, and the difference in yield can be ascribed to a combination of direct backscattering from defects and increased backscattering from atoms in perfect parts of the crystal due to dechanneling. This latter part is indicated by the dashed line and when it is subtracted the depth distribution of the damage is obtained.

Methods for analysis of such spectra are today readily available and, all in all, dechanneling is a very well developed field. When dechanneling by defects is included, the diffusion equation may not be suitable. Alternative approaches are solution of a master equation, which can include large jumps in transverse energy [Gärtner *et al.* 1984], or brute force binary-collision computer simulation.

Localisation of impurities by channeling and blocking

Another important application of channeling has been the use of the strong dip in yield of a close-encounter reaction to determine the location of impurity atoms in a crystal lattice. An example is the determination of the lattice configuration of nitrogen implanted into silicon [Rasmussen and Nielsen 1994].

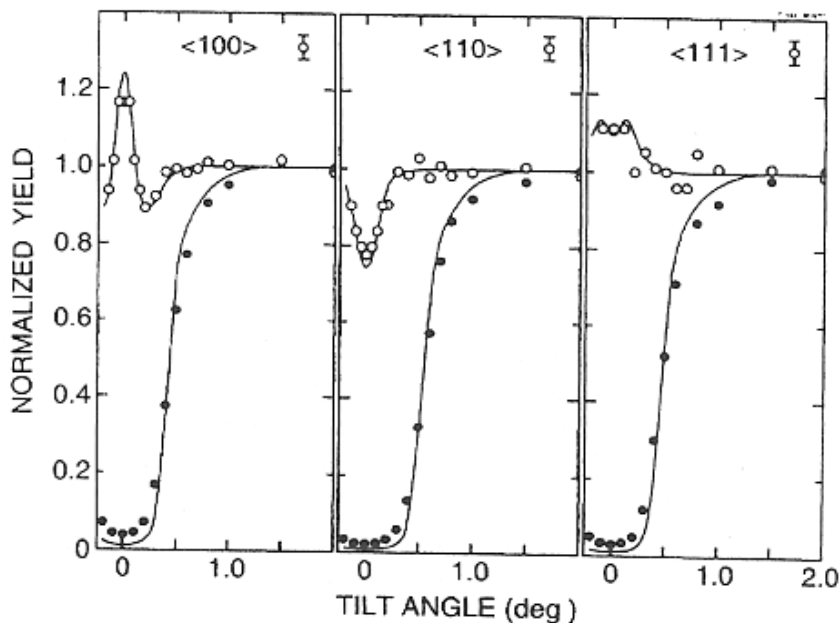


Fig. 68. Angular distributions in yield of (p,α) reaction (o) and of backscattering from Si crystal implanted with nitrogen (•). The lines are from calculations including dechanneling [Rasmussen and Nielsen 1994].

Nitrogen impurities can be detected at low concentrations by a (p,α) reaction. The observed yield of this reaction together with the backscattering yield from the Si lattice are shown in Fig. 68 for angular scans through the three major axes. The scans are averaged over the azimuthal angle whereby perturbations by planar

effects are largely eliminated. The data are consistent with the dumbbell configuration illustrated in Fig. 69. Two nitrogen atoms replace one silicon atom. The lines through the data points are from calculations for such a configuration.

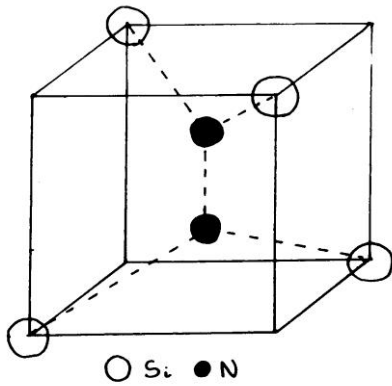
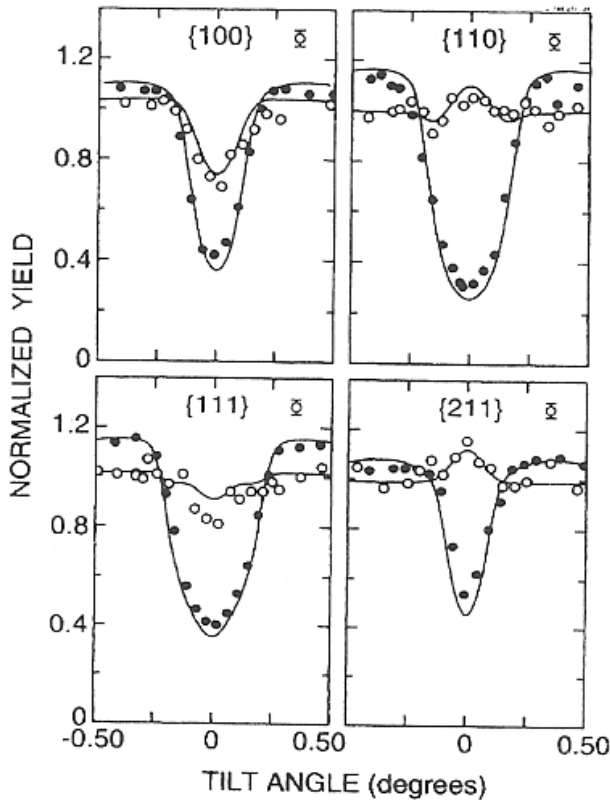


Fig. 69. Nitrogen dumbbell replacing a substitutional atom in a Si lattice (diamond structure). From [Ramussen and Nielsen 1994].

The dumbbells are oriented randomly along the three equivalent $\langle 100 \rangle$ axes (edges of cube). Nitrogen is substitutional along one axis and interstitial along the other two.



This gives a superposition of 1/3 dip and 2/3 narrow peak. An accurate potential (Doyle-Turner) has been used and dechanneling for a perfect lattice has been included. This is seen to give excellent agreement with the data, both for the impurity and for the host lattice. As seen in Fig. 70, also the observed structures for channeling along three different planes were found to be in good agreement with the simulation (planar scans sometimes give crucial information!) [Nielsen *et al.* 1988].

Fig. 70. Planar angular scans of (p, α) and backscattering yields for a nitrogen implanted Si crystal, compared with calculations including dechanneling. From [Rasmussen and Nielsen, 1994].

The equivalence of channeling and blocking implies that impurities can just as well be localised by observation of blocking dips for charged particles emitted from the impurity atoms. A very early example is an observation of a strong blocking dip for α -particles from ^{222}Rn implanted into a tungsten crystal [Domeij and Björkqvist 1965]. The measurements on electrons and positrons discussed below showed that information on lattice location can also be obtained from observation of the blocking effects for these light particles. This is very useful since beta emitting isotopes are ubiquitous in the periodic table. A pioneering effort on quantitative application of this method has been made by Hofsäss [Hofsäss 1996].

Crystal blocking for determination of nuclear lifetimes

In analogy to the lattice localisation of impurities, the blocking effect can be used to determine how far from a lattice site the emission of charged particles takes place. For a nuclear reaction proceeding by formation of a compound nucleus, one may thereby determine the average recoil distance $v_{\perp}\tau$, where v_{\perp} is the component of the compound nucleus velocity perpendicular to the axis and τ is the compound nucleus lifetime [Gibson 1975].

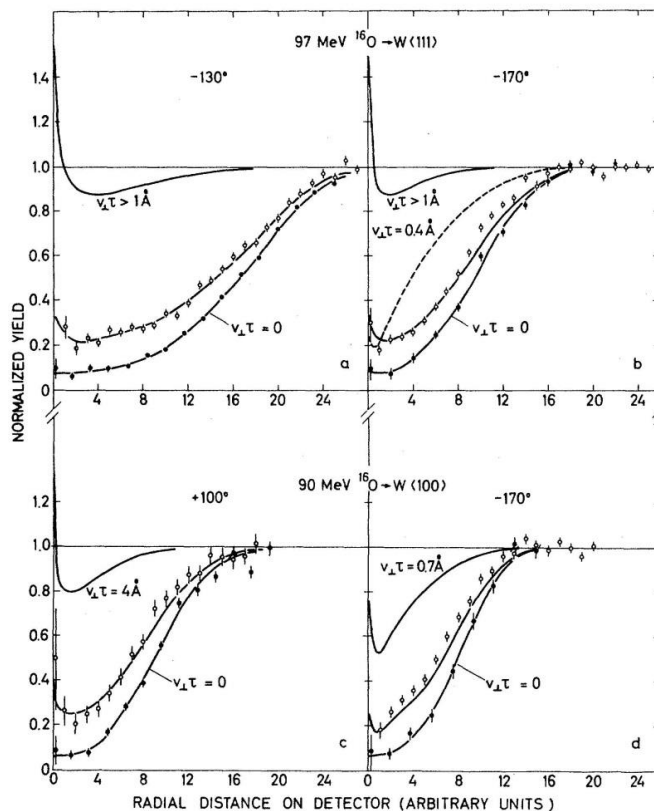


Fig. 71. Fission fragment blocking dips for $^{16}\text{O} \rightarrow \text{W}$ (o), at two bombarding energies and observed simultaneously at two different angles of the axis to the beam direction. The dips are compared with results for prompt fission (●) (lower curves), simulated by scaling the dips obtained for elastic scattering of 40-MeV ^{16}O , according to Eq. (29). The uppermost curves were calculated for an exponential decay with the average recoil distance indicated. (The dip is nearly independent of recoil distance for average recoil distances longer than 1 \AA .) The fragment dips are fitted with a combination of the dips for zero recoil and for a long recoil distance. The dashed curve shows that a single lifetime does not fit the data. [Andersen *et al.* 1976a].

Several groups have studied fission lifetimes with this technique. Since the early seventies I have been working with a group mainly from Aarhus and from the Chalk River Nuclear Laboratories in Canada on development of this technique to study heavy ion induced fission of heavy nuclei. Because the recoil is large in these reactions very short times can be measured, down to about a tenth of an attosecond. This is still very long on the nuclear time scale and times of order 10^{-21} s are expected from statistical nuclear models at the very high excitation energies just after formation of a compound nucleus.

In a series of experiments with ^{12}C , ^{16}O , and ^{19}F projectiles on thin W and Ta crystals we found results consistent with this expectation. As for the lattice-location experiments discussed above, the axial dips are integrated over the azimuthal angle to eliminate planar effects. Very little narrowing of the dips was found but there was an increase in the minimum yield compared with dips in elastic scattering. As seen in Fig. 71, the results then do not correspond to decay with a single lifetime but could be fitted with a superposition of mostly fast fission without lifetime effects and a contribution from slow fission [Andersen *et al.* 1976a]. This is consistent with the Bohr-Wheeler picture of multiple-chance fission of a compound nucleus after cooling of the nucleus by emission of a number of neutrons [Bohr and Wheeler 1939].

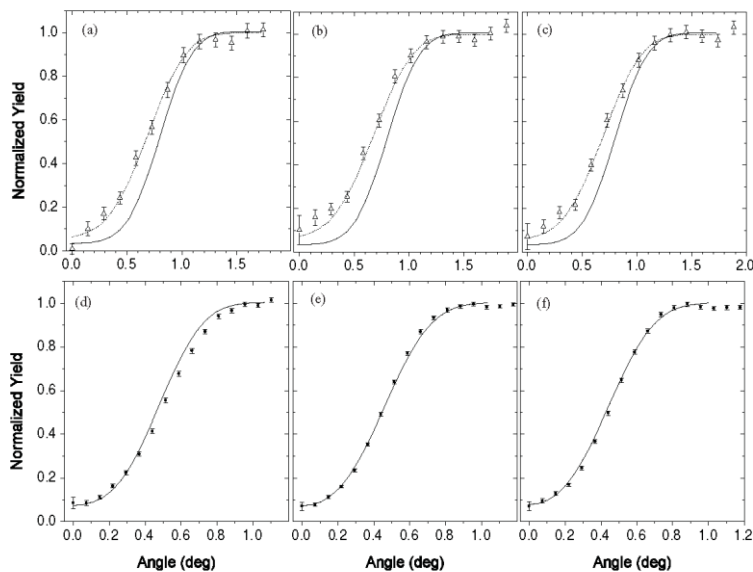


Fig. 72. Blocking dips in fission and elastic scattering for 330-MeV (a,d), 350-MeV (b,e), and 375-MeV (c,f) ^{58}Ni , compared with calculations. The dotted curves include exponential distributions of recoil displacements from a $\langle 111 \rangle$ row, with average values (a) 8 pm, (b) 9 pm, and (c) 8 pm. [Andersen *et al.* 2008].

Recently we have continued the experiments with heavier projectiles. The idea is to investigate the influence of viscosity on the nuclear mass flow at high internal temperatures. Results from other types of measurements, e.g., on the number of neutrons emitted prior to fission and on emission of giant-dipole gamma rays from the compound nucleus, have indicated that the lifetime can be rather long. The

experiments were carried out at Oak Ridge National Laboratories in the US [Andersen *et al.*, 2008]. The analysis indicates a clear narrowing of the fission dips compared with the dip in elastic scattering. This is quite exciting because the time delay must be very long on the nuclear time scale, of order 10^{-18} s, and a large fraction of the fission events must experience this delay. In Fig. 72 the results for bombardment of a thin W crystal with ^{58}Ni ions are compared with a calculated dip for an exponential decay with average displacements of about 8 pm. The elastic dips (lower half of figure) are seen to be in excellent agreement with the calculation for zero displacement, including a small increase in minimum yield ascribed to crystal defects near the interface with a Mo substrate and a correction for mosaic spread in the epitaxially grown crystals.

The fission dips in the upper half of the figure are compared with elastic dips scaled according to Eq. (29). The lifetime effect is very clear. The measured dips are in excellent agreement with dips calculated for exponential decay with average recoil about 8 pm, corresponding to a lifetime of order 1 as. The lifetime cannot be explained in the Bohr-Wheeler picture of multiple-chance fission of a compound nucleus and it is instead interpreted as a signal of very high viscosity of the nuclear mass flow in the fission process. The picture of the united nucleus must be closer to a drop of syrup than to a drop of water. These results may also be important for the interpretation of observations of long fission lifetimes for super-heavy compound nuclei created in heavy-ion reactions [Drouart *et al.* 2005]. To double check the interpretation, measurements of fission after bombardment with the same heavy-ion beams were made with the same set-up but with a thin Mo crystal as target [Andersen *et al.* 2012]. For these much lighter systems the blocking dips of fission fragments showed no narrowing but an increased minimum yield, consistent with multi-chance fission of a compound nucleus.

The observations shown above a clear demonstration of the power of the technique to determine not only average displacements but also the distribution of displacements. Fig. 72 shows that small displacements from a lattice site are most easily detected by the narrowing of the width of the blocking (or channeling) dip, rather than by the increase of the minimum yield. A similar conclusion was reached earlier from measurements of channeling dips in outer-shell xray yields [Andersen and Davies 1976]. It may also be noted that most of the analysis was performed with small computer programmes based on the standard model. (With the very small crystal thicknesses it was not necessary to include dechanneling.) Such calculations are very fast compared to blocking calculations with Monte-Carlo simulation of binary collisions.

21. ELECTRONS AND POSITRONS, CHANNELING RADIATION

Channeling of electrons and positrons was hotly debated in the late sixties and early seventies. As discussed in Ch. 2, the transmission of these light particles through thin crystals is typically dominated by diffraction effects like Bragg scattering. There are two reasons for this: Firstly, the ratio of the Bragg angle in Eq. (2) to the characteristic angle for scattering in Eq. (29) (with E replaced by $\frac{1}{2}pv$) is given by

$$\frac{\theta_B}{\psi_1} = \frac{\pi}{2} (Z_1 Z_2)^{-1/2} \left(\frac{a_0}{d}\right)^{1/2} \left(\frac{M_1}{m_0}\right)^{-1/2}, \quad (196)$$

where m_0 is the electron rest mass and a_0 is the radius of the hydrogen atom, $a_0 = 0.529 \text{ \AA}$. This ratio is very small for particles heavy compared with the electron. But for electrons we should use $Z_1=1$ and the relativistic factor γ instead of the mass ratio in the last factor in Eq. (196). Except for very large values of γ the ratio is then close to unity. Secondly, for fixed energy the velocity is high for these light particles and the mean free path for inelastic scattering can be long so that interference phenomena are not quickly destroyed by incoherence.

While channeling phenomena for positrons are expected to be qualitatively similar to those for protons, apart from interference effects, they must be very different for electrons. Correlated scattering on atoms in a row does not deflect an electron and thereby prevent close encounters with atoms but instead attracts the particle and enhances the probability of such encounters. This also enhances the inelastic scattering, and electron channeling phenomena are therefore less stable.

The essentially classical features of blocking of electrons and positrons were demonstrated by Uggerhøj by observation of the emission of both particles from

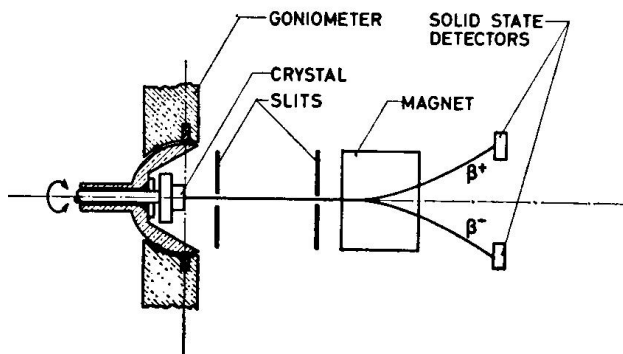


Fig. 73. Set-up for observation of the emission of electrons and positrons from ^{64}Cu implanted into a copper crystal. From [Uggerhøj and Andersen 1968].

radioactive ^{64}Cu implanted into a copper crystal [Uggerhøj 1966]. The beautifully simple experiment is illustrated in Figs. 73 and 74. The crystal is mounted in a goniometer, and two collimators determine the emission direction for both

electrons and positrons. As shown in Fig. 74, there is a strong decrease in yield along the axis for positrons, similar to observations for heavier particles like alpha particles. In contrast, there is a strong increase in the yield of electrons, as would be expected classically from the reversed sign of the interaction with string atoms.

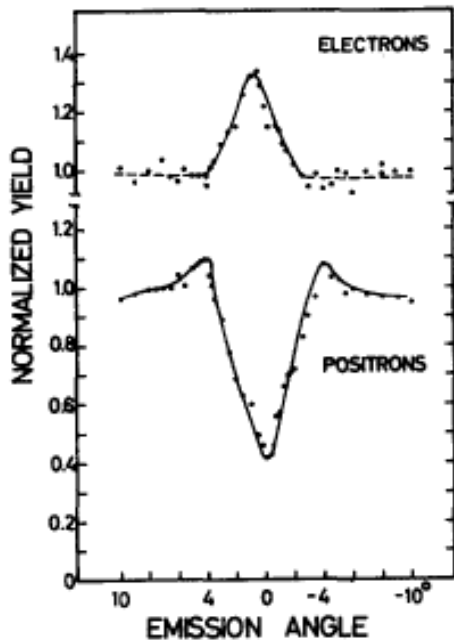


Fig. 74. Emission yield of positrons and electrons from ^{64}Cu versus angle between emission direction and a $\langle 100 \rangle$ axis in a Cu crystal. The energy of the positrons and electrons were 200-300 keV and 150-250 keV, respectively. From [Uggerhøj 1966].

The results of continued measurements are shown in Fig. 75. The comparison with classical calculations in the standard model confirms the classical nature of these effects. The deviations are partly due to crystal defects created by the implantation.

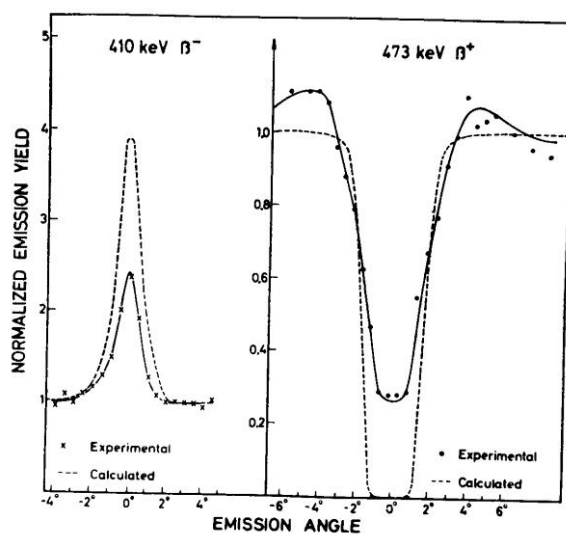


Fig. 75. Observed yields along a $\langle 100 \rangle$ axis in Cu from electron and positron emission by implanted ^{64}Cu . The measurements are compared with continuum model calculations. From [Uggerhøj and Andersen 1968].

The classical interpretation of these experiments was criticised and it was argued that, as known from electron microscopy, the transmission of electrons through thin crystals is dominated by coherent Bragg reflection. However, it was soon

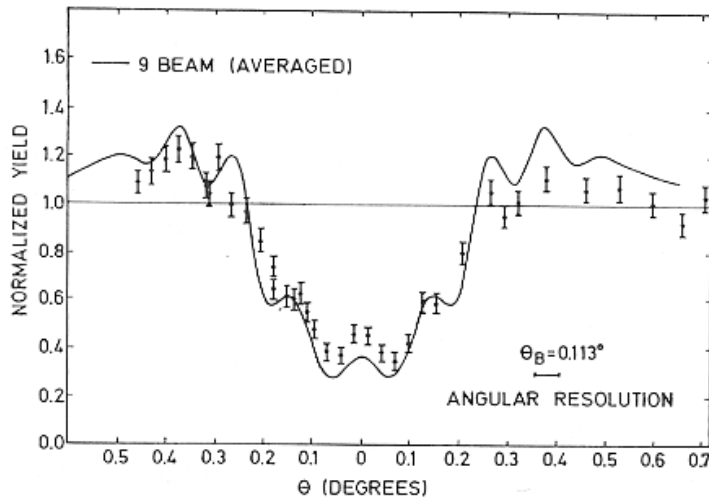


Fig. 76. Wide-angle scattering near a {110} plane for 1.2 MeV positrons in Si, compared with a many-beam calculation. From [Pedersen *et al.* 1972].

realised that this quantisation of transverse momentum does not in itself imply the absence of strong classical features. The decisive question is whether the localisation of an electron to move close to a string or plane gives too much spread in direction of motion via the uncertainty principle to allow a classical description by orbital pictures. This is determined by the number of bound states in the transverse motion, which becomes large for relativistic electrons [Andersen *et al.* 1977].

The phase space for bound states in a planar potential is larger for positrons, which oscillate in the open space between planes, and hence channeling is more classical for positrons than for electrons. I worked at Bell Labs in the US at the time, and together with Augustyniak I set up an experiment with positrons from a radioactive source mounted in the ion source of an old 1 MV Van der Graaf. Fig. 76 shows a comparison between a measured planar dip in yield of wide angle scattering for 1.2 MeV positrons and a so-called many-beam quantum calculation [Pedersen *et al.* 1972]. The dip has an essentially classical envelope with fine structure from Bragg interference. In a many-beam calculation the positron is represented by a wave function that inside the crystal is a superposition of plane waves. The energy eigenstates are determined from diagonalisation of the Hamiltonian in a space spanned by a number of these plane waves (“beams”), with wave vectors differing by reciprocal lattice vectors. The population of the eigenstates is determined by matching at the surface to the incident plane wave.

Channeling radiation. For the history of channeling radiation, see the review [Andersen *et al.* 1983]. The discovery of channeling radiation should be accredited mainly to Kumakhov who was the first to derive the correct relativistic transformation [Kumakhov 1976]. The simplest way is to consider first the emission of radiation in the so-called rest system following the electron (or positron) motion along a string or plane, and then make a Doppler transformation to the laboratory system. In the rest system, both terms in the Hamiltonian, the kinetic energy and the potential, are multiplied by a factor γ and hence the energy eigenvalues are larger by this factor. The Doppler transformation of the radiation back to the lab system gives a factor $(1+\beta)\gamma$ in the forward direction. The outcome is that the Bohr relation between the photon frequency and the electron energy jump is modified by a relativistic factor of $\sim 2\gamma^2$ for emission in the forward direction.

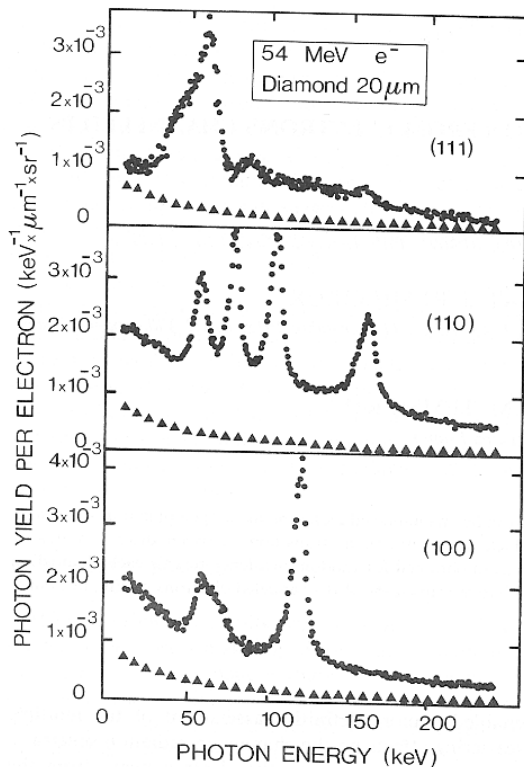


Fig. 77. Photon spectra in the beam direction for 54 MeV electrons along different planes in diamond. Triangles show spectrum for incidence in a random direction. From [Guanere *et al.* 1982].

A line spectrum of planar channeling radiation was first presented by the Livermore group at the ICACS conference in Hamilton, Canada, 1979 [Alguard *et al.* 1980]. Shortly afterwards we observed in Aarhus the first line spectra for axially channeled electrons [Andersen and Lægsgaard 1980]. A spectrum of channeling radiation from electrons in diamond is shown in Fig. 77. The lines are particularly sharp in this material because of the low Z_2 and very small thermal vibrations which lead to weak incoherent scattering and a long lifetime of channeling states.

An important question in the early phase was the relation to the well-known coherent bremsstrahlung in crystals, closely related to Bragg interference [Andersen 1980], [Andersen *et al.* 1981]. This radiation can be thought of as transitions between free (unbound) states of motion, induced by the periodic passage of crystal planes (Fig. 81). Also transitions from free to bound states can be observed (Figs. 78 and 82).

For not too high energies (MeV) a quantum treatment must be applied, and a systematic description can be based on the formalism developed by Lindhard and co-workers [Lervig *et al.* 1967], and further extended by [Andersen *et al.* 1983], [Andersen *et al.* 1985]. Spin effects are not important except for very high energies m_0 in a system with total energy E may be used as a starting point,

$$\left\{ \left[-i\hbar\nabla + \frac{e}{c}\mathbf{A}(\mathbf{R}) \right]^2 c^2 + m_0^2 c^4 \right\} \psi(\mathbf{R}, \dots) = [E - H_{\text{rad}} - H_{\text{lat}} - V(\mathbf{R}, \dots)]^2 \psi(\mathbf{R}, \dots) \quad (197)$$

Here the terms H_{rad} and H_{lat} are the independent Hamiltonians of the radiation field and the crystal, while \mathbf{A} represents the vector potential of the radiation field. The trick is now to separate off a phase factor corresponding to the total momentum and not just to its z component,

$$\psi(\mathbf{R}, \dots) = e^{iKz} w(\mathbf{r}, z, \dots), \quad \text{with } \hbar^2 K^2 c^2 + m_0^2 c^4 = E^2. \quad (198)$$

This gives an approximate equation of first order in the time-like parameter $t = z/v$. Neglecting terms of second order, like $\frac{\partial^2}{\partial z^2}$ and V^2 , we obtain

$$i\hbar v \frac{\partial}{\partial z} w = \left[-\frac{\hbar^2}{2\gamma m_0} \Delta_r + V(\mathbf{r}, z, \dots) + H_{\text{rad}} + H_{\text{lat}} + H_{\text{e,r}} \right] w(\mathbf{r}, z, \dots), \quad (199)$$

$$H_{\text{e,r}} = e \left(\beta A_z + \frac{1}{\gamma m_0 c} \mathbf{A} \cdot \mathbf{p} \right).$$

The equation has the form of a non-relativistic Schrödinger equation in two dimensions, and the wave function describes the transverse channeling state. The operator $H_{\text{e,r}}$ represents the interaction of the particle with the radiation field. It can be treated as a perturbation and also the interaction with the lattice can be simplified by a series of perturbation approximations. The electronic excitations are treated by a replacement of V by its expectation value $\langle V \rangle_e$ in the electronic ground state and a perturbation calculation of the inelastic transitions induced by the difference $V - \langle V \rangle_e$. Similarly, vibrational excitations of the lattice are treated

by the introduction of a thermally averaged potential, with Fourier components reduced by a Debye-Waller factor, $\langle V \rangle_e = \langle V \rangle_{e,T} + (\langle V \rangle_e - \langle V \rangle_{e,T})$. To first order, the last term induces transitions between vibrational lattice states and to second order, the combination of this term with the coupling $H_{e,r}$ induces normal incoherent Bremsstrahlung.

In a final step, the thermally averaged potential is approximated by the axial or planar continuum potential. Also here there are terms left out, causing so-called non-systematic reflections that are usually not very important. For a particle moving at a fairly large angle to a plane also the continuum potential can be treated as a perturbation (classical trajectory **b** in Fig. 78). In this approach, the basic quantum states are plane waves and the radiation from free-to-free transitions (Fig. 81) is obtained to second order from a combination of this perturbation with the radiation coupling $H_{e,r}$. This is analogous to the calculation of incoherent Bremsstrahlung and the radiation is normally called coherent Bremsstrahlung [Andersen *et al.* 1981].

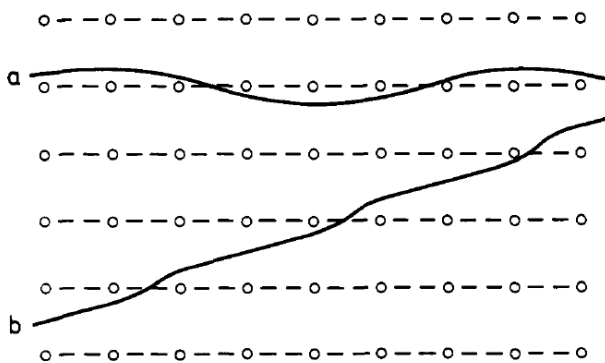


Fig. 78. Qualitative illustration of classical electron trajectories in crystal lattice, **a** for a bound state in the planar continuum potential and **b** for an electron moving at a larger angle to the planes. The angles to the planes have been much exaggerated for both cases. (From [Andersen *et al.* 1981].

Measurements of axial channeling radiation are shown in Fig. 79. The states are two-dimensional, as from a 2D hydrogen atom, and can be classified as usual by a main quantum number and a letter giving the angular momentum L , i.e. s, p, d etc. The selection rule is $\Delta L=1$ and four lines are clearly distinguished, corresponding to 2s-2p, 3d-2p, 2p-1s, and 3p-1s transitions. The angular dependence of the intensities reflects the overlap of the incoming plane wave with the initial states of the transitions, i.e., the intensity is proportional to the square of a Fourier component of the transverse wave function. The ridges at larger angles are from free-to-bound transitions (see below).

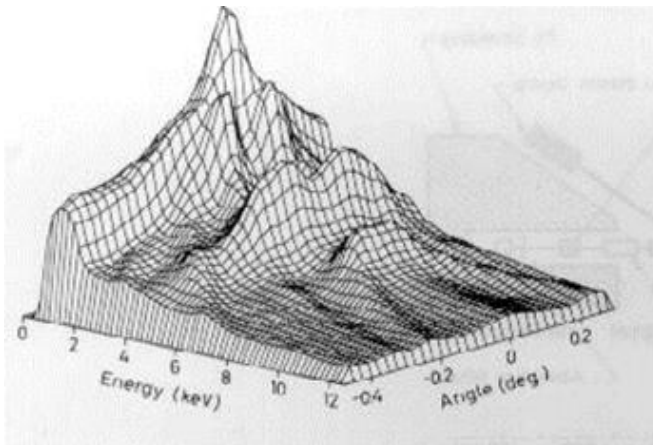


Fig. 79. Photon spectra in the forward direction vs angle of incidence to a $\langle 111 \rangle$ axis for 4 MeV electrons in a $0.5 \mu\text{m}$ thick Si crystal. From [Andersen *et al.* 1982].

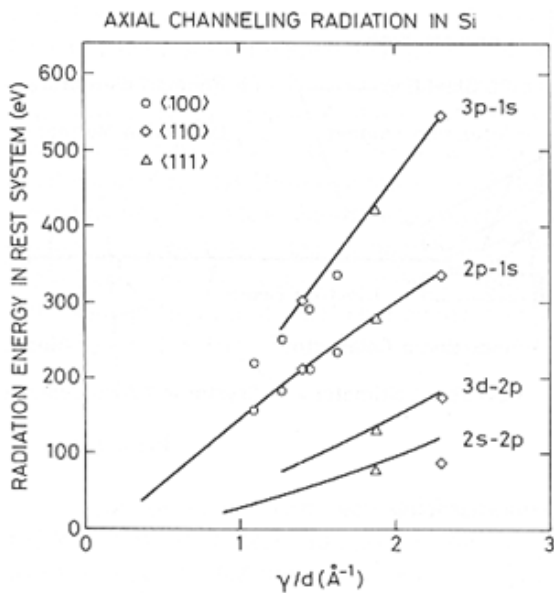


Fig. 80. Comparison between calculated transition energies in the rest frame and measurements, at varying electron total energy, $E = \gamma mc^2$, and for axes with different atomic spacing, d . A Doyle-Turner potential was used in the calculations. From [Andersen *et al.* 1982].

There is a general background of incoherent Bremsstrahlung with intensity approximately proportional to the reciprocal of the photon energy. The intensity of this radiation is also affected by the channeling because it is proportional to the overlap of the particle wave function with the atoms. It is a close-encounter process just like wide-angle scattering. The enhancement is seen at the highest energies in Fig. 79 as a ridge at zero angle to the axis where the s-states have their maximum population.

Radiative transitions between the bound levels give photon energies in the direction of the axis equal to $h\nu \cong 2\gamma\Delta E_R$, where E_R is the energy level in the reference system moving with the particle in the z -direction, the so-called rest system. As mentioned above, the mass is here non-relativistic and the kinetic

energy term in the Hamiltonian is increased by a factor γ . Also the potential is multiplied by a factor γ due to the Lorentz contraction of the spacing, d , of atoms on the string, so the Hamiltonian is just multiplied by the factor γ .

The measurements are in Fig. 80 seen to be reproduced quite well by calculations. Transitions along three different axes are included. The single-string potential in the rest frame scales with γ/d and hence measurements for channeling along three different axes can be included in one graph with scaled units.

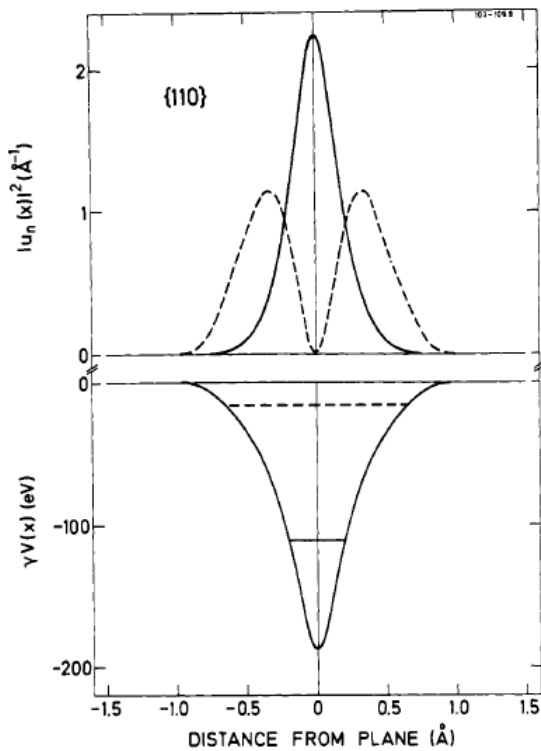


Fig. 81. Potential in rest system, energy levels, and intensity distributions in the two bound states for 4 MeV electrons channelled along a $\{110\}$ plane in Si. From [Andersen *et al.* 1981].

There are fewer bound states in planar channeling, as illustrated in Fig. 81 for 4 MeV electrons along a $\{110\}$ plane in Si.

In Fig. 82 the band structure of energy eigenstates is shown for the three major planes, reduced to the first one-dimensional Brillouin zone. Possible radiative transitions are free-to-free (coherent Bremsstrahlung), bound-to-bound, and also free-to-bound.

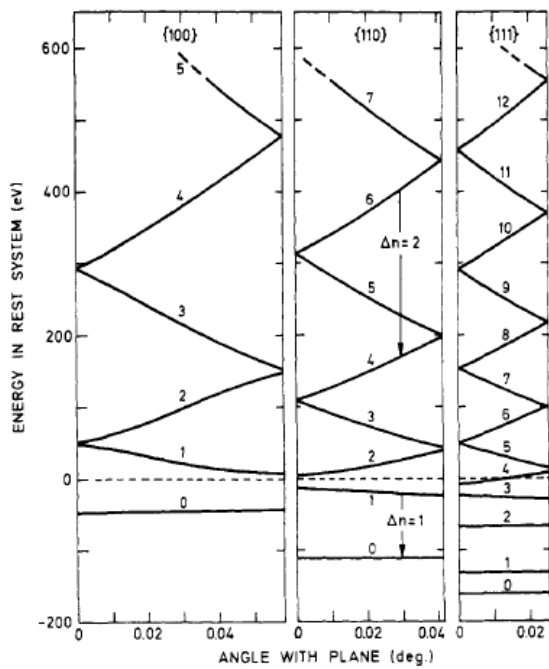


Fig. 82. Band structure of energy eigenstates in the rest system of 4 MeV electrons transmitted through a Si crystal nearly parallel to major planes. The main quantum number n is indicated, and a free-to-free transition and a bound-to-bound transition are shown. From [Andersen *et al.* 1981].

A two-dimensional display of the radiation spectrum for incidence near a {110} plane is shown in Fig. 83. The energy of the bound-to-bound transition at about 1.6 keV is nearly independent of the incidence angle. As for the axial case, the

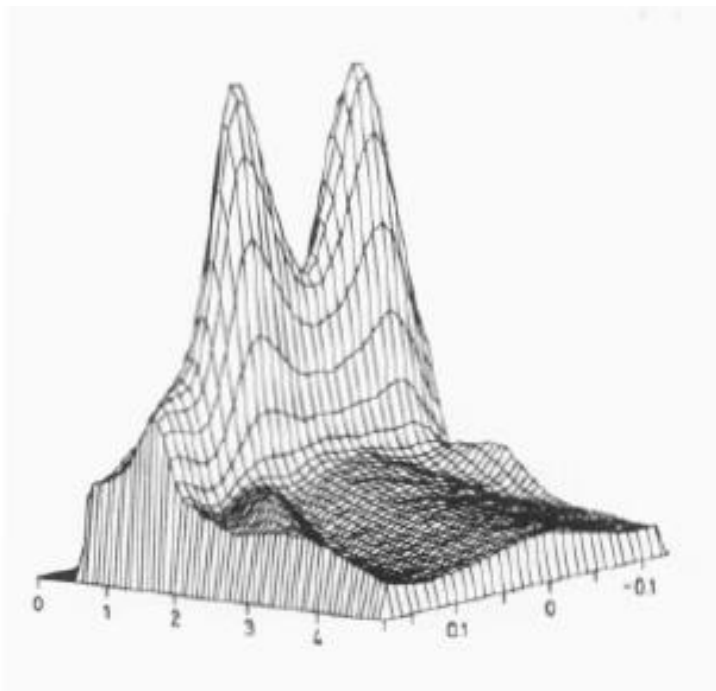


Fig. 83. Two-dimensional plot of a series of energy spectra for a variation of the incidence angle of a 4 MeV e^- beam in steps of 0.01° . The scan crosses a {110} plane in a $0.47 \mu\text{m}$ thick Si crystal. The scale to the left is the photon energy in keV, and to the right the incidence angle to the plane in deg. From [Andersen *et al.* 1981].

intensity is proportional to the population of the first excited state which is determined by the overlap with the incident plane wave, i.e. proportional to the square of a Fourier component of the wave function corresponding to the transverse component of the k -vector of the incident wave. The wave function has odd symmetry and its square is shown in Fig. 81.

The ridges at 3-4 keV at the extreme angles in the figure are due to free-to-bound transitions to the ground state (see Fig. 82). As in Fig. 79, there is at zero angle to the plane an enhancement of the incoherent Bremsstrahlung that is due to an enhanced probability of close collisions with atoms. Here it is mainly due to population of the ground state (Fig. 81).

Also the width of the lines, due to incoherent thermal and electronic scattering and to finite crystal thickness, has been studied in detail [Andersen *et al.* 1983a], [Hau and Andersen 1993]. Fig. 84 illustrates the temperature dependence of the thermally averaged planar potential for a $\{111\}$ plane in Ni (fcc crystal) and of the transition energy for the $1 \rightarrow 0$ transition.

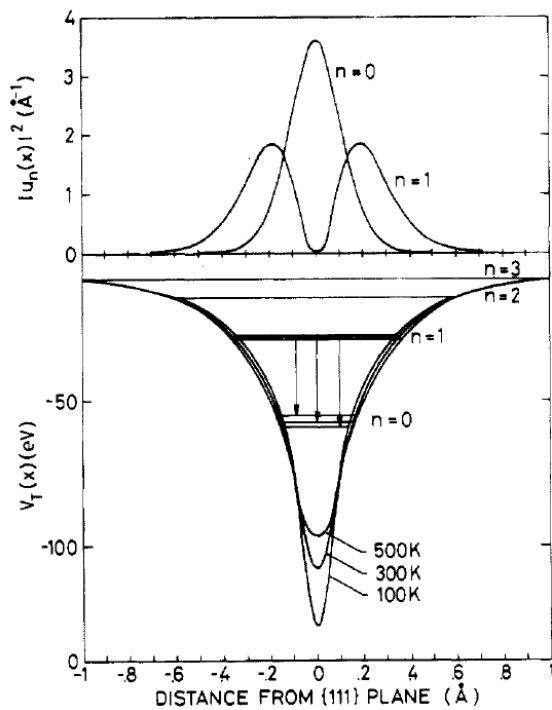


Fig. 84. Thermally averaged planar potential for $\{111\}$ plane in Ni at three different temperatures. The lowest four energy levels for channelled 4 MeV electrons are shown as well as the square of the wave function for the lowest two states (top). The arrows indicate the $1 \rightarrow 0$ radiative transition at the three temperatures. From [Andersen *et al.* 1983].

The energy spectra of radiation in the forward direction shown in Fig. 85 confirm the predicted shift with temperature of the $1 \rightarrow 0$ line near 4 keV. The width of the line is mainly due to thermal incoherent scattering, limiting the lifetime of the channeling states, and hence increases with temperature.

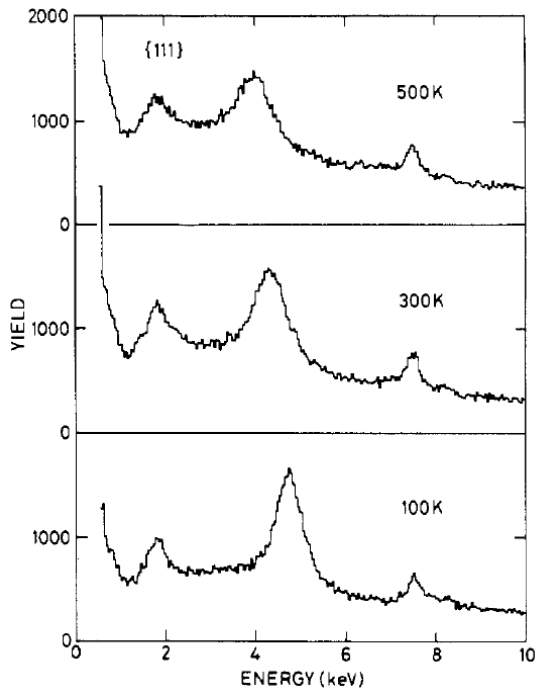


Fig. 85. Radiation spectrum in the forward direction for 4 MeV electrons incident parallel to a $\{111\}$ plane on a thin Ni crystal at three different temperatures. The line near 4 keV is from the $1 \rightarrow 0$ transition indicated by arrows in Fig. 83. The small peak just below 8 keV is from characteristic Ni K-xrays. From [Andersen *et al.* 1983a].

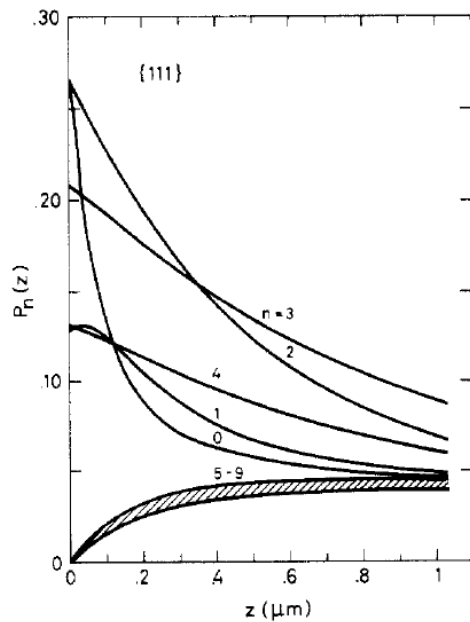


Fig. 86. Depth dependence of the population of channeling states for 4 MeV electrons incident at half the Bragg angle (Eq. (1)) to a $\{111\}$ plane in Ni. The curves are solutions to the master equation, Eq. (155A), with transition probabilities calculated from incoherent thermal scattering. Only the five lowest states have a significant population at the surface. From [Andersen *et al.* 1983a].

The change with depth populations of channeling states, illustrated in Fig. 86, is also dominated by thermal scattering and it can be calculated by solution of the master equation in Eq. (155a). The transition probabilities are proportional to the square of a matrix element of the perturbation $(\langle V \rangle_e - \langle V \rangle_{e,T})$, as mentioned in the discussion of Eq. (199). Compared with multiple scattering for positive particles,

the depth dependence is quite strong, in particular for the states with even n which have high probability density at the atomic planes (Fig. 84).

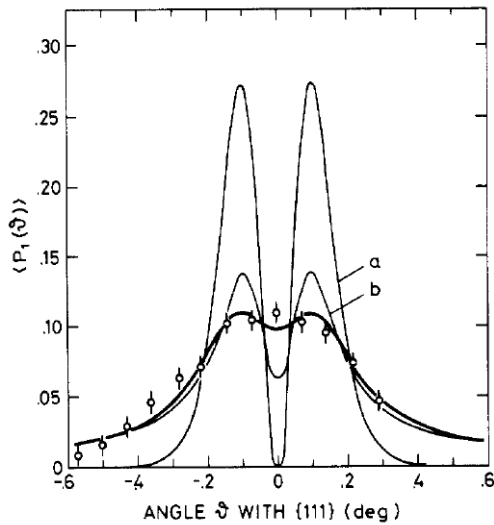


Fig. 87. Average population of the $n=1$ state through a $0.5 \mu\text{m}$ thick Ni crystal, derived from the measured intensity of the $1 \rightarrow 0$ line. The thin-line curves correspond to the population at the surface (a) and the average population obtained from the thermal scattering illustrated in Fig. 85 (b). The thick-line curve includes an average over incidence angles corresponding to the mosaic spread of crystallite orientations in the epitaxially grown thin crystal. From [Andersen *et al.* 1983a].

The calculation of multiple scattering can be tested by a comparison of the measured intensity of the $1 \rightarrow 0$ radiation with calculations, as shown in Fig. 87. When the mosaic spread in the crystal is taken into account the agreement is excellent.

As suggested by the results illustrated above, observation of channeling radiation combined with perturbation calculations can give quite accurate information about crystal properties like thermal vibrations [Datz *et al.* 1986], [Hau *et al.* 1990] and electron densities [Andersen *et al.* 1982a]. However, after a hectic period in the 1980s with many active groups, in both theory and experiments, the activity in low-energy channeling radiation has subsided, and today it is rare to see a paper in this field. Perhaps the field is too well established. Also, the early promises of application of MeV electron beams in crystals as a radiation source seem not to have materialised.

In contrast, there has been a continued interest in radiation phenomena in crystals for high-energy electrons (GeV) [Sørensen and Uggerhøj 1987]. The physics in this region is very different, with essentially classical motion of the electrons, and also other processes like creation of particle-antiparticle pairs have been studied. Like the Bethe-Heitler spectrum of incoherent Bremsstrahlung for a random medium, the radiation spectrum extends up to the kinetic energy of the particle, and the photon yield can be very strongly enhanced. The production of hard photons is an interesting application for particle physics. The effective electrical field generating the radiation corresponds to the continuum potential in the rest system, and since

it is proportional to the relativistic factor γ it becomes huge at extreme relativistic energies. This opens up for fundamental studies in strong-field electrodynamics [Uggerhøj 2005]. As a more practical application, the strong electric field from strings or planes can also be used to bend high-energy beams by transmission through curved crystals [Bak *et al.* 1980].

REFERENCES

M.J. Alguard, R.L. Swent, R.H. Pantell, S. Datz, J.H. Barrett, B.L. Berman, and S.D. Bloom, *Radiation from Channeled Leptons*. Nucl. Instrum. Methods 170, 7-13 (1980).

J.U. Andersen, J.A. Davies, K.O. Nielsen, and S.L. Andersen, *An Experimental Study of the Orientation Dependence of (p,γ) Yields in Monocrystalline Aluminium*. Nucl. Instrum. Methods **38**, 210 (1965).

J.U. Andersen, *Axial and Planar Dips in Reaction Yield for Energetic Ions in Crystal Lattice*. K. Dan. Vidensk. Selsk. Mat. Fys. Medd. **36** No 7 (1967).

J.U. Andersen and E. Uggerhøj, *Investigation of the Energy and Temperature Dependence of the String Effect*. Can. J. Phys. **46**, 517 (1968).

J.U. Andersen and L.C. Feldman, *Comparison of Average-Potential Models and Binary-Collision Models of Axial Channeling and Blocking*. Phys. Rev. B **1**, 2063 (1970).

J.U. Andersen, O. Andreasen, J.A. Davies, and E. Uggerhøj, *The Use of Channeling-Effect Techniques to Locate Interstitial Foreign Atoms in Silicon*. Radiat. Eff. **7**, 25 (1971).

J.U. Andersen and E. Lægsgaard, *Critical Angles for Axial Channeling*. Radiat. Eff. **12**, 3 (1972).

J.U. Andersen and J.A. Davies, *Channeling Dips for Outer-Shell X-ray Yields*. Nucl. Instrum. Methods **132**, 179 (1976).

J.U. Andersen, E. Lægsgaard, K.O. Nielsen, W.M. Gibson, J.S. Forster, I.V. Mitchell, and D. Ward, *Time Evolution of Heavy-Ion-Induced Fission Studied by Crystal Blocking*. Phys. Rev. Lett. **36**, 1539-1542 (1976a).

J.U. Andersen, S.K. Andersen, and W.M. Augustyniak, *Electron Channeling*. K. Dan. Vidensk. Selsk. Mat. Fys. Medd. **39** No 281 (1977).

J.U. Andersen and E. Laegsgaard: *Characteristic Radiation from Channeled Electrons*. Phys. Rev. Lett. **44**, 1079-82 (1980).

- J.U. Andersen, *Channeling Radiation and Coherent Bremsstrahlung*. Nucl.Instr. Meth. **170**, 1-5 (1980).
- J.U. Andersen, K.R. Eriksen, and E. Laegsgaard: *Planar-Channeling Radiation and Coherent Bremsstrahlung*. Physica Scripta **24**, 588-600 (1981).
- J.U. Andersen, E. Bonderup, E. Lægsgaard, B.B. Marsh, and A.H. Sørensen, *Axial Channeling Radiation from MeV Electrons*. Nucl. Instrum. Methods **194**, 209-224 (1982).
- J.U. Andersen, S. Datz, E. Lægsgaard, J.P.F. Sellschop, and A.H. Sørensen, *Radiation from Two-Dimensional "Molecular" Bound States of Electrons Channelled in Diamond*. Phys. Rev. Lett. **49**, 215 (1982a).
- J.U. Andersen, E. Bonderup, and R.H. Pantell, *Channeling Radiation*. Ann. Rev. Nucl. Part. Sci. **33**, 453 (1983).
- J.U. Andersen, E. Bonderup, E. Lægsgaard, and A.H. Sørensen, *Incoherent Scattering of Electrons and Linewidth of Planar-Channeling Radiation*. Phys. Scripta **28**, 308 (1983a).
- J.U. Andersen, E. Bonderup, and E. Laegsgaard: 6. *Channeling Radiation-Quantum Theory*. Topics in Current Phys. **38**, 127-164 (1985).
- J.U. Andersen, *Semiclassical Description of Scattering by Atoms and by Atomic Strings* in: *Semiclassical Descriptions of Atomic and Nuclear Collisions*, eds. J. Bang and J. de Boer (Elsevier Science Publishers B.V., 1985) p. 463.
- J.U. Andersen, J. Bak, and E. Bonderup, *Planar Dechanneling*. Nucl. Instrum. Methods **33**, 34 (1988).
- J.U. Andersen and A. Uguzzoni, *A Restricted Equilibrium in Phase Space for Axial Channeling*. Nucl. Instr. Methods in Phys. Res. **B48**, 181 (1990).
- J.U. Andersen, V.A. Ryabov, A. Uguzzoni and E. Fuschini, *Kinetic Equation Approach in Surface Transmission for Axial Channeling*. Nucl. Instr. Meth. B **90**, 156-160 (1994).
- J.U. Andersen, J. Chevallier, G.C. Ball, W.G. Davies, J.S. Forster, J.S. Geiger, J.A. Davies, H. Geissel, and E.P. Kanter, *Dielectronic Recombination and*

Energy Loss for He-like ^{79}Br Ions Channeled in a Thin Single Crystal of Si. Phys. Rev. A **54**, 624-635 (1996).

J.U. Andersen, G.C. Ball, J. Chevallier, J.A. Davies, W.G. Davies, J.S. Forster, J.S. Geiger, and H. Geissel, *Heavy Ion Channeling.* Nucl. Instr. Meth. B **119**, 292 (1996a).

J.U. Andersen, J. Chevallier, J.S. Forster, S.A. Karamian, C.R. Vane, J.R. Beene, A. Galindo-Uribarri, J. Gomez del Campo, C.J. Gross, H.F. Krause, E. Padilla-Rodal, D. Radford, C. Broude, F. Malaguti, and A. Uguzzoni, *Attosecond Lifetimes in Heavy-Ion Induced Fission Measured by Crystal Blocking.* Phys. Rev. C **78**, 064609 (2008).

J.U. Andersen, J. Chevallier, J.S. Forster, S.A. Karamian, C.R. Vane, J.R. Beene, C.J. Gross, H.F. Krause, J.F. Liang, D. Shapira, A. Uguzzoni, *Time Delays in Heavy-Ion-Induced Fission of Medium-Z Nuclei, Measured by Crystal Blocking.* Phys. Rev. C **85**, 044604 (2012).

B.R. Appleton, C. Erginsoy, and W.M. Gibson, *Channeling Effects in the Energy Loss of 3-11 MeV Protons in Silicon and Germanium Single Crystals.* Phys. Rev. **161**, 330 (1967).

D.D. Armstrong, W.M. Gibson, and H.E. Wegner, *Proton Channeling Studies in Thin Crystals with a Supercollimated Beam.* Rad. Effects **11**, 241 (1971).

J. Bak, G. Melchart, E. Uggerhøj, S.P. Møller, H. Nielsen, G. Petersen, H. Schiøtt, J.J. Grob, and P. Siffert, *Bending of High Energy Beams Using Axial and Planar Channeling.* Phys. Lett. B **93**, 505 (1980).

J.F. Bak, G. Melchart, S.P. Møller *et al.*, *Measurement of Average Electron Densities in Si and Ge Using MeV δ -Rays Produced by Channeled High-Energy Projectiles.* Nucl. Phys. **A389**, 533 (1982).

J.H. Barrett, *Monte Carlo Calculations of Channeling.* Phys. Rev. **B3**, 1527 (1971).

J.H. Barrett, *Breakdown of the Statistical-Equilibrium Hypothesis in Channeling.* Phys. Rev. Lett. **31**, 1542 (1973).

J.H. Barrett *et al.*, *Effect of Thermal Vibrations and Nuclear Recoil on the Minimum Yield in Channeling Phenomena.* Radiat. Eff. **28**, 119 (1976).

V.V. Beloshitsky, M.A. Kumakhov, and V.A. Muralev, *Multiple Scattering of Channeled Ions in Crystals.* Radiat. Eff. **13**, 9 (1972).

- V.V. Beloshitsky, M.A. Kumakhov, and V.A. Muraley, *Multiple Scattering of Channeling Ions in Crystals II-Planar Channeling*. Radiat. Eff. **20**, 95 (1973).
- N. Bohr and J.A. Wheeler, *The Mechanism of Nuclear Fission*. Phys. Rev. **56**, 426 (1939).
- N. Bohr, *The Penetration of Atomic Particles through Matter*. K. Dan. Vidensk. Selsk. Mat. Fys. Medd. **18** No 8 (1948).
- E. Bonderup, H. Esbensen, J.U. Andersen, and H.E. Schiøtt, *Calculations on Axial Dechanneling*. Rad. Eff. **12**, 261 (1972).
- W. Brandt, *Channeling in Crystals*. Scientific American **218**, 91 (1968)
- J.C. Briggs and A.P. Pathak, *Momentum Transfer Cross Sections and the Z_1 Oscillations in Stopping Power*. J. Phys. C **6**, L153-L157 (1973).
- E. Bøgh, J.A. Davies, and K.O. Nielsen, *Experimental Evidence for the Extinction of (p,γ) Yields in Single Crystals*. Phys. Lett. **12**, 129 (1964).
- E. Bøgh and E. Uggerhøj, *Orientation Dependence of Rutherford Scattering Yields in Single Crystals*. Phys. Lett. **17**, 116 (1965).
- E. Bøgh, *Rutherford Scattering of Protons in the Surface Layers of a Tungsten Single Crystal*. Phys. Rev. Lett. **19**, 61 (1967).
- E. Bøgh and J.L. Whitton, *Reversibility of Fast Charged Particle Trajectories in Single Crystals*. Phys. Rev. Lett. **19**, 553 (1967).
- E. Bøgh, *An Application of High Energy-Resolution Scattering Measurements in Channeling Studies*. Radiat. Eff. **12**, 11 (1972).
- C. Cohen and D. Dauvergne, *High Energy Ion Channeling. Principles and Typical Applications*. Nucl. Instrum. Methods in Phys. Res. **225**, 40-71 (2004).
- S. Datz, B.L. Berman, B.A. Dahling, M.V. Hynes, H. Park, J.O. Kephart, R.K. Klein, and R.H. Pantell, *On the Dependence of Electron Planar Channeling Radiation upon Lattice Vibration Amplitude*. Nucl. Instrum. Methods in Phys. Res. B **13**, 19-22 (1986).
- J.A. Davies, *The Channeling Phenomenon – and some of its Applications*. Phys. Scripta **28**, 294 (1983).
- G. Dearnaley, Preprint Oct. 1963. *The Channeling of Ions through Detectors*. IEEE Trans. Nucl. Sci. **NS-11** (1964).

- B. Domeij and K. Björkqvist, *Anisotropic Emission of Alpha Particles from a Monocrystalline Source*. Phys. Lett. **14**, 127 (1965).
- P.A. Doyle and P.S. Turner, *Relativistic Hartree-Fock X-ray and Electron Scattering Factors*. Acta Crystallogr. **A24**, 390 (1968).
- G.O. Engelmohr, R.M. Müller, and W. White, *a Positive Ion Camera for Blocking and Channeling Studies*. Nucl. Instr. Methods **83**, 160 (1970).
- K.R. Eriksen, Cand. Scient. Thesis, University of Aarhus (1980, unpublished).
- L. Eriksson, J.A. Davies, and P. Jespersgaard, *Range Measurements in Oriented Tungsten Single Crystals (0.1-1.0 MeV). I. Electronic and Nuclear Stopping Powers*. Phys. Rev. **161**, 219-234 (1967).
- H. Esbensen and J.A. Golovchenko, *Energy Loss of Fast Channeled Particles*. Nucl. Phys. A **298**, 382-396 (1976).
- H. Esbensen, O. Fich, J.A. Golovchenko, S. Madsen, H. Nielsen, H.E. Schiøtt, E. Uggerhøj, C. Vraast-Thomsen, G. Charpak, S. Majewski, G. Odyniec, G. Petersen, F. Sauli, J.P. Ponpon, and P. Siffert, *Random and Channeled Energy Loss in Thin Germanium and Silicon Crystals for Positive and Negative 2-15-GeV/c Pions, Kaons, and Protons*. Phys. Rev. B **18**, 1039-1054 (1978).
- L.C. Feldman, Ph.D. Thesis, Rutgers University, N.J. USA (1967) .
- L.C. Feldman and B.R. Appleton, *Multiple Scattering and Planar Dechanneling in Si and Ge*. Phys. Rev. B **8**, 935 (1973).
- L.C. Feldman, J.W. Mayer, and S.T. Picraux, *Materials Analysis by Ion Channeling*. (Academic Press, London, 1982).
- J. Finnemann, *En redegørelse for resultaterne af beregninger over spredning af elektroner med lav energi på afskærmede Coulombfelter*. Thesis under supervision of J. Lindhard, Physics Institute, University of Aarhus (1968).
- J.S. Forster, G.C. Ball, W.G. Davies, J.S. Geiger, J.U. Andersen, J.A. Davies, H. Geissel and F. Nickel: *Resonant Coherent Excitation (RCE) of Higher-Order Resonances for $^{28}\text{Si}^{13+}$ Ions Channeled in a Thin Si Crystal*. Nucl. Instr. Meth. B **107**, 27-30 (1996).
- D.S. Gemmell and R.E. Holland, *Blocking Effects in the Emergence of Charged Particles from Single Crystals*. Phys. Rev. Lett. **14**, 945 (1965).

D.S. Gemmell, *Channeling and Related Effects in the Motion of Charged Particles Through Crystals*. Rev. Mod. Phys. **46**, 129 (1974).

W.M. Gibson, *Blocking Measurements of Nuclear Decay Times*. Ann. Rev. Nucl. Sci. **25**, 465-508 (1975).

M. Guanere, D. Sillou, M. Spighel, N. Cue, M.J. Gaillard, R.G. Kirsch, J-C. Poizat, J. Remmillieux, B.L. Berman, P. Cattillon, L. Roussel, and G.M. Temmer, *Sharp-Line and Broad-Continuum Radiation from Electrons Channeled in Diamond*. Nucl. Instrum. Methods, **194**, 225-228 (1982).

K. Gärtner, K. Hehl, and G. Schlotzhauer, *Axial Dechanneling: II. Point Defects*. Nucl. Instrum. Methods B **4**, 55-62 (1984).

L.V. Hau, E. Lægsgaard, and J.U. Andersen, *Thermal Vibrations in Si Studied by Channeling-Radiation Spectroscopy*. Nucl. Instrum. Methods in Phys. Res., B **48**, 244-247 (1990).

L. Vestergaard Hau and J.U. Andersen, *Channeling Radiation Beyond the Continuum Model: The Phonon "Lamb shift" and Higher-Order Corrections* Phys. Rev. A **47**, 4007-4032 (1993); *Line Shifts of Channeling Radiation from MeV Electrons*. Rad. Effects and Defects in Solids **25**, 75-80 (1993).

H. Hofsäss, *Emission Channeling*. Hyperfine Interactions **97-8**, 247-283 (1996).

H.F. Krause and S. Datz, *Channeling Heavy Ions Through Crystalline Lattices*. Adv. At. Mol. Opt. Phys. **37**, 139-180 (1996).

M.A. Kumakhov, *On the Theory of Electromagnetic Radiation of Charged Particles in a Crystal*. Phys. Lett. A **57**, 17-18 (1976).

Ph. Lervig, J. Lindhard, and V. Nielsen, *Quantal Treatment of Directional Effects for Energetic Charged Particles in Crystal Lattices*. Nucl. Phys. A **96**, 481-504 (1967).

J. Lindhard, M. Scharff, and H.E. Schiøtt, *Notes on Atomic Collisions, II*. K. Dan. Vidensk. Selsk. Mat. Fys. Medd. **33**, No 14 (1963).

J. Lindhard, *Motion of Swift Charged Particles, as Influenced by Strings of Atoms in Crystals*. Phys. Lett. **12**, 126 (1964).

J. Lindhard, *Influence of Crystal Lattice on Motion of Energetic Charged Particles*. K. Dan. Vidensk. Selsk. Mat. Fys. Medd. **34** No 14 (1965).

- H. Lutz and R. Sizmann, *Super Ranges of Fast Ions in Copper Single Crystals*. Phys. Lett. **5**, 113 (1963).
- N. Matsunami, M.L. Swanson, and L.M. Howe, *The Determination of Solute Atom Displacements in Mixed Dumbbell Interstitials for the Face-Centered Cubic Lattice*. Can. J. Phys. **56**, 1057 (1978).
- N. Matsunami and L. M. Howe, *A Diffusion Calculation of Axial Channeling in Si and Ge*. Radiat. Effects **51**, 111-26 (1980).
- C.D. Moak, S. Datz, O.H. Crawford, H.F. Krause, P.F. Dittner, J. Gomez del Campo, J.A. Biggerstaff, P.D. Miller, P. Hvelplund, and H. Knudsen, *Resonant Coherent Excitation of Channeled Ions*. Phys. Rev. A **19**, 977-993 (1979).
- Y. Nakai, T. Ikeda, Y. Kanai, T. Kambara, N. Fukinishi, K. Komaki, C. Kondo, T. Azuma, and Y. Yamazaki, *Resonant Coherent Excitation of 2s Electron of Li-like Fe Ions to the $n = 3$ States*. Nucl. Instrum. Methods in Phys. Res. B **230**, 90-95 (2005).
- B. Bech Nielsen, private communication, 1986, and thesis 1987.
- B. Bech Nielsen, J.U. Andersen, and S.J. Pearton, *Lattice Location of Deuterium Interacting with the Boron Acceptor in Silicon*. Phys. Rev. Lett. **60**, 321-324 (1988).
- O.H. Nielsen and W. Weber, *Displacement Correlations in Semiconductors*. J. Phys. C: Sol. St. Phys. **13**, 2449 (1980).
- O.S. Oen, *Interpretation of the Anisotropy of Alpha Particle Emission from a Monocrystalline Source*. Phys. Lett. **19**, 358 (1965).
- V.V. Okorokov, *The Coherent Excitation of Nuclei Moving through a Crystal*. Yad. Fiz. **2**, 1009 (1965) [Sov. J. Nucl. Phys. **2**, 719 (1966)].
- M.J. Pedersen, J.U. Andersen, and W.M. Augustyniak, *Channeling of Positrons*. Rad. Effects **12**, 47-52 (1972).
- M.J. Pedersen, J.U. Andersen, D.J. Elliott, and E. Lægsgaard, *Axial Dechanneling II. An Experimental Study*. In *Atomic Collisions in Solids*, Vol. II, S. Datz, B.R. Appleton, and C.D. Moak (eds.) (Plenum Press, New York, 1975) p. 863.
- S.T. Picraux and J.U. Andersen, *Measurements and Calculations of Critical Angles for Planar Channeling*. Phys. Rev. **186**, 267 (1969).

- S.T. Picraux, J.A. Davies, L. Eriksson, N.G.E. Johansson, and J.W. Mayer, *Channeling Studies in Diamond-Type Lattices*. Phys. Rev. **180**, 873 (1969).
- G.R. Piercy, F. Brown, J.A. Davies, and M. McCargo, *Experimental Evidence for the Increase of Heavy Ion Ranges by Channeling in Crystalline Structures*. Phys. Rev. Lett. **10** (1963).
- J.C. Poizat and J.R. Remillieux, *Calculations of Planar-Channeling Effects on Rutherford Scattering in Single Crystals*. Phys. Rev. Lett. **27**, 6 (1971).
- F. Berg Rasmussen and B. Bech Nielsen, *Microstructure of the Nitrogen Pair in Crystalline Silicon Studied by Ion Channeling*. Phys. Rev. B **49**, 16353-16360 (1994).
- M.T. Robinson and O.S. Oen, *The Channeling of Energetic Atoms in Crystal Lattices*. Appl. Phys. Lett. **2**, 30-32 (1963). *Computer Studies of the Slowing Down of Energetic Atoms in Crystals*. Phys. Rev. **132**, 2385-99 (1963).
- H.E. Schiøtt, E. Bonderup, J.U. Andersen, and H. Esbensen, *Axial Dechanneling I. A Theoretical Study*. In *Atomic Collisions in Solids*, Vol. 2, S. Datz, B.R. Appleton, and C.D. Moak (eds.), (Plenum Press, New York, 1975) p843.
- R.P. Sharma, J.U. Andersen, and K.O. Nielsen, *Application of Blocking Technique to Measure Lifetimes of Nuclear Levels Excited in (p, alpha) Reactions in P and Al*. Nucl. Phys. **A204**, 371 (1973).
- A.H. Sørensen and E. Uggerhøj, *Channeling and Channeling Radiation*. Nature **325**, 311 (1987).
- A.F. Tulinov, V.S. Kulikauskas, and M.M. Malov, *Proton Scattering from Tungsten Single Crystal*. Phys. Lett. **18**, 304 (1965).
- E. Uggerhøj, *Orientation Dependence of the Emission of Positrons and Electrons from ^{64}Cu Embedded in Single Crystals*. Phys. Lett. **22**, 382 (1966).
- E. Uggerhøj and J.U. Andersen, *Influence of Lattice Structure on Motion of Positrons and Electrons through Single Crystals*. Can. J. Phys. **46**, 543 (1968).
- E. Uggerhøj, *Some Energy-Loss and Channeling Phenomena for GeV Particles*. Phys. Scripta **28**, 331 (1983).
- U.I. Uggerhøj, *The Interaction of Relativistic Particles with Strong Crystalline Fields*. Rev. Mod. Phys. **77**, 1131-1171 (2005).